

Doctoral theses at NTNU, 2022:112

Ewa Karchniwy

Detailed numerical modeling of solid fuels conversion processes

ISBN 978-82-326-6228-9 (printed ver.)
ISBN 978-82-326-5456-7 (electronic ver.)
ISSN 1503-8181 (printed ver.)
ISSN 2703-8084 (electronic ver.)

Doctoral theses at NTNU, 2022:112

NTNU
Norwegian University of
Science and Technology
Thesis for the degree of
Philosophiae Doctor
Faculty of Engineering
Department of Energy and Process Engineering

 **NTNU**
Norwegian University of
Science and Technology

 NTNU

 **NTNU**
Norwegian University of
Science and Technology

Ewa Karchniwy

Detailed numerical modeling of solid fuels conversion processes

Thesis for the degree of Philosophiae Doctor

Trondheim, April 2022

Norwegian University of Science and Technology
Faculty of Engineering
Department of Energy and Process Engineering



Norwegian University of
Science and Technology

NTNU

Norwegian University of Science and Technology

Thesis for the degree of Philosophiae Doctor

Faculty of Engineering
Department of Energy and Process Engineering

© Ewa Karchniwy

ISBN 978-82-326-6228-9 (printed ver.)

ISBN 978-82-326-5456-7 (electronic ver.)

ISSN 1503-8181 (printed ver.)

ISSN 2703-8084 (electronic ver.)

Doctoral theses at NTNU, 2022:112



Printed by Skipnes Kommunikasjon AS

Preface

This thesis is submitted to the Norwegian University of Science and Technology (NTNU) and the Silesian University of Technology (SUT) for partial fulfillment of the requirements for the degree of philosophiae doctor. The doctoral work has been performed partially at the Department of Energy and Process Engineering, NTNU, Trondheim, and partially at the Department of Thermal Engineering, SUT, Gliwice. The aforementioned institutions agreed on terms and requirements of a Double Degree in a Cotutelle Agreement. This work was supervised by Professor Terese Løvås and Dr. Ing. Nils Erland L. Haugen at NTNU, and Associate Professor Adam Klimanek at SUT.

Abstract

This thesis investigates conversion of solid fuel particles from different perspectives. In particular, two aspects of the conversion process are studied: 1) the effect of turbulence on the conversion rate and 2) the combustion behaviour of a single carbon particle.

Direct Numerical Simulations of polydisperse particle systems in a periodic box of isotropic and homogeneous turbulence were performed in order to analyse how turbulence affects the mass transfer rate in such configuration. The effect of turbulence was found to be identical qualitatively and very similar quantitatively to what was observed for monodisperse particle systems, i.e. there exist two opposing mechanisms through which turbulence can affect the reactant transfer to surfaces of particles. The first mechanism leads to formation of particle clusters, which are responsible for decreased mass transfer rate, while the other is associated with the mass transfer being enhanced by turbulent motions. The model which accounts for the combined effect of turbulence was shown to be applicable to polydisperse particle systems. The effect of particle back-reaction was also studied, the results revealed its importance especially in cases characterized by high Stokes numbers. A sensitivity of the effect of turbulence to selected parameters was investigated through theoretical analysis and using simple numerical examples. Several parameters (mixture composition, particle material, turbulence intensity, particle size, mass flow rate) were demonstrated to have a meaningful influence on how strong the effect is. Finally, the effect of turbulence on the conversion rate in practical systems was examined. For this purpose, an industrial-scale boiler was simulated in ANSYS Fluent. The results showed that regions of very different conditions can simultaneously occur in different parts of the boiler, which rules out the possibility to predict the net effect of turbulence a priori. Moreover, it was shown that the conversion rate might be affected by turbulence much less than expected based on theoretical predictions as the reaction rate is often controlled by kinetics, i.e. it is independent on the rate of reactant transfer.

A simple model for the resolved carbon particle conversion was implemented in the Pencil Code. Efficiency of the model was achieved by pre-adjustment of diffusion coefficients, reduction of the speed of sound and employment of a semi-global mechanism. Despite numerous simplifications, an ability of the model to predict main characteristics of the char particle conversion and formation of a flame zone was demonstrated by validating the model against experimental and numerical results. Sensitivity of the conversion rate to kinetic parameters and transport coefficients was studied. A strong sensitivity to the oxygen diffusivity was registered, especially at higher temperatures.

Acknowledgements

I have never considered myself as particularly lucky. My mind was changed soon after I had started my research project under the supervision of Adam Klimanek and Nils Erland L. Haugen. Today, after several years of our collaboration, I have no doubts: I must have drawn a lucky ticket in the 'supervisors lottery'. I am extremely grateful for the opportunity to work with supervisors who I look up to both as excellent researchers and great human beings. Thank you not only for your scientific guidance, but also for all the effort you patiently put into raising my confidence, and for never doubting my abilities or letting me feel bad about myself, even when I made mistakes or got stuck on some problems. Your support meant the world to me and I appreciate so much all I learned from you throughout these years.

I would also like to thank Terese Løvås for taking the role of my formal supervisor and for that I have always felt welcome in the Department of Energy and Process Engineering.

My parents, Basia and Andrzej, have always been there for me, whenever I needed them. I could count on their understanding even though at times I would neglect my family responsibilities. I am also grateful to other members of my closest family (Anna, Leszek, Bożena and Grażyna) who kept their fingers crossed for me and who would welcome all updates on my research with curiosity and encouragement.

Finally, I would never have made it to the finish line had it not been for my friends. I am particularly grateful to:

- Justyna, you are the most down-to-earth person I have ever known. Thank you for being such a great and supportive friend!
- Suyash, our funny, spontaneous conversations were exactly what I needed during the most challenging periods, thank you for that!
- Shareq, you believed in me much more than I did myself. Thank you for all discussions and coffee breaks.
- Dominika and Michał, you were always ready to help me, regardless of whether I had a broken bike or needed some motivational words.
- All members of SCS OSOZ Racing Team, to compete as your teammate was the best way to temporarily forget about my research struggles.
- My lovely housemates: Abba, Marcelo, Katriina, Ivana and Dusan, thank you for caring and making my PhD experience so much better!

- My fellow PhD students and post-docs at the Department of Thermal Engineering in Gliwice and at the Department of Energy and Process Engineering in Trondheim, I am glad to share this journey with you, thanks for all your encouragement and everyday discussions.

Contents

Preface	iii
Abstract	v
Acknowledgements	viii
Thesis structure	xi
List of Figures	xiii
1 Introduction	1
1.1 Statistics and motivation	1
1.2 Different approaches to modeling of particulate flows	3
1.3 Solid fuel conversion	6
1.4 The effect of turbulence on the solid fuel conversion rate	12
1.5 Numerical studies of solid fuels conversion - literature review . . .	15
1.5.1 Point particle DNS	15
1.5.2 Resolved particle simulations	17
1.5.3 Literature review - summary	24

1.6 Thesis objectives	24
2 Methodology	27
2.1 The Pencil Code and its expansion	27
2.1.1 Development of the numerical model used in Paper III	29
2.2 Numerical model for large-scale simulations	34
3 Contributions	35
3.1 Summary of Paper I	35
3.2 Summary of Paper II	37
3.3 Summary of Paper III	39
3.4 Other contributions	40
4 Thesis summary	43
4.1 Conclusions	43
4.2 Future work	44
Bibliography	47
5 Research papers	65
5.1 Paper I	67
5.2 Paper II	91
5.3 Paper III	107

Thesis structure

This thesis is in the form of a collection of papers and has the following structure. Chapter I provides a brief introduction to the problems tackled in this thesis and discusses the relevant literature, while in Chapter II theoretical aspects (mathematical formulation and numerical methods) are outlined. Chapter III summarizes publications that form a basis for this thesis. Other publications and conference materials the author of this thesis was involved in (that are not subjected to assessment) are also mentioned. Concluding remarks and potential work that remains to be done in the future are the subject of Chapter IV. In the last chapter, Chapter V, author's main publications are attached.

The following publications are subjected to assessment:

- Paper I: Ewa Karchniwy, Adam Klimanek, Nils Erland L. Haugen (2019). *The effect of turbulence on mass transfer rates between inertial polydisperse particles and fluid*. Journal of Fluid Mechanics, 874, 1147-1168.
- Paper II: Ewa Karchniwy, Nils Erland L. Haugen, Adam Klimanek, Øyvind Langørgen, Sławomir Śladek (2021). *The effect of turbulence on mass transfer in solid fuel combustion: RANS model*. Combustion and Flame, 227, 65-78.
- Paper III: Ewa Karchniwy, Nils Erland L. Haugen, Adam Klimanek. *A numerical study on the combustion of a resolved carbon particle*. Submitted for consideration to Combustion and Flame.

List of Figures

1.1	Classification of approaches to particulate flows modeling	4
1.2	Different scales at which solid fuel conversion can be modeled (to create this figure Fig. 16 in [1] and Fig. 5 in [2] were used, as well as Fig. 13 from the submitted paper attached in Section 5.3)	5
1.3	Schematics of the solid fuel conversion process. The focus of this thesis is on the char particle combustion, indicated in the violet frame.	7
1.4	Schematics of the coal chemical structure (reused from [3] based on CC-BY license). From the chemical standpoint, coal consists of organic matrix with mineral inclusions. The organic part, shown in the figure, is a macromolecular network composed of condensed aromatic rings and peripheral groups (side chains). The rings are grouped into aromatic nuclei (clusters) that are connected with each other by labile bridges [4].	7
1.5	Combustion zones/regimes (figure reproduced basen on Fig. 1 in [1])	10
1.6	Interactions between a particle with a characteristic time scale τ_p and turbulent eddies belonging to different ranges of turbulence energy spectrum (the turbulence energy spectrum reproduced based on Fig. 1 in [2])	14

2.1	Schematic representation of a domain for the resolved particle case (not drawn to scale). A grey circle in the middle represents the particle, interior of which is not resolved. An exemplary 4 th order interpolation stencil (black dots) is also shown. $n + 1$ grid points in each spatial direction (d) are needed for n^{th} order interpolation, such that the interpolation stencil consists of the $(n + 1)^d$ points that are situated closest to the receiver point, to which a function is interpolated to. The interpolation zone on the ogrid (the region bounded by pink dashed lines) is chosen in such a way that none of the points belonging to the interpolation stencil on the Cartesian grid is located inside the interpolation zone on the ogrid.	29
2.2	Comparison of 1D profiles of temperature (left) and species mass fractions (right)	30
3.1	Particle number density for different particle sizes. The particle size grows from left to right. Upper row: 2-way coupling, lower row: 1-way coupling (figure reproduced from [2])	36
3.2	Distribution of Damköhler and Stokes numbers inside the investigated practical system (figure reproduced from [1]). The strongest effect of particle clustering is expected to be observed at high Da and at $St \sim 0.1$ (in lower parts of the boiler and around injections), while the effect associated with relative velocity is expected to be most pronounced at relatively low Da, in the upper part of the domain. White areas are regions with no particles.	38
3.3	Contours of carbon monoxide flame, left: gas phase reaction rate reduced by a factor of 2, right: gas phase reaction rate increased by a factor of 2	40

Chapter 1

Introduction

1.1 Statistics and motivation

Solid fuels are one of the most common energy sources in the world. In spite of its diminishing role, coal remains the largest source for power generation and has a second to oil largest share in the global energy mix. According to the last year's Statistical Review of World Energy report [5], in 2019 coal accounted for around 27% of the primary energy consumption and satisfied 36.4% of electricity demand. Contrary to coal, solid fuels classified as renewable energy sources, such as biomass and refuse-derived fuel, are recognized as important energy sources in the future and their share in the primary energy is expected to grow [6].

Despite a slight decline of the energy demand in 2020 induced by the COVID-19 pandemics, the global primary energy consumption continues to grow and is predicted to be increasing in the coming years [7]. This growing demand necessitates a wise use of energy resources. This is particularly crucial in the case of energy produced out of fossil fuels, since their burning contributes to the majority of the greenhouse emissions in the world, which has severe consequences both for the climate and human health. Out of available fossil fuels, it is coal that contributes to the highest carbon dioxide production and air pollution per unit of produced energy [8]. It is, however, unlikely that the global coal consumption will be radically reduced in the near future. The reason for that is coal's relatively low cost, abundance and availability, together with the fact that the development of countries like e.g. China and India heavily relies of coal-based energy. According to recent data, coal generation maintained a constant level over the past five years as a decrease in the coal consumption in OECD countries is balanced by the consumption increase in emerging economies [9]. It seems that a reasonable, albeit temporary, solution

is to adopt so called clean coal technologies that aim to reduce environmental impact of coal by modifying current technologies to achieve increased efficiency and reduced emissions. The World Energy Resources report [10] estimates that an average 7% increase in the efficiency of coal-fired power plants would reduce the global CO₂ emission by 1.7 billion tonnes every year. While this number is not very impressive when juxtaposed with over 30 billion tonnes of carbon dioxide emitted yearly, the adoption of clean coal technologies might be an important step towards succeeding in climate change mitigation. This can be supported by the fact that the predicted growth of electricity demand will be only partially satisfied by the growing contribution of renewables [11].

In order to design low-emission and highly-efficient technologies, and thus to reduce the negative environmental impact, a better understanding of fundamental processes occurring during solid fuels conversion is needed. This understanding can be gained through experiments and numerical analysis. Both of these research methodologies are employed nowadays to study solid fuels conversion. Using various experimental techniques, solid fuels heating value, composition (both elemental and in terms of moisture, volatile matter, fixed carbon, and ash), density, porosity as well as other properties can be determined. The experimental techniques, although most of them are known already for a long time, are still being developed and improved to provide more accurate and a wider range of results. Experimental investigations are also essential to provide input parameters for numerical simulations and data for model validation. In fact, the entire field of numerical combustion relies on kinetic parameters that are determined experimentally, typically through thermogravimetric analysis, e.g. [12, 13] or by optical observations in a drop tube furnace, e.g. [14, 15, 16]. Despite the many advantages of experiments, information provided by them may not be complete due to complexity and a broad range of scales involved in the solid fuel conversion processes. Moreover, it might be cost-ineffective to experimentally test new technologies, and to examine the impact of multiple parameters on their performance. The existing gaps in knowledge and understanding can be addressed through numerical modeling. Nowadays, numerical models are frequently used in design of new and optimization/improvement of existing solid fuel combustion systems. Numerical simulations of solid fuels conversion are most often performed using multiphase Computational Fluid Dynamics (CFD) codes coupled with chemical kinetics. The goal of the work presented in this thesis was to study different aspects of fundamental phenomena occurring during solid fuel conversion. To carry out these studies, various numerical approaches and solvers were employed, as will be explained later in this thesis.

1.2 Different approaches to modeling of particulate flows

Domestic use of solid fuel typically include burning of quite large fuel pieces, e.g. wood logs. Fuels such as wood or waste are also utilized in relatively large pieces on the industrial scale in special installations e.g. grate boilers. However, in the case of large coal combustion and gasification systems, coal is usually grinded (pulverized) in special devices into very small particles. Since the focus of this work is on such systems, the following discussion is in the context of pulverized fuel combustion. CFD simulations of solid fuels conversion belong to a general class of flows with particles. When modeling particulate flows, the selection of numerical approach is often dictated by the time and length scales of the problem in question, as well as the particle volume fraction and the mass loading. As a general rule, the larger the scale of the analyzed system, the more modeling is required, where by modeling it is meant that certain phenomena are accounted for through empirical or approximate expressions. This is because these phenomena happen at too small (or short) scales or are too complex to be considered directly; or because certain limitations of the numerical approach make it impossible to avoid modeling. An inherent consequence of modeling is compromised accuracy, it is therefore important that models used in a simulation reflect all key phenomena with the level of detail which is required by specific application.

A schematic classification of approaches to particulate flows modeling is shown in Fig. 1.1. Flows characterized by the high particle volume fraction are often studied using Euler-Euler approach in which both the fluid and the solid phase is treated as a continuum and solved in the Eulerian reference frame. Such an approach is suitable for modeling of some particle-laden flows, sedimentation, fluidized beds or pneumatic transport. This method is mentioned here for the sake of completeness as it is rarely applicable to solid fuel conversion and is not used in this work.

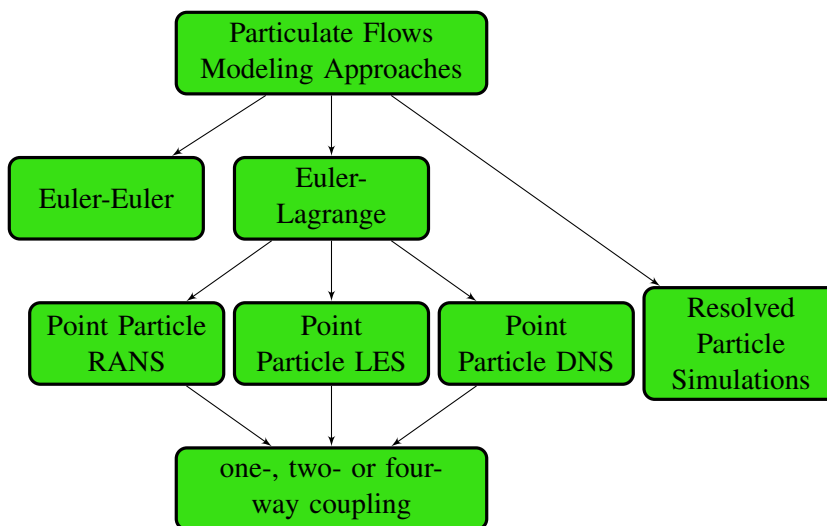


Figure 1.1: Classification of approaches to particulate flows modeling

Whenever the solid phase volume fraction is relatively low, the so-called Euler-Lagrange (sometimes also called point particle) approach becomes applicable. With this approach, the fluid phase is treated as a continuum, but the particles are treated as point sources and are tracked separately or in groups in the Lagrangian reference frame. The mass, momentum and energy exchange between particles and fluid, as well as collisions between particles can be included through appropriate models. The fluid-particle interactions are realized as one-way or two-way couplings, where the one-way coupling means that the exchange is from the fluid to particles only, without the feedback (back-reaction) from particles to fluid; while the two-way coupling includes the particle back-reaction. If, in addition, particle collisions are considered, such a strategy is referred to as four-way coupling and is usually applied to particulate flows with high mass loading. The Euler-Lagrange approach with different degree of coupling is often used to model solid fuels conversion systems. Depending on what fraction of turbulence energy spectrum is resolved, these studies can be further categorized into Reynolds-averaged Navier-Stokes (RANS), Large Eddy Simulation (LES) and Direct Numerical Simulation (DNS). In RANS, flow quantities are decomposed into mean and fluctuating parts. In order to solve for mean quantities, the fluctuating component, which incorporates effects of turbulence, must be modeled using a suitable turbulence model. In LES, large scales of turbulence are resolved but a part of the turbulence energy spectrum corresponding to small (and sometimes also medium-size) eddies must be modeled using subgrid scale models.

A full-scale industrial boiler, depicted in the left panel of Fig. 1.2, is a good example of cases typically investigated using RANS or, eventually, LES approach with the Euler-Lagrange framework. In addition to the turbulence energy spectrum, all effects of turbulence, e.g. on particle dispersion, and on homogeneous and heterogeneous reactions, have to be modeled. The models to be used in those large-scale simulations of particulate flows can be formulated based on the results of simulations carried out at much smaller scales. An example of such a simulation is shown in the middle panel of Fig. 1.2. It can be thought of as if a tiny volume of turbulent flow with reacting particles was cut out from the large-scale boiler domain and analyzed in detail. This approach is called DNS and its main characteristic is that all scales of turbulence are resolved on the numerical grid. Even at this relatively small-scale, the number of particles is quite large so they need to be treated as point sources with fluid-particles interactions accounted for by closure expressions, e.g. drag laws.

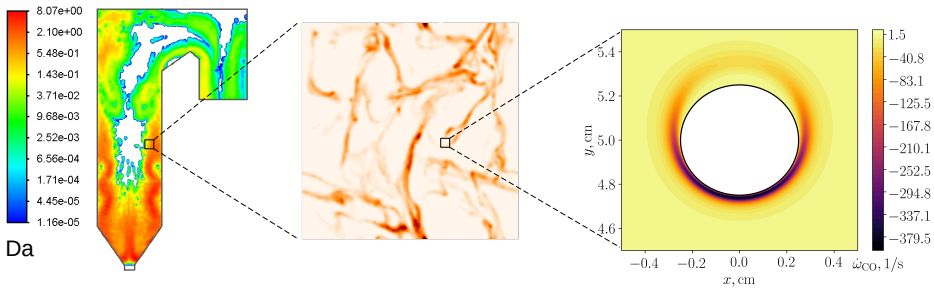


Figure 1.2: Different scales at which solid fuel conversion can be modeled (to create this figure Fig. 16 in [1] and Fig. 5 in [2] were used, as well as Fig. 13 from the submitted paper attached in Section 5.3)

The point particle approximation is commonly used in DNS studies on solid fuels conversion as it allows one to investigate turbulent flows that contain a large number of particles, and such simulations are good representations of practical systems. However, the main limitation of this approximation is that it is strictly applicable to relatively small particles, i.e. particles smaller than the smallest length scales of turbulence (Kolmogorov scale) [17, 18]. Moreover, the accuracy of the results strongly relies on selected closure expressions that model interactions between particles and fluid. If accuracy and a high level of detail is the main concern, the particle surface together with its boundary layer can be resolved directly on a numerical grid. In Fig. 1.1 this approach is called the resolved particle simulation. In order to resolve the particle, the grid cells close to the particle surface must be much smaller than the particle itself. This limits the applicability of resolved simulations to a much lower number of particles than it is possible to study with the

point particle approach. Currently, the number of resolved particles of the order of 10^3 [19] or even up to 10^4 [20] can be considered in non-reactive simulations. Recently, several hundred particles with catalytic reaction in a fixed-bed reactor [21, 22] were simulated with the resolved DNS approach. Resolved simulations of solid fuel conversion are, however, most often limited to a single particle or a small particle arrays due to increased complexity of the problem and high computational effort associated with reactive flows. Nevertheless, it is already possible to simulate a collection of resolved, colliding particles in a turbulent, reacting flow [23]. It should be expected that similar approaches will be soon adopted to study solid fuel conversion. An example of a resolved particle approach applied to a solid fuel particle is presented in the right panel of Fig. 1.2, which shows a CO flame (CO reaction rate) forming around a carbon particle. The length scales in such simulations are typically several orders of magnitude smaller than the length scales considered in RANS studies, which means that fundamental phenomena can be studied in great details with particle resolved simulations. This brings many advantages of such an approach and makes it an attractive research tool. For example, closure expressions for mass, momentum and energy exchange to be used in point particle simulations can be formulated, verified and improved based on the results obtained from resolved simulations [24, 25].

In this work, three different numerical approaches are employed to study solid fuels conversion, namely the Euler-Lagrange approach combined with RANS and DNS, and the resolved particle simulation.

1.3 Solid fuel conversion

Before discussing objectives of the current work and the relevant literature, it is worthwhile to briefly analyse component processes occurring during solid fuel conversion. These processes are schematically presented in Fig. 1.3. It should be noted though that this picture is highly simplified, as there are also many other fundamental processes and phenomena that are involved in the coal or biomass combustion. The complex nature of solid fuel conversion is a consequence of the fuel molecular structure. To get a feel of the situation, a schematics of the chemical structure of the coal organic part is presented in Fig. 1.4. Although in this thesis only char conversion is considered, which is modeled in a simplified manner, a general description of solid fuel conversion together with relevant modeling approaches is given in this section. This brief description should provide the reader with a broader perspective on the problems that are dealt with in this thesis.

The conversion process begins with heat being transferred to fuel particles. Upon heating, the particles dry and devolatilize. The volatile matter is then mixed with oxidizer and burns in a volumetric fashion. Although the process of volatiles

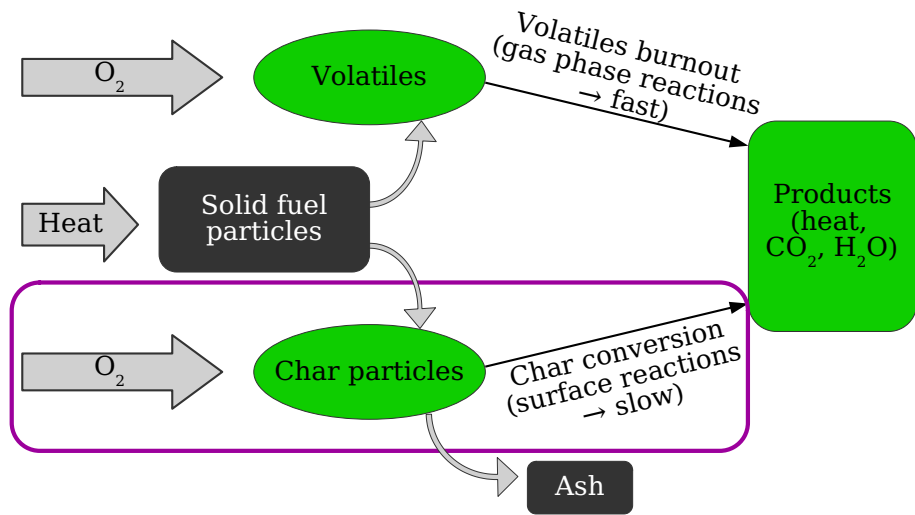


Figure 1.3: Schematics of the solid fuel conversion process. The focus of this thesis is on the char particle combustion, indicated in the violet frame.

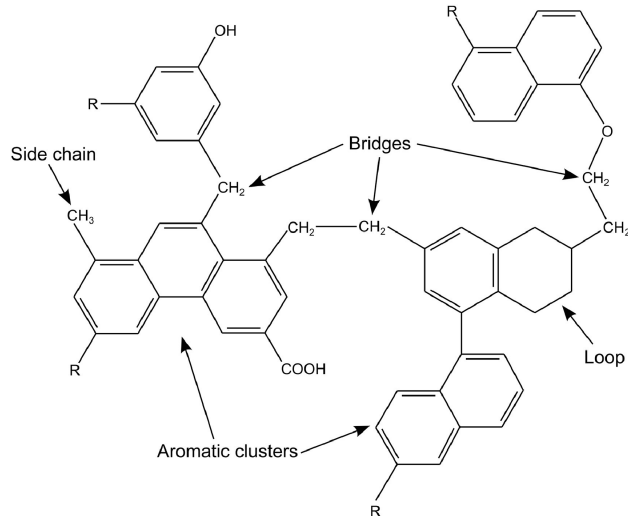
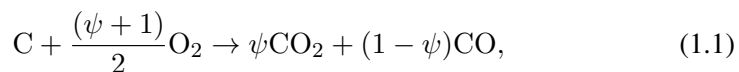


Figure 1.4: Schematics of the coal chemical structure (reused from [3] based on CC-BY license). From the chemical standpoint, coal consists of organic matrix with mineral inclusions. The organic part, shown in the figure, is a macromolecular network composed of condensed aromatic rings and peripheral groups (side chains). The rings are grouped into aromatic nuclei (clusters) that are connected with each other by labile bridges [4].

burnout is very fast, it is also extremely complex. An accurate description of devolatilization needs to account for the solid fuel molecular structure decomposition, yield of different volatile matter components (such as light gases and heavy hydrocarbons) and char formation. In addition, the devolatilization rate is influenced by e.g. heating rates, fuel rank (i.e. fraction of carbon in solid fuel) or particle size and this dependence must also be accounted for. Several phenomenological network models exist that are capable of predicting all of the above mentioned aspects of devolatilization. The best known ones, developed for coal, are Functional Group-Depolymerization, Vaporization and Crosslinking model [26], Flash-Distillation Chain-Statistics model [27] and Chemical Percolation Devolatilization model [28]. Based on these three models, many different versions were formulated that improve their predictions in certain areas or extend their applications e.g. to biomass [29, 30]. Due to high computational cost associated with network models, they are rarely employed directly in CFD computations. Most often, simple empirical models are used instead, such as global kinetic single- or multi-step models [31, 32], or a distributed activation energy model [33, 34]. These models must be calibrated based on pyrolysis experiments, they are often limited to particular conditions and are able to predict the volatiles yield only for very simplified volatiles compositions. Nevertheless, they are efficient and easy to implement, which justifies their broad use in CFD studies. Recently, an improved approach to model devolatilization in CFD simulations was explored, which combines advantages of the network models and empirical models by calibrating the latter using results provided by the former [35, 36].

One of the products of devolatilization is char. Although combustion of char is often considered as a process subsequent to devolatilization, some experimental [37] and numerical [38] studies suggest that these processes can happen simultaneously, i.e. the char combustion begins before the volatiles burnout is complete. The char particles are highly porous and undergo conversion through heterogeneous reactions, i.e. through reactions that occur on the char particle surface. Heterogeneous reactions can be classified into oxidation:



in which oxygen is the reactant, and gasification:



in which the reactants are carbon dioxide, steam or hydrogen. Most gasification reactions are endothermic and much slower than exothermic oxidation. Furthermore, both oxidation and gasification reactions can also contribute to SO_x and

NO_x formation as the sulphur and nitrogen build into the char structure are released during char conversion. Various mechanisms were proposed to model sulphur and nitrogen oxides during char conversion, e.g. [39, 40, 41]. For the heterogeneous reactions to occur, the reactant has to first diffuse to the char particle surface, which makes it a relatively slow process. If the boundary layer around the char particle is not resolved, the species diffusion through the boundary layer needs to be modeled. This is done using single-, two- or continuous-film models, which differ from each other by complexity and accuracy by assuming no flame, infinitely-thin flame sheet and finite flame thickness, respectively [42]. Compared to devolatilization, the time scale of the char combustion can be even a few orders of magnitude larger [43]. Since a large fraction of the fuel heating value is contained in char particles, a complete conversion is desired due to economical and efficiency reasons. Because of that, the overall solid fuel conversion rate is usually limited by char combustion. In numerical studies, surface reactions are often described in their global form, as one-step, n -th order reactions. This is the form represented by Eqs. (1.1) - (1.3). A more detailed description of the surface reactions mechanism is given by Langmuir-Hinshelwood type models, which account for elementary steps, such as the reactant adsorption at the active surface area (active sites), heterogeneous conversion and the products desorption. These kind of mechanisms were formulated both for oxidation, e.g. [44, 45, 46], and gasification, e.g. [47, 48], and were proved to be superior to the global n -th order reaction mechanisms as they are able to account for a change in the reaction order as the char conversion progresses and the temperature of the process changes. Another phenomenon that can be described with the Langmuir-Hinshelwood type models is the char reactivity inhibition caused by the presence of hydrogen and carbon monoxide [49], and competition between gasification reactants, CO_2 and H_2O , for the active sites [3].

Heterogeneous reactions occur not only at the external surface of particles but also at the intrinsic surface, i.e. the surface of pores. In fact, the intrinsic surface area is typically much larger than the area of the external particle surface, which means that char is often consumed mostly through reactions inside the pores. This, however, depends on temperature at which the conversion occurs, as well as the particle size. In general, the rate of char conversion can be limited by: the reactant diffusion through the particle boundary layer, the reactant intraparticle (pore) diffusion and the surface reactions kinetics. Depending on which process controls the overall rate, three regimes can be distinguished [43]. At relatively low temperatures, the reactant transport to the particle surface and inside the particle pores is faster than its subsequent consumption. As a consequence, the reactant concentration is constant across the particle and its boundary layer, and the rate of conversion is controlled by the reaction kinetics. This is usually called zone I combustion or

the kinetically-controlled regime. Since the reactant is available inside the pores, the conversion takes place mainly on their surface, which results in a pore structure evolution, increased particle porosity and a decrease of the particle apparent density. In zone II (pore diffusion regime), characteristic for higher temperatures, the conversion rate is controlled by the reactant diffusion inside the particle pores. This means that the reactant is consumed before it has a chance to fully penetrate the pores. As a result, the reactant concentration at the particle external surface is higher than its concentration in the pores and the conversion takes place at the external particle surface as well as on a fraction of the intrinsic surface. This causes both the particle size and the apparent density to decrease during conversion. Finally, if the reaction occurs at high temperatures in zone III, i.e. in the film diffusion regime characterized by very fast kinetics, the conversion rate is controlled by the reactant diffusion through the particle boundary layer. In this regime, there is almost no reactant inside the pores and the reaction occurs on the external particle surface. For that reason, the particle size decreases, while the apparent density remains unchanged. The above-mentioned regimes are illustrated in Fig. 1.5, which shows the char reaction rate as a function of temperature.

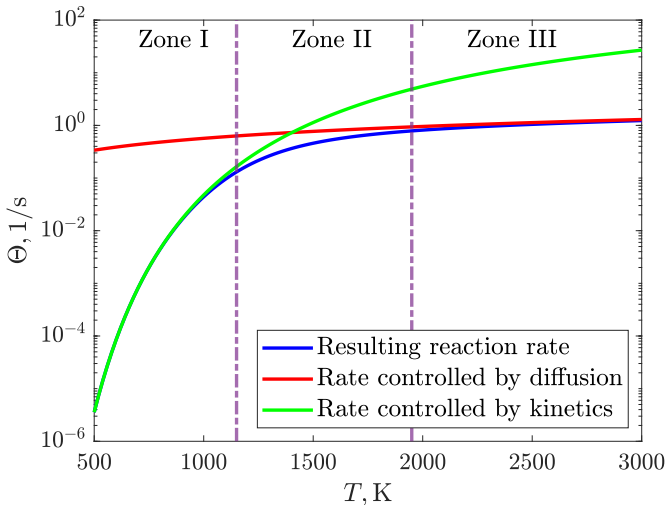


Figure 1.5: Combustion zones/regimes (figure reproduced basen on Fig. 1 in [1])

Pores can be categorized into micro-, meso- and macropores, depending on their size. Even in resolved particle simulations the pores are typically not resolved or the porous structure is represented in a simplified way by assuming symmetrical structure and resolving only the macropores. This is because the porous structure is very complex, its exact shape is usually unknown and it is computationally too expensive to resolve micro- and mesopores (although an attempt was made

to take an X-ray image of a coke particle and resolve it in details using over 0.2 billion cells [50]). There exist several approaches to model intrinsic reactivity. The simplest and least accurate one is to lump all intraparticle phenomena and intrinsic reactivity into empirical kinetic parameters. More complex approaches account for all key phenomena occurring in the particle boundary layer and inside pores. For example, in order to compute the intrinsic reaction rate, the fact that the particle intrinsic surface changes during conversion should be taken into account. Among models that describe this process the Grain Model [51] and the Random Pore Model [52, 53] are probably most popular, although there exist quite a few similar models that describe the intrinsic surface evolution, as reported by Hasse et al. [3]. The output of these models can be used to compute the intrinsic conversion rate, which is the highest rate achieved in conditions corresponding to zone I. This rate can be related to the observed (i.e. real) conversion rate through a parameter called the effectiveness factor. The estimation of the effectiveness factor requires further modeling. The most common approach makes use of so called Thiele modulus [54], which relates the rate of effective pore diffusion with the intrinsic rate. The models that describe the intrinsic reactivity have to be supplemented with additional input parameters determined experimentally, such as the initial char intrinsic surface or pore structural parameters (curvature, variation in cross section area, etc.). Another aspect of the char particle conversion that is considered in advanced models is the particle size and density evolution, often referred to as the mode of burning. As mentioned in the previous paragraph, those changes of the diameter and/or apparent density are regime-dependent, which can be accounted for by relevant models, e.g. [55]. At later stages of conversion the intrinsic reactivity of char is often observed to rapidly decrease [56, 57] under heat treatment. This is caused by several processes leading to rearrangement of the char matrix structure, collectively called thermal annealing or thermal deactivation. Due to this loss of reactivity, the total char burnout takes longer, which is important from the perspective of industrial systems in which a nearly complete conversion is desired [58]. The effect of thermal annealing on char reactivity is typically represented by empirical models in the form of distributed activation energy [59] and semi-global [60, 61] Arrhenius expressions. Finally, at the last stage of conversion the char particle contains significant fraction of mineral matter, which impedes the reactant transport to the reacting part of the particle surface. This phenomenon is called ash inhibition. The effect of the ash inhibition is modeled by considering ash grains built into the char structure and as ash film formed around the carbon core [62, 63]. An accurate description of the char conversion should account for all of the processes and phenomena mentioned in this paragraph. For this purpose, several compound models were developed that assemble selected sub-models into a complete formulation of the char conversion process. The most well-known of

such models is the Carbon Burnout Kinetics model [62] and its multiple derivatives, e.g. [64, 65] .

In practical solid fuel combustion systems, all processes presented schematically in Fig 1.3 happen inside a turbulent fluid and they are affected by the turbulence. The effect of turbulence on the gas phase combustion is well studied. Over the past half century, a large number of numerical models were developed to account for this effect in CFD simulations [66]. Among the best-known ones are the eddy dissipation model [67], the eddy dissipation concept [68], the flamelet model [69], the probability density function model [70] and the conditional moment closure model [71]. Although the above-mentioned models were originally formulated to account for turbulence-chemistry interactions for gas phase combustion, the application of some of them was extended to RANS and LES of pulverized coal combustion, see e.g. [72, 73, 74, 75]. Those extended models include the effect of turbulence on particles conversion indirectly by e.g. affecting particle trajectories or the gas composition around the particle. However, turbulence can also directly affect the heterogeneous reaction by enhancing or attenuating the reactant mass transfer to the particle surface. This is not accounted for in models for the gas phase chemistry adjusted to solid fuel combustion. A closer look at the effect of turbulence on the heterogeneous reaction rate will be taken in the next section.

1.4 The effect of turbulence on the solid fuel conversion rate

Since a large part of this thesis is devoted to study the effect of turbulence on the heterogeneous reaction rate, this section attempts to explain the relationship between turbulence and the conversion rate. This description is based on works of Krüger et al. [76], Haugen et al. [77] and Paper I [2] which is a part of this thesis. The purpose of this section is to give a conceptual and physical background rather than a detailed mathematical formulation, which is given in the aforementioned publications.

First of all, it is important to understand that the only way turbulence can affect the surface reaction rate is through the heat and mass transfer of the reactant towards the particle surface. It is therefore strictly correct to state that the effect of turbulence is on the transfer rate. This in turn can, but does not necessarily have to, have an impact on the conversion rate. This impact depends on the conversion regime the surface reaction occurs in. In the kinetically-controlled regime, practically no effect of turbulence on the conversion rate can be observed, even though the mass transfer rate can be influenced. This is because turbulence cannot affect the reaction kinetics. The effect on the surface reaction rate begins to be noticeable in the pore diffusion regime, but it is only in zone III that *the effect of turbulence on the mass transfer rate* and *the effect of turbulence on the surface reaction rate*

can be used interchangeably. It should be noted that in the presence of multiple surface reactions the situation becomes more complicated as it is common that two different reactions are in different regimes for the same temperature [43]. This is typically the case for oxidation and gasification reactions. At temperatures for which oxidation is already well in the film diffusion regime, gasification can be still controlled by the reaction kinetics or pore diffusion. Under such conditions, turbulence will affect only these reactions that are limited by diffusion, so the net effect of turbulence on the conversion rate will depend on relative contributions from all surface reactions and their regimes.

Having clarified how the effect of turbulence on the reactant transport translates into the effect on the conversion rate, it remains to be explained what is meant by *the effect*. There exist in fact two effects that are opposite to each other. Let's consider a system of monodisperse particles, all with a characteristic response time τ_p , in a turbulent flow in which eddies can be identified by their turnover times τ_{eddy} . Upon interaction between the particles and the eddies, three different scenarios are possible that depend on relative magnitudes of τ_p and τ_{eddy} . These three scenarios (referred to as 'regimes') are situated in the corresponding ranges of the turbulence energy spectrum in Fig. 1.6. The figure shows the case in which τ_p is of the same order as a turnover time of the inertial range (central region in Fig. 1.6) eddy, as in this situation the effect of turbulence is expected to be strongest.

If $\tau_p > \tau_{eddy}$, the particles will not be much affected by the eddies and this will yield a relative velocity between the particles and fluid. A consequence of the relative velocity is the mass transfer enhancement, which is the first effect of turbulence. The second effect is the mass transfer rate reduction, which can occur when $\tau_p \approx \tau_{eddy}$. In these conditions, particles will be thrown out of turbulent eddies and will end up gathered in clusters in low vorticity regions, between the eddies. Since the reactant is quickly consumed inside such clusters due to large particle concentration, the conversion will proceed at a reduced rate owing to the reactant depletion and its impeded transport within the cluster. Therefore, the second effect of turbulence is a decreased mass transfer rate due to turbulence-induced particle clustering. In the last possible scenario, $\tau_p < \tau_{eddy}$, particles adjust very fast to turbulent motions and passively follow the eddies. Under such conditions, turbulence will neither enhance nor reduce the reactant transfer to the particle surface, which means that no effect of turbulence will be observed.

A further clarification is required to as 1) why, according to Fig. 1.6, the effect of turbulence associated with particle clustering is most likely to be caused by inertial range eddies; 2) how the picture presented in Fig. 1.6 will change in the polydisperse particle system. The first point can be explained as follows. For the reactant transfer rate to be reduced as a result of particle clustering, it is required that

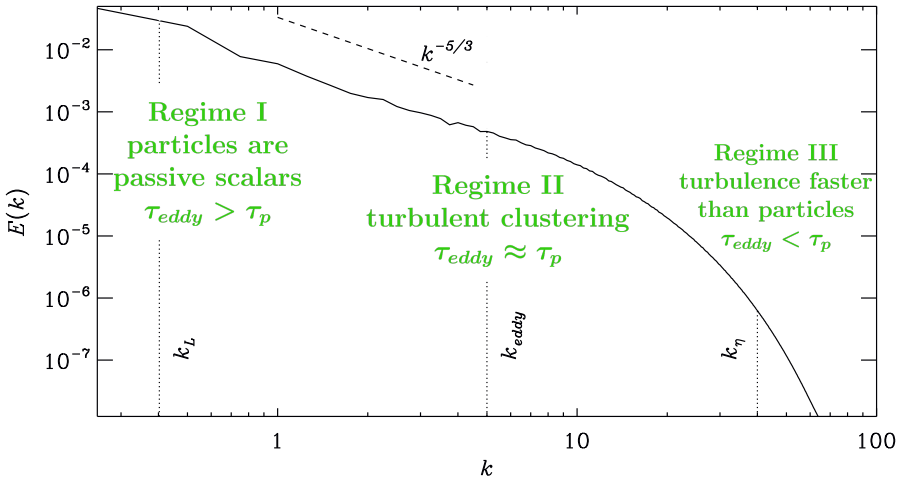


Figure 1.6: Interactions between a particle with a characteristic time scale τ_p and turbulent eddies belonging to different ranges of turbulence energy spectrum (the turbulence energy spectrum reproduced based on Fig. 1 in [2])

clusters are sufficiently dense and that they exist for sufficiently long time. In other words, a high particle number density inside clusters of relatively long lifetimes constitutes the most conducive conditions. It has been confirmed both numerically [78, 79] and experimentally [80, 81] that the strongest clusters are formed by the eddies belonging to the dissipation range (rightmost region in Fig. 1.6). However, the clusters formed by the dissipation range eddies are typically too short-lived to affect the reactant transfer in a significant way. This is why the effect of turbulence associated with particle clustering is most pronounced when the clusters are formed by the inertial range eddies. These clusters are characterized by long enough lifetimes, and sufficiently high particle number densities can occur in this region. Regarding the second point, the picture presented in Fig. 1.6 becomes more complex when a polydisperse particle system is considered. Particles of different sizes are characterized by various response times, which means that a certain range of turbulent scales (or even the entire turbulence energy spectrum if the particle size distribution is broad enough) can contribute to clustering. This topic will be explored in more details in this thesis, as interactions between eddies and polydisperse particles, and the resulting effect on the reactant decay rate, are the subject of Paper I.

1.5 Numerical studies of solid fuels conversion - literature review

Very different aspects of solid fuels conversion have been studied numerically in the literature. Some research is devoted to industrial applications and development of improved solid fuel-based technologies, while the other is very fundamental and focuses on the underlying fuel conversion phenomena. In fact, a great deal has been written on each of the fundamental processes mentioned in Section 1.3 and an extensive review about modeling approaches has recently been published [3]. Furthermore, the literature on the pulverized coal combustion is so abundant that even review publications typically focus on narrower scope, e.g. on pulverized coal combustion in oxy-fuel atmosphere [82] or on modeling of pulverized coal-fired boilers [83]. Given how extensive the field of numerical modeling of solid fuels combustion is, only the most relevant and recent studies will be covered in this section. Since the main numerical approach employed in this work is the point particle DNS and the resolved particle simulation, this section will be limited to review of recent numerical studies on solid fuel conversion in which the flow scales are fully resolved.

1.5.1 Point particle DNS

The main advantage of the DNS approach is that the entire (or, strictly speaking, nearly entire as the grid size is typically of the order of Kolmogorov scales) turbulence energy spectrum is resolved, both spatially and temporally. In the context of reacting flows, this means that all turbulence-chemistry interactions are accounted for directly, without the need of modeling. On the other hand, the major drawback of the DNS is extremely high computational expense. Because of that, the use of the DNS is typically restricted to simple, small-scale domains and relatively low Reynolds number flows. These simple configurations can, nevertheless, provide a great understanding of mechanisms behind certain phenomena, especially when supported with experiments and/or theoretical analysis [84]. Whereas in the past a majority of 2- and 3-dimensional studies on the solid fuel conversion was performed using RANS approach, with the computational power available nowadays it has become feasible to employ LES or even DNS to study situations of practical importance. Currently, LES is often employed in simulations of laboratory-scale pulverized coal burners and furnaces [85, 86, 87, 88, 89], coal and biomass gasifiers [90, 91] or even full-size furnaces [92], while DNS is still restricted to somewhat simpler configurations.

The point particle DNS of pulverized solid fuel combustion is a relatively novel research area, explored mainly in the past decade. The computational effort required to perform e.g. three-dimensional DNS simulation of pulverized coal jet flame is

well illustrated by data provided by Luo et al. [93], who carried out first studies of this type. To examine a coal jet at relatively high Reynolds number (28 284), it took the authors three months on over 1000 cores, i.e. over 2 million CPU hours, to simulate 11 ms of the flow. The occurrence of individual and group combustion regions in the flame was identified and interactions between burning particles and vortices were analyzed. In their later work, the same research group focused on flame structure and its temporal evolution [94], and on the lifted flame stabilization mechanism [95]. Combustion characteristics in the pulverized coal jet flame were also studied by Hara et al. [96], who used a slightly more advanced description of volatile composition and showed that the jet can be divided into layers of pre-mixed and diffusion flames. This research was later extended by Muto et al. [97] to account for the particle shrinkage and swelling.

A number of DNS studies considered a simplified system of a cubic turbulent domain with reacting solid particles distributed randomly or formed into a shear (mixing) layer. These studies are computationally less demanding than the aforementioned simulations of more complex configurations like particle jets, yet they can still provide a valuable insight into solid fuel conversion. Brosh & Chakraborty [98] and Brosh et al. [99] used this set-up to analyse the impact of particle equivalence ratio, velocity fluctuation and particle size on the ignition and subsequent early stage combustion. Muto et al. [100] employed the point particle DNS with the aim to study ignition of pulverized coal in a mixing layer. They were the first to use a detailed chemical mechanism as in all publications mentioned so far in this section, a global, two-step mechanism was used to describe devolatilization, together with a simplified volatile matter composition. Their simulations were, however, two-dimensional thus not being able to account for all features of turbulence, such as e.g. vortex stretching. This was pointed out by Rieth et al. [101] who performed first three-dimensional DNS of pulverized coal combustion in a mixing layer using a detailed chemical mechanism. They found that in the two-dimensional case the volatile matter conversion rate was largely underpredicted due to the small scale mixing not being correctly accounted for in 2D turbulence. The results allowed to analyse in detail the mechanism behind particle ignition and the complex flame structure, in which both premixed and non-premixed modes were distinguished, as well as regions of flame extinction. Most recently, Wen et al. [102] and Shamooni et al. [103] performed DNS of pulverized coal flames in mixing layer combined with detailed gas phase kinetics accounting for typical mechanisms for NO_x formation (prompt, thermal and fuel). Their studies provided a thorough understanding of different pathways through which NO_x is produced. Similar configuration was considered by Wan et al. [104] who employed a detailed mechanism for sodium species to investigate alkali metal emissions during pulverized coal combustion.

Besides the important role of point particle DNS in providing an in-depth understanding of turbulent solid fuel flames, the results of such simulations are also extremely valuable when it comes to development of numerical models. A good example of such application are recent studies on the effects of turbulence on the mass transfer rate [76, 77] (these effects were described in Section 1.4). Krüger et al. [76] employed the point particle DNS to examine the effect of turbulence-induced particle clustering on the reactant consumption rate and proposed a simple model to account for this effect. The model was, however, not closed in a sense that an input parameter was required. The second effect of turbulence, i.e. the mass transfer enhancement due to relative velocity between the particle and fluid, was later described by Haugen et al. [77] with another model derived from physical considerations combined with point particle DNS results. In the same work, the DNS results were also used to formulate a complete, parameter-free model accounting for the combined effect of turbulence. The model in the form proposed by Haugen et al. [77] can be used to incorporate the effect of turbulence on the mass transfer rate into large-scale RANS simulations. The sensitivity of the model predictions to various conditions and parameters and the model application to large scale simulations are considered in this thesis. These aspects are dealt with in Paper II. In their studies, Krüger et al. [76] and Haugen et al. [77] considered a simplified case, in which the reactant was represented by a passive scalar, consumed immediately and isothermally upon reaching the particle surface. The same research group has further extended their work to non-isothermal flow and finite-rate carbon oxidation [105]. This configuration allowed to study not only the isolated effect of turbulence on the mass transfer rate, but also the resulting effect on the conversion rate, which is of practical importance. Krüger et al. [105] also suggested that the effect of particle clustering should be studied in polydisperse particle systems as particles of different sizes exhibit different clustering behavior. This motivated research presented in Paper I.

1.5.2 Resolved particle simulations

The resolved particle DNS of *non*-reactive flows is a quite mature research area. This approach was employed in the past to develop closure models for momentum, heat and kinetic energy exchange, as summarized by Tenneti and Subramaniam [25]. Another typical utilization of resolved particle approach was to test validity of point particle approximation for larger particles and to verify the applicability of empirical expressions commonly used in point particle simulations [17, 106]. Given how much research was carried out, in which non-reactive flows were considered, it may be somewhat surprising that little attention has been paid to reactive flows. Similarly to point particle DNS, most resolved particle studies on solid fuel conversion were conducted over the past decade. The exception was a pioneering

work of Lee et al. [107] who performed transient simulations of the resolved solid fuel particle combustion using the spectral element method a quarter century ago.

It should be noted that many publications exist in which conversion of a spherical particle in a quiescent flow is considered, e.g. [108, 109, 110, 111]. These works take advantage of a spherical symmetry and resolve the particle only in radial direction. Due to much lower computational requirements, several 1D models with detailed description of kinetics and particle morphology have been developed before the emergence of 2D or 3D models with the same level of complexity. In fact, the one-dimensional approach can provide a great insight into fundamental char conversion phenomena and new models are still developed, see e.g. [112, 113]. However, the focus of this section is on two- and three-dimensional studies in which either convection or non-spherical particles are considered. Therefore, one-dimensional models are intentionally omitted here.

Quasi-steady state approach

Due to very different time scales of devolatilization and char combustion, most studies focus on one of these processes. Moreover, since the time scale for char conversion is relatively long, this process is often considered in a pseudo-steady state, where it is assumed that the changes of the particle diameter and/or density are very slow, compared to time scales for convection and diffusion in the gas phase, and can be neglected. Such a steady state assumption was employed by Higuera [114] to study the effect of particle size, Reynolds number and gas compositions on the combustion characteristics. A global reaction mechanism was used together with the assumption that all intraparticle phenomena are lumped into kinetic parameters. The particle temperature evolution over time was also tracked and a very little change over conversion time was observed. A very similar numerical approach was employed by Kestel et al. [115] who investigated the influence of Reynolds number and ambient temperature on the flame sheet formation around 2-mm carbon particle in air. In later work of Kestel et al. [116], a slightly more detailed semi-global mechanism was employed to examine the influence of steam concentration on the oxidation rate. It was found that at sufficiently high steam concentrations and temperatures the region, where the reaction rate is the highest splits from the region of the highest temperature. The effect of steam concentration on the char particle combustion behavior was also examined by Zhang et al. [117]. They adopted almost identical numerical approach to Kestel et al. [115] but explored oxy-fuel atmosphere with different oxygen fractions. A noticeable impact of the steam content on the peak temperature was observed. The results also showed that as the steam concentration is increased, a contribution from oxidation to the overall char consumption rate decreases. Nikrityuk et al. [118] used the same numerical approach as Kestel et al. [115] to demonstrate

that the flame temperature and thickness, as well as the carbon consumption rate are greatly dependent on the choice of heterogeneous kinetics, especially in the kinetically-controlled regime. Their numerical approach was subsequently extended by the same research group to account for radiation in the gas phase and one additional surface reaction. This model was used by Richter et al. [119], who studied conversion of the 200- μm particle in oxy-combustion atmospheres at different Reynolds numbers and ambient gas temperatures. They demonstrated that the inclusion of the gas phase radiation model can result in significant reduction of the particle surface temperature. A shift of the oxidation regime from zone III to zone I was observed as the Reynolds number was increased which resulted in a large enhancement of the oxidation rate. Similar conclusions were drawn by Safronov et al. [120] who performed resolved simulations of 200- μm and 2-mm particles combustion in dry air. It was found that smaller particles burn at higher temperatures and that the transition from zone I to III occurs at lower ambient gas temperatures in the case of larger particles. Safronov et al. [120] also made an attempt to consider some aspects of intraparticle diffusion, although the particle porosity was not accounted for in their model. The first study in which the particle with its internal porous structure was fully resolved was conducted by Richter et al. [121], who considered few porous particle geometries varying in porosity and the specific surface area. They explored the effect of the Stefan flow and homogeneous reactions on the species and heat transfer inside the pores and in the particle boundary layer. It was observed that in the case of small particles the additional internal surface results in the higher conversion rate, while in the same conditions the effect of porosity on conversion of larger particles might be negligible due to much weaker permeability. Later, Richter et al. [122] performed an interesting study on the combustion of a three-dimensional porous carbon particle in O_2/CO_2 atmosphere. A 3D geometry of the 200- μm particle was constructed in a clever way by arranging 185 small particles into a spherical shape. A range of the ambient gas temperature was considered and a non-porous particle was also considered for the purpose of comparison. It was found that the particle agglomerate is never significantly penetrated by gas and that the flame does not move deep into pores even at low ambient temperatures. Xue et al. [123] also employed the pseudo-steady state approach to study conversion characteristics of resolved porous particles with porosity up to 0.4. In their later study [124] a higher porosity (up to 0.9) and different porous structures were considered. Despite a significantly faster diffusion inside the highly porous particles it was observed that the overall carbon consumption rate is much more dependent on the particle size and ambient conditions than on porosity. Another application of resolved pseudo-steady state simulations is to complement large-scale studies and provide a more in-depth understanding of processes analyzed at larger scales. This approach was employed by Richter et al.

[125] who first performed RANS simulations of a laboratory-scale entrained flow gasifier. Then, a few particles located at representative regions in the reactor were selected for fully-resolved analysis in conditions provided by large-scale simulations. Both particles undergoing pyrolysis and char conversion were considered using a numerical model previously formulated by the same research group [119]. The results revealed that in highly reactive regions the Stefan flow might broaden the boundary layer around particles. This, in turn, can significantly modify heat and species transport properties across the boundary layer. Finally, the steady state approach was used by Schulze et al. [126] to investigate combustion and gasification of different multiple particle configurations representing a fixed bed gasifier. A two- and three-dimensional randomly packed beds and a three-dimensional row of particles were simulated. It was shown that 2D configuration captures well all relevant phenomena, as opposed to the particle row. Under conditions corresponding to the real fixed bed gasifier, all considered gasification reactions were observed to be diffusion controlled. The three dimensional resolved simulations of the packed bed have later provided validation of the heat and mass transport model formulated by the same research group [127]. The model has subsequently been used to improve accuracy of kinetic data provided by TGA experiments by accounting for resistance to transport caused by parts of experimental apparatus.

Unsteady studies of devolatilization

By using the pseudo-steady state approximation together with the resolved particle approach, many aspects of char combustion and gasification can be examined in an efficient way. However, the pseudo-steady state assumption fails for non-laminar flows in which transient structures are formed. Furthermore, the approximation becomes invalid for unsteady phenomena and processes that occur at relatively short time scales. An example of such transient, rapidly progressing process is devolatilization. Ignition and devolatilization of a single resolved particle was numerically investigated by Vascellari et al. [128] with the purpose of supplying scalar dissipation rate profiles to be used in the laminar flamelet model. In order to provide transient boundary conditions for resolved simulations, the particle heating rate and trajectory was first computed using Euler-Lagrange approach combined with a detailed devolatilization model. A capability of the flamelet approach supported by resolved simulations to predict the particle ignition was demonstrated. In later work of Vascellari et al. [129], ignition of a resolved particle was simulated in order to validate a new flamelet/progress variable model proposed by the authors. Tufano et al. [130] also investigated devolatilization and ignition of a single coal particle and analyzed the impact of selected species concentrations on the ignition delay. A detailed volatile composition, consisting of light gases and larger hydrocarbons, was obtained from a complex network model. The network model was

also used to adjust kinetic parameters for the single rate law describing the devolatilization rate, and a detailed skeletal mechanism was employed for the gas phase chemistry. A predicted ignition delay was in a good agreement with experimental data. Moreover, it was observed that the ignition takes longer in CO_2/O_2 atmospheres compared to atmospheres composed of N_2/O_2 . In their later works Tufano et al. [131] examined formation of wake flame at higher Reynolds numbers and interactions of volatile flame in particle ensembles. Initial and boundary conditions for the resolved simulations were extracted from LES of a semi-industrial furnace. It was shown that depending on the distance between particles two combustion regimes can be distinguished: group combustion for closely spaced particles and individual combustion at larger inter-particle distances. In vast majority of resolved particle studies, a laminar flow is considered as the flow in a close vicinity to particle is roughly laminar. Nevertheless, some particles in industrial facilities may experience higher turbulence intensity. This motivated further work of Tufano et al. [132], in which the authors investigate the influence of turbulence and higher particle Reynolds number on devolatilization characteristics. They found that higher particle Reynolds numbers result in delayed volatiles ignition and in the flame being shifted to the particle wake. It was also observed that turbulent motions might lead to local flame detachments and extinctions, and that the devolatilization rate can be both reduced and increased due to turbulence. While all of the works mentioned in this paragraph focus on coal particles devolatilization, the resolved particle approach have also been used to investigate pyrolysis of biomass particles [133].

Transient studies of char conversion

Devolatilization is a good example of a fast and transient process that does not fit into the applicability range of a pseudo-steady state assumption. Similarly, certain aspects of char combustion require unsteady approach. In general, the char particle morphology changes during conversion and all component processes are time dependent. Thus, an unsteady approach must be employed in order to account for the evolution of pores and specific surface area, changes to apparent density and the char particle size, or development of the ash layer. These processes were considered in several publications on the resolved particle conversion. Luo et al. [134] proposed a novel immersed boundary method that allows to track the reacting particle radius on a structured, Cartesian grid. Conversion of a 5-mm char particle in air was studied at different particle Reynolds numbers and surface temperatures. The particle morphology was not considered and a semi-global mechanism was used for surface and gas phase reactions. Although the approach was relatively simple, the experimental results were well reproduced by their model. It was observed that at high surface temperatures the flame can detach from the

particle surface and conversion becomes dominated by gasification. The model developed by Luo et al. [134] was later employed by Zhang et al. [135] to investigate how chemical reactions affect the burning char particle drag force. The presence of both gas phase and surface reactions was observed to yield an increased drag force. Based on the results of resolved simulations, a correlation for the drag force was proposed that includes the effect of reactions through two dimensionless parameters. Beckmann et al. [136] studied combustion of a 5.2-mm char particle in air. The particle was represented as an isotropic, continuously porous medium. The intrinsic kinetics and all input parameters required to model the evolution of particle morphology were determined experimentally. Local changes in the specific surface area were modeled using Random Pore Model. A good agreement with the experimentally measured char burnout and evolution of the particle surface temperature was obtained. It was demonstrated that the model was able to predict the ash layer formation, which resulted in a slower char consumption rate in the final stage of conversion. One transient aspect of the char particle conversion not accounted for by Beckmann et al. [136] was the change of the particle size. Both the regression of the particle surface and the evolution of porosity were taken into account in the model developed by Dierich et al. [137] who performed simulations of the resolved particle gasification. Their model additionally included the influence of the Stefan flow inside the particle pores, but the influence of ash and homogeneous reactions were not considered. It was found that at low Reynolds numbers Stefan flow might have a significant effect on the particle boundary layer and that in diffusion-controlled regime the intra-particle Stefan flow impedes the reactant transport into pores. A positive gradient of the porosity in the radial direction was observed, the highest gradient was registered for conversion in zone III. Similar agglomerate porous structure to Richter et al. [122] was considered by Wittig et al. [138] to study how the carbon gasification rate is influenced by various pore size distributions in kinetically-controlled regime. Based on the results, a modification to the Random Pore Model was proposed. A potential for char particles to undergo fragmentation was also explored. Fong et al. [139] indicated that an effective porous continuum might not be a good representation of real char particles due to the presence of large macropores and voids, the effect of which is not well predicted. They further argued that even pore resolved simulations neglect the influence of meso- and micropores and that the typically considered pore structures are excessively idealized. The authors constructed realistic char particle model using X-ray micro-computed tomography and investigated gasification in conditions characteristic to entrained flow gasifiers. Large intra-particle structures were resolved directly, while smaller pores were included through the porous continuum equations. For comparison, an idealized spherical, continuously-porous particle was also simulated. It was shown that in the pore-diffusion regime the species

transfer inside pores is enhanced when large voids and macropores are resolved. The work of Fong et al. [139] was extended by Liang & Singer [140] to oxidation conditions and smaller particles. Effectiveness factors computed based on the resolved simulations for 50 different particles were compared with predictions of different models typically employed in large-scale CFD simulations. It was found that no model is able to correctly predict the effectiveness factor for all char particle types, in particular for particles with complex pore structures. The evolution of char particle morphology was also studied by Nguyen et al. [141] who used similar numerical approach to Beckmann et al. [136]. Various gas temperatures and compositions were analyzed in order to cover a broad range of effectiveness factors. It was found that the evolution of the particle diameter and apparent density, typically described by the mode of burning model, depends simultaneously on the conversion level and the effectiveness factor. Based on the results, new expressions for the input parameters in the mode of burning model were formulated. Furthermore, a modification to the standard Random Pore Model was proposed that extends its applicability to all combustion regimes. Nguyen et al. [142] also conducted transient, resolved study in which the particle shape evolution is tracked using an adaptive mesh algorithm. The conversion of particles of different initial shape in conditions corresponding to a reactive zone inside an industrial entrained-flow gasifier was investigated. The model accounted for intrinsic reactivity through the effectiveness factor and Thiele modulus, but no changes to the specific surface area, apparent density and porosity were considered due to the assumption of film diffusion-controlled conversion. The results showed that the development of the particle shape is strongly dependent on the particle Reynolds number. For typical conditions in entrained-flow gasifiers no significant changes to the shape of spherical particles were observed, however, the shape evolution of non-spherical particles can substantially affect their drag coefficients and trajectories.

The unsteady features of a single char particle combustion were explored by Farazi et al. [143]. In their work, the focus was on early stages of char conversion so the changes in the particle morphology and size were not taken into account. A detailed mechanism was used for homogeneous and heterogeneous chemistry. The influence of variations in oxygen concentrations, particle Reynolds numbers and Damköhler numbers (convective and diffusive) in N_2/O_2 and CO_2/O_2 atmospheres was investigated. Lower conversion rates and temperatures in oxy-fuel atmospheres were observed, and the reason behind that was explored in detail. Furthermore, the authors noticed that it was not enough to study the particle Reynolds number alone as changes in the particle diameter yield different combustion characteristics than changes in the relative velocity. This was associated with relative changes of the convection, diffusion and chemical time scales. The numerical framework of Farazi et al. [143] was later used by Sayadi et al. [144] to exam-

ine combustion of char particle ensembles in oxy-fuel atmosphere. Various vertical and horizontal inter-particle spacing, different array arrangements, oxygen concentrations and particle Reynolds numbers were analyzed. In all cases, the conversion rate of the particle array was observed to be lower compared to the conversion rate of individual particles.

All publications on the resolved particle conversion mentioned so far in this section consider either devolatilization or char combustion. It seems that up to now only in the work of Tufano et al. [38] an attempt was made to take into account all stages of conversion, from heating, through ignition and volatiles combustion, to char particle conversion. The authors employed a detailed description of volatiles yield and composition, and a very complex mechanism for gas phase reactions. For char conversion both gasification and oxidation, as well as thermal annealing reactions were considered. The particle was represented as a porous medium and the model accounted for the evolution of porosity and tortuosity, and intra-particle mass transport by means of convection and diffusion. The experimentally predicted ignition delay was well reproduced by their model. Furthermore, it was found that ignition can occur in one or two steps depending on the oxygen concentration. Contrary to a common assumption, it was demonstrated that char conversion can begin during devolatilization, and that can affect certain devolatilization characteristics.

1.5.3 Literature review - summary

As clearly seen from the literature reviewed in this section, most point particle DNS and transient resolved particle simulations on solid fuel conversion were performed in recent years. The point particle DNS is typically employed to study physics of pulverized coal flames in different conditions or to investigate turbulent solid fuel combustion at a fundamental level. The resolved particle studies, on the other hand, investigate complex conversion processes occurring at a single particle level in laminar flow. The current state of the art are point particle DNS that include detailed kinetics and transient resolved particle DNS that account for complex intra-particle processes.

1.6 Thesis objectives

Two aspects of the solid fuel conversion are investigated in this thesis:

- the effect of turbulence on the conversion rate,
- the combustion behaviour of a resolved carbon particle.

The main objectives of these studies are:

- employing point particle DNS to study the effect of turbulence on the mass transfer rate in polydisperse particle systems,
- investigating the effect of turbulence on the conversion rate in practical, large-scale systems through RANS simulations,
- estimating a sensitivity of this effect to relevant parameters,
- developing an efficient resolved particle DNS model for a single particle combustion,
- gaining a thorough comprehension of the behaviour of the reacting char particle.

The first objective is achieved in Paper I, the second and third objectives are accomplished in Paper II, and the last two objectives are achieved in Paper III.

Chapter 2

Methodology

This chapter discusses selected aspects of the governing equations and numerical methods. In this thesis, solid fuel conversion is considered at different scales. The smallest one, considered in Paper III, is a two-dimensional resolved carbon particle that undergoes conversion in a laminar flow. The medium one, considered in Paper I, is a DNS of isotropic and homogeneous turbulence with reacting Lagrangian particles in a periodic domain. The largest ones, considered in Paper II, are practical turbulent systems (simplified jet burner and industrial-scale boiler) modeled using the Euler-Lagrange approach and RANS equations in their incompressible form. Clearly, three very different numerical approaches are employed in this thesis to study various aspects of solid fuel conversion. Each of these approaches is characterized by a distinct set of equations. Since detailed presentations of the mathematical formulations are given in the papers that form this thesis, only an outline of the relevant methodology is presented here.

2.1 The Pencil Code and its expansion

Resolved particle simulations and point particle DNS were performed using the same solver, called the Pencil Code [145]. Therefore, numerical methods, as well as most of the equations are common for these two cases. The Pencil Code is an open-source solver for compressible flows. The code is multi-purpose and can be adapted to model a broad range of physical phenomena. A clever structure of the code makes it very efficient when employed for massively parallel simulations. This feature is an important benefit when performing point particle DNS on up to 512 cores for high Reynolds number cases. The Pencil Code uses a 6th order finite difference approximation for spatial derivatives and a 3rd order Runge-Kutta scheme for time advancement. While high order methods are necessary for DNS

studies of turbulent flow, there is no such need in the case of the resolved particle in a laminar flow. Nevertheless, the same numerical methods are used for both situations modeled with the Pencil Code. For the point particle DNS described in Paper I, two additional terms were included in the momentum equation that were not present in the resolved particle study presented in Paper III. The first of them was the forcing term, which is the source of large scale kinetic energy in the domain, that prevents the turbulence from decaying. The second term accounted for the particle back reaction to the fluid, and was necessary due to the point particle approximation. This term was non-zero only in those cases in which the two-way coupling was considered. Another main difference between the point particle DNS and the resolved particle numerical models concerns species and chemistry. Five species transport equations (O_2 , CO_2 , CO , N_2 , H_2O) together with the energy equation and a chemical mechanism were included in the resolved particle numerical model, while only a single reactant transport equation was incorporated in the point particle DNS model. There, the reactant was consumed at the catalytic particle surface without any heat being released or absorbed. Several less important differences also exist between the two numerical models established in the Pencil Code. For a detailed description of the numerical approaches, the reader is referred to Paper I (point particle DNS) and Paper III (resolved particle model).

For the resolved particle simulations, it is crucial that all chemical and flow scales in the particle boundary layer are well resolved, which necessitates a very high resolution in the vicinity of the particle. At the same time, the domain should be large enough to avoid confinement effects. In a large part of the domain, outside the flame zone and the particle boundary layer, lower resolution is desired in order not to compromise efficiency of the code. In the Pencil Code, a local grid refinement in the boundary layer was achieved using the overset grid approach, i.e. the particle was surrounded by a body-fitted, cylindrical grid (aka 'the ogrid') with a non-uniform grid spacing in the radial direction, while the part of the domain further away from the particle was resolved on a much coarser Cartesian grid. Interpolation between the ogrid and the Cartesian grid was accomplished using 4th order Lagrange polynomials. Explicit method of interpolation was employed, which means that there is no overlap between the interpolation zone on the ogrid and the interpolation stencil on the Cartesian grid. A schematic representation of the domain for the resolved particle case and the interpolation strategy is shown in Fig. 2.1. This framework is used for all investigations described in Paper III. Detailed information about the overset grid used in the Pencil Code is given by Aarnes et al. [146, 147].

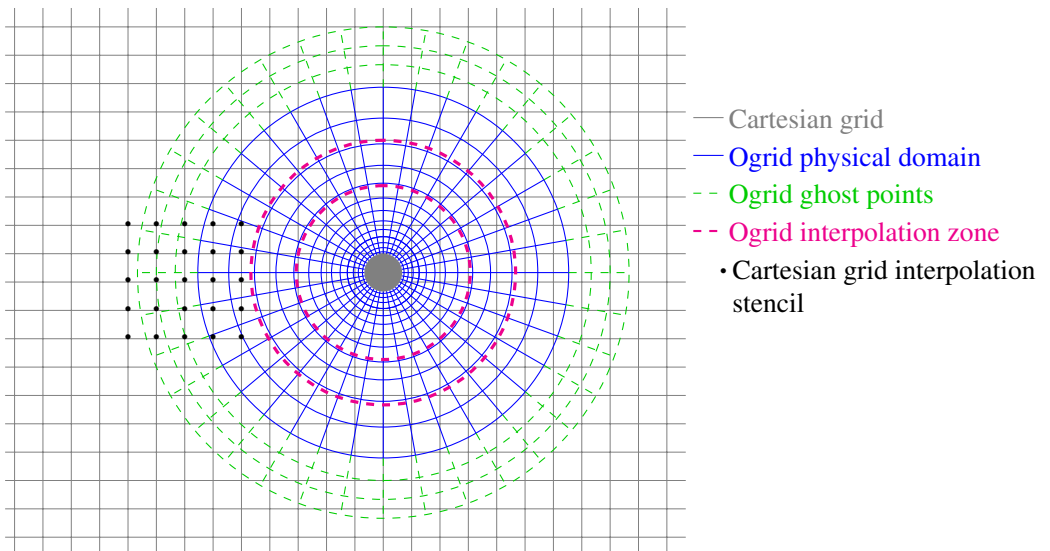


Figure 2.1: Schematic representation of a domain for the resolved particle case (not drawn to scale). A grey circle in the middle represents the particle, interior of which is not resolved. An exemplary 4th order interpolation stencil (black dots) is also shown. $n + 1$ grid points in each spatial direction (d) are needed for n^{th} order interpolation, such that the interpolation stencil consists of the $(n + 1)^d$ points that are situated closest to the receiver point, to which a function is interpolated to. The interpolation zone on the ogrid (the region bounded by pink dashed lines) is chosen in such a way that none of the points belonging to the interpolation stencil on the Cartesian grid is located inside the interpolation zone on the ogrid.

2.1.1 Development of the numerical model used in Paper III

For point particle DNS, use was made of modules and subroutines already existing in the Pencil Code, while a new framework was developed to carry out the resolved particle investigations. The code development, carried out within this thesis, included implementation of:

- energy equation on the ogrid
- simplified chemistry module
- relevant boundary conditions at the particle surface

The energy equation was implemented using temperature as a dynamical variable and the assumption was made that the viscous heating and gas phase radiation can be neglected. The radiative heat transfer between the gas phase and particle was

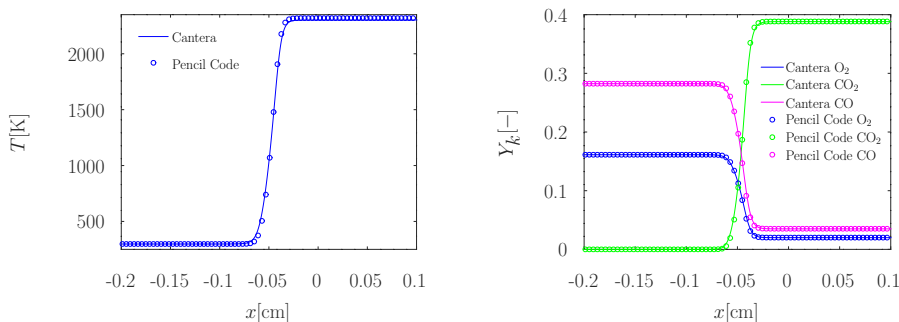


Figure 2.2: Comparison of 1D profiles of temperature (left) and species mass fractions (right)

also omitted as a constant temperature was specified at the particle surface. This boundary condition for temperature is certainly not true in reality and a rigorous approach accounting for all heat transfer mechanisms would show that the surface temperature is changing during particle combustion, as already shown by many studies. Nevertheless, a constant temperature was specified at the surface for the purpose of validation against an experiment [148] conducted with a fixed particle surface temperature, as explained in Paper III.

The simplified chemistry module accounts for one, reversible reaction in the gas phase, i.e. oxidation of CO to CO_2 . In order to verify the implementation of the gas phase reaction into the Pencil Code, the same mechanism was implemented in the Cantera software, which was developed for modeling chemically reactive systems. A one-dimensional flame was simulated; the results, in the form of profiles of temperature and species mass fractions, are compared in Fig. 2.2. It can be seen that the results obtained from the Pencil Code and Cantera are in very close agreement. It should be mentioned, though, that the correct implementation of the mechanism does not mean that the obtained flame profile is a good reflection of reality. Due to the fact that the global mechanism is not able to represent a real reaction pathway and formation of intermediate species, the resulting flame is too thin, which also leads to the flame speed being overpredicted.

Two surface reactions, oxidation and CO_2 gasification are currently included. These reactions affect the gas phase through the boundary conditions at the particle surface. Since the surface temperature is maintained constant, only species concentrations and velocity are directly influenced. The velocity at the surface is computed as the net outflow of species produced during heterogeneous reactions, while for species a balance between their production and diffusion is assumed.

Implementation of boundary condition for species

A simple iterative algorithm is employed for finding species mass fractions at the particle surface. Since the algorithm was not explained in Paper III, the details of the implementation are given in this section. For the impenetrable particle (i.e. the particle which interior is not resolved), the species balance can be expressed as [134]:

$$\rho D_k \frac{\partial Y_k}{\partial r} + \dot{m}_C Y_k + \dot{m}_k = 0, \quad (2.1)$$

where ρ represents the density of the mixture, \dot{m}_C is the carbon consumption rate, Y_k is the k^{th} species mass fraction, D_k is its diffusion coefficient and \dot{m}_k is its rate of production. For reactants (O_2 and CO_2) \dot{m}_k is given by:

$$\dot{m}_k = -\rho Y_k B_j \exp(-E_j/RT), \quad (2.2)$$

where B_j and E_j are kinetic parameters of reaction j , T is temperature and R represents the gas constant. For the mechanism implemented in the simplified chemistry module, the CO production rate can be computed as:

$$\dot{m}_{\text{CO}} = -\frac{2M_{\text{CO}}}{M_{\text{CO}_2}} \dot{m}_{\text{CO}_2} - \frac{2M_{\text{CO}}}{M_{\text{O}_2}} \dot{m}_{\text{O}_2}, \quad (2.3)$$

where M_k are molar masses. The char conversion rate can then be obtained from

$$\dot{m}_C = -(\dot{m}_{\text{O}_2} + \dot{m}_{\text{CO}_2} + \dot{m}_{\text{CO}}). \quad (2.4)$$

A gradient of the arbitrary variable ϕ at the particle surface can be represented by a one-sided finite difference scheme as:

$$\nabla \phi = \frac{1}{\Delta r} \sum_{i=1}^n \alpha_i \phi_i, \quad (2.5)$$

where the summation is over n cells and starts at the boundary at which $i = 1$; Δr is the size of the first cell in the radial direction and α_i are coefficients whose magnitudes depend on the order of the employed numerical scheme. In the Pencil Code, a 6th order scheme is used and the coefficients are given in Tab. 2.1. A one-sided formulation for the gradient given by Eq. (2.5), with coefficients from Tab. 2.1, is different from the summation-by-parts approach initially implemented by Aarnes et al. [146, 147] in the Pencil Code. It was observed that for the reactive case, the summation-by-parts boundary condition might yield additional numerical instabilities. Therefore, a traditional one-sided finite difference formula was used instead.

i	1	2	3	4	5	6	7
α_i	-49/20	6	-15/2	20/3	-15/4	6/5	-1/6

Table 2.1: Coefficients for one-sided 6th order finite difference scheme

By defining $r_j = B_j \exp(-E_j/RT)$ and substituting Eqs. (2.2)-(2.5) into Eq. (2.1) for O₂ and CO₂ one obtains:

$$\frac{D_{O_2}}{\Delta r} \sum_{i=1}^n \alpha_i Y_{O_2,i} - \left(\frac{2M_C}{M_{O_2}} Y_{O_2,1} r_{O_2} + \frac{M_C}{M_{CO_2}} Y_{CO_2,1} r_{CO_2} \right) Y_{O_2,1} +$$

$$-Y_{O_2,1} r_{O_2} = 0, \quad (2.6)$$

$$\frac{D_{CO_2}}{\Delta r} \sum_{i=1}^n \alpha_i Y_{CO_2,i} - \left(\frac{2M_C}{M_{O_2}} Y_{O_2,1} r_{O_2} + \frac{M_C}{M_{CO_2}} Y_{CO_2,1} r_{CO_2} \right) Y_{CO_2,1} +$$

$$-Y_{CO_2,1} r_{CO_2} = 0, \quad (2.7)$$

which can be rearranged to:

$$Y_{O_2,1}^2 \underbrace{\left(-\frac{2M_C}{M_{O_2}} r_{O_2} \right)}_{= A_{O_2}} + Y_{O_2,1} \underbrace{\left(\frac{D_{O_2}}{\alpha_1 \Delta r} - \frac{M_C}{M_{CO_2}} Y_{CO_2,1} r_{CO_2} - r_{O_2} \right)}_{= B_{O_2}} +$$

$$+ \underbrace{\frac{D_{O_2}}{\Delta r} \sum_{i=2}^n \alpha_i Y_{O_2,i}}_{= C_{O_2}} = 0 \quad (2.8)$$

$$Y_{CO_2,1}^2 \underbrace{\left(-\frac{M_C}{M_{CO_2}} r_{CO_2} \right)}_{= A_{CO_2}} + Y_{CO_2,1} \underbrace{\left(\frac{D_{CO_2}}{\alpha_1 \Delta r} - \frac{2M_C}{M_{O_2}} Y_{O_2,1} r_{O_2} - r_{CO_2} \right)}_{= B_{CO_2}} +$$

$$+ \underbrace{\frac{D_{CO_2}}{\Delta r} \sum_{i=2}^n \alpha_i Y_{CO_2,i}}_{= C_{CO_2}} = 0. \quad (2.9)$$

Eqs. (2.8) and (2.9) are quadratic expressions for Y_{CO_2} and Y_{O_2} at the particle surface. Both equations contain the product term $Y_{\text{CO}_2}Y_{\text{O}_2}$, which makes it impossible to solve them separately and brings the need of an iterative solution. In order to solve Eqs. (2.8) and (2.9) simultaneously, the following procedure is repeated for every grid point belonging to the particle surface:

- the range for possible solutions is chosen to be $[Y_{\min}, Y_{\max}] = [0, 1]$
- two solutions for Y_{O_2} are chosen: $Y_{\text{O}_2,\text{left}}$ and $Y_{\text{O}_2,\text{right}}$ such that

$$Y_{\text{O}_2,\text{left}} = Y_{\min} + q(Y_{\max} - Y_{\min}),$$

$$Y_{\text{O}_2,\text{right}} = Y_{\max} - q(Y_{\max} - Y_{\min}),$$
 where $q = (3 - \sqrt{5})/2$ is the golden ratio coefficient
- the chosen solutions are substituted into Eq. (2.9) which allows to solve for $Y_{\text{CO}_2,\text{left}}$ and $Y_{\text{CO}_2,\text{right}}$: $Y_{\text{CO}_2} = \frac{-B_{\text{CO}_2} \pm \sqrt{B_{\text{CO}_2}^2 - 4A_{\text{CO}_2}C_{\text{CO}_2}}}{2A_{\text{CO}_2}}$ (the solution which belongs to $[Y_{\min}, Y_{\max}]$ is selected)
- $Y_{\text{CO}_2,\text{left}}$ and $Y_{\text{CO}_2,\text{right}}$ are substituted into Eq. (2.8) from which $Y_{\text{O}_2,\text{left}}^*$ and $Y_{\text{O}_2,\text{right}}^*$ are solved for: $Y_{\text{O}_2}^* = \frac{-B_{\text{O}_2} \pm \sqrt{B_{\text{O}_2}^2 - 4A_{\text{O}_2}C_{\text{O}_2}}}{2A_{\text{O}_2}}$ (the solution which belongs to $[Y_{\min}, Y_{\max}]$ is selected)
- the relative error, δ , for both solutions is computed as $\delta = \frac{|Y_{\text{O}_2} - Y_{\text{O}_2}^*|}{Y_{\text{O}_2}^*}$
- if the relative error is greater than the chosen tolerance level ($\delta < 1e - 8$), a new solution range is defined as:

$$[Y_{\min}, Y_{\max}] = [Y_{\min}, Y_{\text{O}_2,\text{right}}] \text{ if } \delta_{\text{right}} > \delta_{\text{left}}$$
 or

$$[Y_{\min}, Y_{\max}] = [Y_{\text{O}_2,\text{left}}, Y_{\max}] \text{ if } \delta_{\text{right}} < \delta_{\text{left}}$$
 and the steps described above are repeated for the new range
- if the relative error is smaller than the chosen tolerance level the assumed solution is accepted as a correct one for the considered grid point.

Once Y_{O_2} and Y_{CO_2} at the boundary are known for every cell on the particle surface, \dot{m}_{CO} and \dot{m}_{C} are obtained from Eqs. (2.3) and (2.4). Subsequently, the remaining species mass fractions can be solved directly from Eq. (2.1), which can be rearranged as:

$$Y_{k,1} = \frac{-(\dot{m}_k \Delta r + \rho D_k \sum_{i=2}^n \alpha_i Y_{k,i})}{\alpha_1 \rho D_k + \dot{m}_c \Delta r}. \quad (2.10)$$

2.2 Numerical model for large-scale simulations

This section provides a brief overview of the numerical models that were used for the large scale systems simulated in Paper II. Large-scale simulations of practical systems have been performed using the commercial software ANSYS-Fluent, taking advantage of its User Defined Function (UDF) functionality. For these cases, a simplified numerical model was employed based on incompressible flow and a steady-state assumption. The Euler-Lagrange approach was used, where the particles motion was described using the Discrete Phase model available in Fluent. A characteristic feature of this model is that it tracks particle parcels (i.e. collections of particles of the same size), rather than individual particles. Turbulent dispersion of particles was accounted for by the Discrete Random Walk Model. Turbulence was modelled using the standard $k - \epsilon$ model, while the Discrete Ordinates model was utilized for radiative heat transfer. Constant rate devolatilization was considered with a simplified one-step description for the volatiles combustion. Turbulence-chemistry interaction was accounted for by a Finite-Rate/Eddy-Dissipation model, supplied by Fluent. A single surface oxidation reaction was considered, the product being CO_2 in the simplified jet burner case and CO for the large scale boiler. In the latter case, oxidation of CO to CO_2 was additionally included. The surface reaction rate was predicted by the kinetic-diffusion model, which assumes that the rate is limited by whatever process is slower: diffusion of reactant to the particle surface or the consumption rate due to the reaction kinetics. The effect of turbulence was accounted for by the model formulated by Haugen et al. [77]. The model was implemented as a modification to the diffusion-controlled reaction rate through the UDF, using `DEFINE_PR_RATE` function, predefined in ANSYS-Fluent. The exact content of the UDF can be accessed through the supplementary material attached to Paper II.

Chapter 3

Contributions

This chapters summarizes the author's publications. This thesis is based on three papers, two of which are already published in international, peer-reviewed journals, while the last one has been recently submitted and is now under review. Since all three papers are co-authored, the author's contribution in each publication is explained. Different aspects of solid fuel conversion have been considered with the main focus being on the effect of turbulence on the surface reaction rate and the conversion characteristics of a resolved carbon particle.

3.1 Summary of Paper I

Contributions: The author's responsibility was to perform simulations, post-process the results and prepare the manuscript. A great deal of guidance throughout the entire process was provided by Nils Erland L. Haugen, who formulated the research goals, suggested ways to analyse the results and helped with their interpretation, and who taught the author how to use the code and the post-processing software. The manuscript was written by the author with help from Nils Erland L. Haugen. The manuscript was thoroughly reviewed by Adam Klimanek.

This paper is an extension of the studies performed by Krüger et al. [76] and Haugen et al. [77] to polydisperse particle systems. The paper aims to study how turbulence affects the mass transfer rate between the fluid and inertial particles and how this can possibly influence the net surface reaction rate. The goal was also to verify if a model formulated to account for the effect of turbulence in monodisperse particle systems is still applicable when polydisperse particles are considered. Since the particle clustering is due to those eddies that have similar time scales to the particle response time, for polydisperse systems with a broad particle

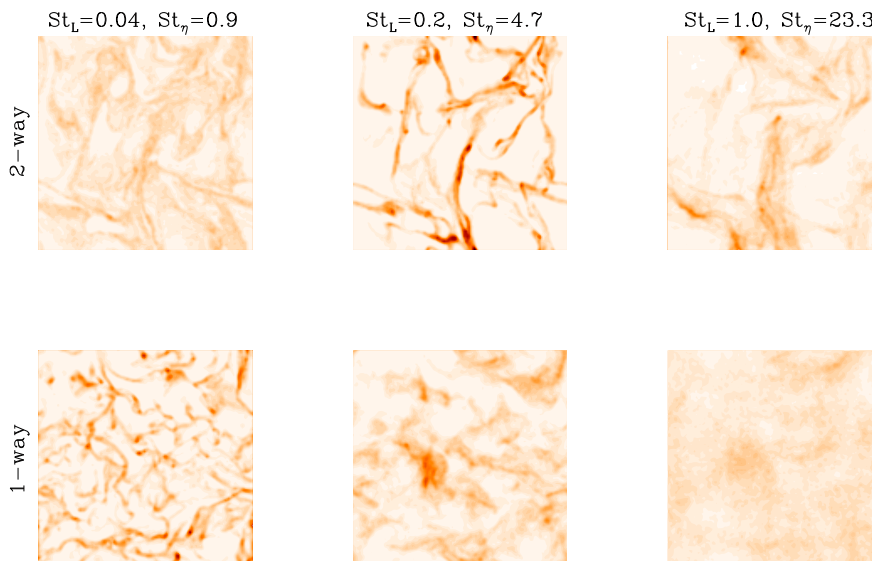


Figure 3.1: Particle number density for different particle sizes. The particle size grows from left to right. Upper row: 2-way coupling, lower row: 1-way coupling (figure reproduced from [2])

size distribution all scales of turbulence can contribute to clustering. This is very different from monodisperse systems, in which only a small fraction of turbulent eddies is responsible for cluster formation.

Point particle DNS of a cubic domain with homogeneous and isotropic turbulence were performed over a range of parameters such as Damköhler (Da), (mean) Stokes (St) and Reynolds numbers. In order to separate the effect of turbulence, it was assumed that the reaction is unimolecular, isothermal and fully controlled by diffusion, i.e. the reactant is consumed infinitely fast upon reaching the particle surface. A few additional aspects of the numerical model employed to perform these simulations are discussed in Section 2.1. Three different distributions of particle size were considered, and the effect of particle back-reaction was examined by comparing cases with fluid-particle coupling modeled as one-way and two-way. The results did not show any significant dependence on the particle size distribution. It was observed that the back-reaction of particle momentum to the fluid can contribute to the mass transfer rate reduction. This happens at high mass loading, whereas for low mass loading the mass transfer rate is reduced to almost the same degree as when the particle back-reaction is neglected. It was found that

there exists a correlation between locations of clusters that are made of particles with different sizes, as can be observed in Fig. 3.1 which shows particle number density corresponding to three different particle sizes. This came as a surprise because different eddies lead to clustering of particles of different sizes, e.g. small eddies (with short time scales) cause clustering of small particles ($\tau_p \approx \tau_{eddy}$), but not the large ones ($\tau_p \gg \tau_{eddy}$). The correlation is stronger when the fluid-particles momentum exchange is two-way. Other consequences of the particle back-reaction is a stronger tendency to clustering and a change of the cluster length scales, as well as a larger non-uniformity in the reactant distribution, which leads to a slower conversion rate. For the surface reaction rates, very similar results to those presented by Haugen et al. [77] were obtained, which means that the effect of turbulence on the surface reaction rate can be equally strong in mono- and poly-disperse particle systems. In particular, at low (high) Damköhler numbers the mass transfer rate is increased (decreased) by turbulence. Despite the fact that clusters are 'sharpest' when they are formed by the dissipation-range eddies ($St_\eta \sim 1$, where the Stokes number is based on the Kolmogorov scale), the effect of particle clustering is strongest when clustering is caused by inertial-range eddies. The reason for that is longer life times of clusters at higher Stokes numbers.

3.2 Summary of Paper II

Contributions: The initial idea for this research was proposed by Adam Klimanek. The User Defined Function that couples the model for the effect of turbulence with ANSYS Fluent was written by Øyvind Langørgen. Setting-up the simulations, post-processing of the results and manuscript writing was a common effort of the author and Adam Klimanek. Every step of the work was closely supervised by Nils Erland L. Haugen, who provided lots of valuable feedback and suggestions, and who also contributed to the discussion on the model sensitivity. The final manuscript was reviewed by Sławomir Sładek.

This paper is a continuation of studies on the effect of turbulence on the mass transfer rate. The aim was to verify theoretical predictions in real situations and apply the model that accounts for the effect of turbulence to practical, large-scale systems. The model was implemented as a modification to the reaction rate due to diffusion in the kinetic-diffusion model for surface combustion. A succinct description of the numerical approach is presented in Section 2.2. Both effects of turbulence were accounted for by the model, i.e. the mass transfer rate decrease due to particle clustering and the mass transfer rate increase due to relative velocity between particles and fluid. First, theoretical estimations were performed to assess at which conditions the effect of turbulence is most pronounced and to which parameters it is most sensitive to. It was found that, at stoichiometric con-

ditions, the effect of turbulence associated with particle clustering depends on the fuel type and atmospheric composition. For example, the surface reaction rate can potentially be reduced much more for ilmenite particles and 100% H_2O atmosphere than for carbon particles in air. Also, turbulence characteristics, such as its intensity and length scale were shown to influence the reaction rate. A simplified CFD model of a jet burner was developed to verify theoretical predictions and investigate the influence of mass flow rate, particle size and jet inlet velocity. As expected, a significant reduction of the conversion rate due to particle clustering was observed in cases with mass flow rates corresponding to around-stoichiometric and fuel-rich mixtures. This is because these cases are characterised by relatively high Damköhler numbers. For the same reason, the effect of clustering is stronger at lower jet inlet velocities. Contrary to theoretical predictions, no significant influence of the particle size on the conversion rate was observed. It turned out that variations in some parameters, such as the particle diameter, can shift the combustion regime towards more kinetically or diffusion-controlled. As a consequence, the effect of turbulence on the mass transfer rate does not directly translate into the effect on the overall conversion rate.

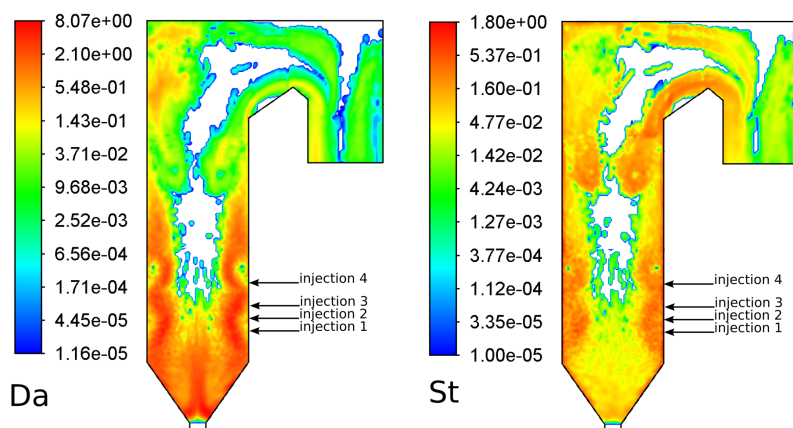


Figure 3.2: Distribution of Damköhler and Stokes numbers inside the investigated practical system (figure reproduced from [1]). The strongest effect of particle clustering is expected to be observed at high Da and at $St \sim 0.1$ (in lower parts of the boiler and around injections), while the effect associated with relative velocity is expected to be most pronounced at relatively low Da , in the upper part of the domain. White areas are regions with no particles.

A real practical system, in the form of a pulverized coal fired boiler was investigated. Although the effect of turbulence on the conversion rate can be predicted once Damköhler and Stokes numbers are known, it is not possible to determine it

in advance in real systems due to the fact that such systems are characterized by a broad range of Da and St , as can be seen in Fig. 3.2, which shows a distribution of Damköhler and Stokes numbers inside the boiler. This also means that turbulence can have opposing effects on the conversion rate in different regions of the domain. For the particular case under investigation, it was found that the dominating effect of turbulence is particle clustering, which accounts, on the net basis, for around 17% reduction of the mass transfer rate. The net surface reaction rate was, however, reduced only by 2% due to the reaction being in the kinetically-controlled regime.

3.3 Summary of Paper III

Contributions: The research idea was proposed by Nils Erland L. Haugen, who also provided the author with assistance and guidance during development of the numerical model. This included suggestions on the details of the numerical approach, multiple coding sessions, code testing and advice on how to deal with unexpected numerical issues. The author carried out simulations, post-processed the results and wrote the manuscript. The entire process was closely supervised by Adam Klimanek who provided valuable feedback and suggestions during weekly discussions.

This paper takes a different perspective on the solid fuel conversion than the two publications described above. An efficient approach to carry out resolved particle simulations of solid fuel combustion was proposed and the model was implemented into the framework of the Pencil Code, as explained in Section 2.1. A body-fitted, cylindrical grid, also presented in Section 2.1, was used to resolve the particle and its boundary layer. An advantage of such mesh is that it gives the possibility to implement boundary conditions in a straightforward way and to increase the resolution close to the particle, where the flame is formed. Furthermore, two unconventional aspects of the numerical model are that 1) all transport coefficients were fitted to match predictions of the kinetic theory; 2) the speed of sound was reduced to relax time step and grid size requirements. These two aspects, together with the simplified chemical mechanism, resulted in a good overall efficiency of the model. The model was validated against numerical [134] and experimental [148] results. This was done by performing two dimensional simulations of carbon particle combustion in air, in conditions corresponding to a laminar flow and a quasi-steady state. A decent accuracy was achieved although not all features of the experimental results were correctly predicted. Possible shortcomings of the model that could lead to these discrepancies were identified. Furthermore, a cross code validation was performed between the model implemented into the Pencil Code and a model developed within this study using ANSYS Fluent. The comparison of

reaction rates showed a very good agreement between the two codes confirming no errors at the implementation stage. A dependence of the conversion rate on various parameters, such as diffusion coefficients and reaction rates, was investigated. It was shown that the conversion rate is mostly affected by the oxygen diffusivity, which is due to the fact that for most of the studied cases the conversion occurred in the diffusion-controlled regime. Two diffusion-controlled limits for the reaction rate were identified. The first one was associated with the oxygen diffusion to the particle surface. The second one was reached at higher temperatures at which the flame detaches from the particle. This limit was associated with the oxygen diffusion to the flame zone. It was also observed that the flame thickness and its tendency to detach from the particle surface are strongly affected by the gas phase reaction rate, as shown in Fig. 3.3.

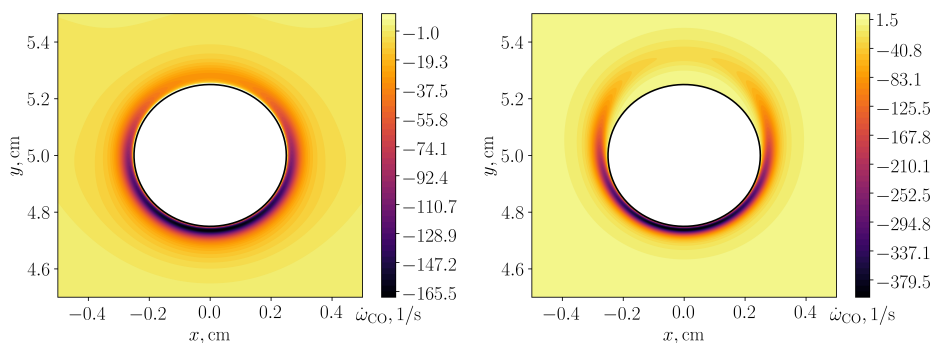


Figure 3.3: Contours of carbon monoxide flame, left: gas phase reaction rate reduced by a factor of 2, right: gas phase reaction rate increased by a factor of 2

3.4 Other contributions

The author had also a minute contribution in work that led to the following papers (1-3) and conference publications and presentations (4-10):

1. Nils E.L. Haugen, Jonas Krüger, Jørgen R. Aarnes, Ewa Karchniwy, Adam Klimanek (2021). *Thermophoresis and its effect on particle deposition on a cylinder for low and moderate Reynolds numbers*. International Journal of Heat and Mass Transfer, 181, 121996.
2. Sławomir Śladek, Agnieszka Korus, Adam Klimanek, Ewa Karchniwy, Wojciech P. Adamczyk, Andrzej Szlęk (2021). *Measurements of surface temperature distribution at coal dust particles*. Energy, 243, 123025.
3. The Pencil Code Collaboration, Axel Brandenburg, Anders Johansen, Philippe A. Bourdin, Wolfgang Dobler, Wladimir Lyra, Matthias Rheinhardt, Sven Bingert,

Nils Erland L. Haugen, Antony Mee, Frederick Gent, Natalia Babkovskaia, Chao-Chin Yang, Tobias Heinemann, Boris Dintrans, Dhruvaditya Mitra, Simon Candelaresi, Jörn Warnecke, Petri J. Käpylä, Andreas Schreiber, Piyali Chatterjee, Maarit J. Käpylä, Xiang-Yu Li, Jonas Krüger, Jørgen R. Aarnes, Graeme R. Sarrson, Jeffrey S. Oishi, Jennifer Schober, Raphaël Plasson, Christer Sandin, Ewa Karchniwy, Luiz Felipe S. Rodrigues, Alexander Hubbard, Gustavo Guerrero, Andrew Snodin, Illa R. Losada, Johannes Pekkilä, Chengeng Qian (2021). *The Pencil Code, a modular MPI code for partial differential equations and particles: multipurpose and multiuser-maintained*. Journal of Open Source Software, 6(58), 2807.

4. Ewa Karchniwy, Adam Klimanek, Nils E.L. Haugen (2018). *The effect of turbulence on mass transfer rates between inertial particles and fluid for polydisperse particle size distributions*. In: Book of abstracts of Joint meeting of the Polish and Scandinavian-Nordic Sections of the Combustion Institute: PSN 2018, Kraków, 6-7 September 2018 (p. 173-175).

5. Nils E.L. Haugen, Jonas Krüger, Ewa Karchniwy, Patrycja Zaręba, Terese Løvås, Tian Li, Adam Klimanek (2019). *The effect of turbulence on the reactant mass transfer to pulverized char*. In: Book of abstracts of 17th International Conference on Numerical Combustion, Aachen, 6-8 May 2019 (p. 105).

6. Ewa Karchniwy, Nils E.L. Haugen, Adam Klimanek (2019). *RANS modelling of the effect of turbulence on heterogeneous reaction in pulverized coal combustion*. In: The book of abstracts of XXIV International Symposium on Combustion Processes, Wrocław, 23-25 September 2019 (p. 64-65).

7. Ewa Karchniwy, Sławomir Śladek, Adam Klimanek, Andrzej Szłek, Wojciech Adamczyk, Agnieszka Korus (2020). *The effect of surface temperature distribution on net force acting on reacting particles*. In: Proceedings of the 6th International Conference Contemporary Problems of Thermal Engineering : CPOTE 2020, Poland, 21-24 September 2020 (p. 301-307).

8. Sławomir Śladek, Adam Klimanek, Ewa Karchniwy, Wojciech Adamczyk, Agnieszka Korus, Andrzej Szłek (2020). *Measurements of coal particle surface temperature distribution*. In: Proceedings of the 6th International Conference Contemporary Problems of Thermal Engineering : CPOTE 2020, Poland, 21-24 September 2020 (p. 309-315).

9. Ewa Karchniwy, Sławomir Śladek, Adam Klimanek, Andrzej Szłek, Agnieszka Korus, Wojciech Adamczyk (2021). *Influence of Surface Temperature Distribution on Reaction Rate of Solid Fuel Char Particles*. In: Proceedings of the 7th World Congress on Mechanical, Chemical, and Material Engineering (MCM'21), 2-4

August, 2021, Virtual Conference.

10. Ewa Karchniwy, Adam Klimanek, Sławomir Śladek, Andrzej Szlęk, Agnieszka Korus, Wojciech Adamczyk (2021). *The Effect of Particles Surface Temperature Distribution in Numerical Modelling Of High Scale Combustion and Gasification Chambers*. In: Proceedings of the 7th World Congress on Mechanical, Chemical, and Material Engineering (MCM'21), 2-4 August, 2021, Virtual Conference.

Chapter 4

Thesis summary

4.1 Conclusions

In this thesis conversion of char/carbon particles was analyzed at three different scales. At each scale, different numerical approach was employed. Initially, the effect of turbulence on the mass transfer rate in polydisperse particle systems was studied. A broad range of Stokes and Damköhler numbers was analyzed. The back-reaction of particle momentum to fluid was observed to significantly increase clusters strength at Stokes numbers higher than ~ 0.1 and to reinforce a correlation between clusters made of particles of different sizes. It was demonstrated that a dependence of the effect of turbulence on St and Da is very similar to what was observed in the case of monodisperse particle systems, i.e. at low Da the mass transfer is enhanced due to turbulent motions contributing to the relative velocity between particles and fluid, while at higher Da the reactant consumption is slowed down due to particle clustering. This means that the model, developed under the assumption of monodisperse particles, is also capable to predict the effect of turbulence on the mass transfer rate in polydisperse particle systems. Theoretical analysis revealed that under certain conditions particle clustering might have a non-negligible influence on the conversion rate in practical systems. In particular, a fuel-rich mixture or a mixture characterized by low stoichiometric air-fuel ratio were identified as most promising conditions, although the size of particles and of the considered system, as well as characteristics of turbulence might also play a role. These conclusions motivated further research on the effect of turbulence in large-scale facilities. The first large-scale system that was investigated was a simplified jet burner. These studies showed that, in some cases, when the effect of turbulence is accounted for, the particles travel much further before reaching a full conversion. This information is important as industrial systems are typically

optimized to be large enough to allow for as high conversion as possible to maximize the efficiency, but not much larger to minimize construction and maintenance costs. Therefore, whenever RANS simulations are involved in the design and optimization process, the effect associated with particle clustering should be taken into account. A high potential for turbulence to affect the mass transfer has been observed for quite a broad range of studied conditions and parameters, especially in systems characterized by relatively large particles and high mass flow rates. Finally, the effect of turbulence was for the first time investigated in a real, industrial-scale system. In such a system both the Stokes number and the Damköhler number typically differ by several orders of magnitude within the domain, making it impossible to make a priori predictions about the resulting net effect of turbulence on the mass transfer rate. In the simulated boiler, large regions of both enhanced and reduced mass transfer due to turbulence have been observed. The net average effect turned out to be a significant ($\sim 20\%$) mass transfer rate decrease. This, however, did not translate into the slower conversion rate, which was found to be reduced barely by 2% on average. The reason for this was indicated as too low temperature in regions of high particle density (high Damköhler numbers). In those regions the conversion rate was in the kinetically-controlled regime, in which turbulence cannot affect the reaction rate.

4.2 Future work

Despite the fact that the results showed marginal effect of turbulence on the conversion rate in the investigated industrial-scale boiler, it would be interesting to examine other industrial systems. Based on theoretical predictions presented in paper II, many facilities with much higher sensitivity to the effect of particle clustering exist. This includes gasification reactors, combustion systems in which conversion undergoes in oxy-fuel atmospheres or Chemical Looping Combustion reactors, in which minerals serve as oxygen carriers. The reasons the effect of turbulence is foreseen to be stronger in those systems are e.g. higher temperature (i.e. reaction in the diffusion-controlled regime), higher Damköhler numbers or higher equivalence ratios.

Many future improvements can be suggested for a resolved particle model. As clearly seen by comparing with recent publications on the resolved char particle conversion, the model implemented into the Pencil Code is not as advanced as other similar models. Even though the model was developed with efficiency in mind, some simplifications should be removed in order to fully benefit of the model capabilities to predict unsteady phenomena. First of all, the assumption of the constant surface temperature should be replaced by a boundary condition that accounts for key heat transfer mechanisms. In addition, many transient processes cannot be

investigated with the semi-global reaction mechanism implemented at the moment. Therefore, a more detailed mechanism both for heterogeneous and homogeneous reactions should be considered. This would also entail re-implementation of the species boundary conditions as at the current stage of development a simple algorithm is used which assumes that the only reactive species at the particle surface are O_2 and CO_2 . The last modification, which is crucial to perform transient simulations, is implementation of realistic initial conditions. Apart from the above mentioned aspects, further extensions of the model would be required to gain a deeper insight into the conversion process. For example, following current trends in the literature, it would be interesting to expand the code capability to particle ensembles or to employ a continuum porous medium approach to account for intra-particle phenomena. This would, however, require a significant code expansion. Given the additional challenges of dealing with a compressible flow solver, a question should be raised whether such a major code expansion is reasonable.

Bibliography

- [1] E. Karchniwy, N. E. L. Haugen, A. Klimanek, Ø. Langørgen, S. Sładek, The effect of turbulence on mass transfer in solid fuel combustion: RANS model, *Combustion and Flame* 227 (2021) 65–78. doi:[10.1016/J.COMBUSTFLAME.2020.12.040](https://doi.org/10.1016/J.COMBUSTFLAME.2020.12.040).
- [2] E. Karchniwy, A. Klimanek, N. E. L. Haugen, The effect of turbulence on mass transfer rates between inertial polydisperse particles and fluid, *Journal of Fluid Mechanics* 874 (2019) 1147–1168. doi:[10.1017/JFM.2019.493](https://doi.org/10.1017/JFM.2019.493).
- [3] C. Hasse, P. Debiagi, X. Wen, K. Hildebrandt, M. Vascellari, T. Faravelli, Advanced modeling approaches for CFD simulations of coal combustion and gasification, *Progress in Energy and Combustion Science* 86 (2021) 100938. doi:<https://doi.org/10.1016/j.pecs.2021.100938>.
- [4] S. Niksa, 2 - Fuel quality, thermophysical properties, and transport coefficients, in: S. Niksa (Ed.), *Process Chemistry of Coal Utilization*, Woodhead Publishing Series in Energy, Woodhead Publishing, 2020, pp. 23–52. doi:<https://doi.org/10.1016/B978-0-12-818713-5.00002-2>.
- [5] [Statistical review of world energy, 69th edition](#), Tech. rep., British Petroleum Co, London (2020).
URL <https://www.bp.com/content/dam/bp/business-sites/en/global/corporate/pdfs/energy-economics/statistical-review/bp-stats-review-2020-full-report.pdf>

- [6] **Renewables 2020**, Tech. rep., International Energy Agency, Paris (2020).
URL <https://www.iea.org/reports/renewables-2020>
- [7] **World energy outlook 2020**, Tech. rep., International Energy Agency, Paris (2020).
URL <https://www.iea.org/reports/world-energy-outlook-2020>
- [8] H. Ritchie, M. Roser, **Energy mix**, Tech. rep. (2020).
URL <https://ourworldindata.org/energy>
- [9] **Statistical review of world energy, 70th edition**, Tech. rep., British Petroleum Co, London (2021).
URL <https://www.bp.com/content/dam/bp/business-sites/en/global/corporate/pdfs/energy-economics/statistical-review/bp-stats-review-2021-full-report.pdf>
- [10] **World energy resources 2016**, Tech. rep., World Energy Council (2016).
URL <https://www.worldenergy.org/wp-content/uploads/2016/10/World-Energy-Resources-Full-report-2016.10.03.pdf>
- [11] **Electricity market report - july 2021**, Tech. rep., International Energy Agency, Paris (2021).
URL <https://www.iea.org/reports/electricity-market-report-july-2021>
- [12] P. A. Morgan, S. D. Robertson, J. F. Unsworth, Combustion studies by thermogravimetric analysis. 1. Coal oxidation, *Fuel* 65 (11) (1986) 1546–1551. doi:10.1016/0016-2361(86)90331-5.
- [13] S. S. Idris, N. A. Rahman, K. Ismail, Combustion characteristics of Malaysian oil palm biomass, sub-bituminous coal and their respective blends via thermogravimetric analysis (TGA), *Bioresource Technology* 123 (2012) 581–591. doi:10.1016/j.biortech.2012.07.065.
- [14] S. Ouyang, H. Yeasmin, J. Mathews, A pressurized drop-tube furnace for coal reactivity studies, *Review of Scientific Instruments* 69 (8) (1998) 3036–3041. doi:10.1063/1.1149052.
- [15] J. Riaza, R. Khatami, Y. A. Levendis, L. Álvarez, M. V. Gil, C. Pevida, F. Rubiera, J. J. Pis, Single particle ignition and combustion of anthracite, semi-anthracite and bituminous coals in air and simulated oxy-fuel

- conditions, *Combustion and Flame* 161 (4) (2014) 1096–1108. doi:
[10.1016/j.combustflame.2013.10.004](https://doi.org/10.1016/j.combustflame.2013.10.004).
- [16] X. Bai, G. Lu, T. Bennet, A. Sarroza, C. Eastwick, H. Liu, Y. Yan, Combustion behavior profiling of single pulverized coal particles in a drop tube furnace through high-speed imaging and image analysis, *Experimental Thermal and Fluid Science* 85 (2017) 322–330. doi:[10.1016/j.expthermflusci.2017.03.018](https://doi.org/10.1016/j.expthermflusci.2017.03.018).
- [17] S. Subramaniam, M. Mehrabadi, J. Horwitz, Developing improved Lagrangian point particle models of gas-solid flow from particle-resolved direct numerical simulation, Center for Turbulence Research Proceedings of the Summer Program (January) (2014) 5–14. doi:[10.13140/RG.2.1.1814.2326](https://doi.org/10.13140/RG.2.1.1814.2326).
- [18] J. G. M. Kuerten, Point-Particle DNS and LES of Particle-Laden Turbulent flow - a state-of-the-art review, *Flow, Turbul. Combust.* 97 (3) (2016) 689–713. doi:[10.1007/s10494-016-9765-y](https://doi.org/10.1007/s10494-016-9765-y).
- [19] P. Costa, L. Brandt, F. Picano, Interface-resolved simulations of small inertial particles in turbulent channel flow, *Journal of Fluid Mechanics* 883 (2020) A54. doi:[10.1017/jfm.2019.918](https://doi.org/10.1017/jfm.2019.918).
- [20] F. Picano, W. P. Breugem, L. Brandt, Turbulent channel flow of dense suspensions of neutrally-buoyant spheres, *Journal of Fluid Mechanics* 764 (2015) 463–487. doi:[10.1017/jfm.2014.704](https://doi.org/10.1017/jfm.2014.704).
- [21] J. Lu, S. Das, E. A. Peters, J. A. Kuipers, Direct numerical simulation of fluid flow and mass transfer in dense fluid-particle systems with surface reactions, *Chemical Engineering Science* 176 (2018) 1–18. doi:
[10.1016/j.ces.2017.10.018](https://doi.org/10.1016/j.ces.2017.10.018).
- [22] J. Lu, E. A. Peters, J. A. Kuipers, Direct numerical simulation of fluid flow and dependently coupled heat and mass transfer in fluid-particle systems, *Chemical Engineering Science* 204 (2019) 203–219. doi:[10.1016/j.ces.2019.02.043](https://doi.org/10.1016/j.ces.2019.02.043).
- [23] A. Abdelsamie, G. Fru, T. Oster, F. Dietzsch, G. Janiga, D. Thévenin, Towards direct numerical simulations of low-Mach number turbulent reacting and two-phase flows using immersed boundaries, *Computers and Fluids* 131 (2016) 123–141. doi:[10.1016/j.compfluid.2016.03.017](https://doi.org/10.1016/j.compfluid.2016.03.017).
- [24] N. G. Deen, E. Peters, J. T. Padding, J. Kuipers, Review of direct numerical simulation of fluid–particle mass, momentum and heat transfer

- in dense gas–solid flows, *Chem. Eng. Sci.* 116 (2014) 710–724. doi:
[10.1016/j.ces.2014.05.039](https://doi.org/10.1016/j.ces.2014.05.039).
- [25] S. Tenneti, S. Subramaniam, Particle-Resolved Direct Numerical Simulation for Gas-Solid Flow Model Development, *Annu. Rev. Fluid Mech.* 46 (1) (2014) 199–230. doi:[10.1146/annurev-fluid-010313-141344](https://doi.org/10.1146/annurev-fluid-010313-141344).
- [26] P. R. Solomon, D. G. Hamblen, R. M. Carangelo, M. A. Serio, G. V. Deshpande, General model of coal devolatilization, *Energy and Fuels* 2 (4) (2002) 405–422. doi:[10.1021/EF00010A006](https://doi.org/10.1021/EF00010A006).
- [27] S. Niksa, A. R. Kerstein, FLASHCHAIN Theory for Rapid Coal Devolatilization Kinetics. 1. Formulation, *Energy and Fuels* 5 (5) (1991) 647–665. doi:[10.1021/ef00029a006](https://doi.org/10.1021/ef00029a006).
- [28] D. M. Grant, R. J. Pugmire, T. H. Fletcher, A. R. Kerstein, Chemical Model of Coal Devolatilization Using Percolation Lattice Statistics, *Energy and Fuels* 3 (2) (1989) 175–186. doi:[10.1021/ef00014a011](https://doi.org/10.1021/ef00014a011).
- [29] S. Niksa, Predicting the rapid devolatilization of diverse forms of biomass with bio-flashchain, *Proceedings of the Combustion Institute* 28 (2) (2000) 2727–2733. doi:[https://doi.org/10.1016/S0082-0784\(00\)80693-1](https://doi.org/10.1016/S0082-0784(00)80693-1).
- [30] A. D. Lewis, T. H. Fletcher, Prediction of sawdust pyrolysis yields from a flat-flame burner using the CPD model, *Energy and Fuels* 27 (2) (2013) 942–953. doi:[10.1021/ef3018783](https://doi.org/10.1021/ef3018783).
- [31] S. Badzioch, P. G. Hawksley, Kinetics of Thermal Decomposition of Pulverized Coal Particles, *Industrial and Engineering Chemistry Process Design and Development* 9 (4) (1970) 521–530. doi:[10.1021/i260036a005](https://doi.org/10.1021/i260036a005).
- [32] H. Kobayashi, J. B. Howard, A. F. Sarofim, Coal devolatilization at high temperatures, *Symposium (International) on Combustion* 16 (1) (1977) 411–425. doi:[10.1016/S0082-0784\(77\)80341-X](https://doi.org/10.1016/S0082-0784(77)80341-X).
- [33] D. B. Anthony, J. B. Howard, H. C. Hottel, H. P. Meissner, Rapid devolatilization of pulverized coal, *Symposium (International) on Combustion* 15 (1) (1975) 1303–1317. doi:[10.1016/S0082-0784\(75\)80392-4](https://doi.org/10.1016/S0082-0784(75)80392-4).
- [34] D. B. Anthony, J. B. Howard, Coal devolatilization and hydrogastification, *AIChE Journal* 22 (4) (1976) 625–656. doi:[10.1002/AIC.690220403](https://doi.org/10.1002/AIC.690220403).

- [35] M. Vascellari, R. Arora, M. Pollack, C. Hasse, Simulation of entrained flow gasification with advanced coal conversion submodels. Part 1: Pyrolysis, *Fuel* 113 (2013) 654–669. doi:[10.1016/j.fuel.2013.06.014](https://doi.org/10.1016/j.fuel.2013.06.014).
- [36] M. Vascellari, D. G. Roberts, S. S. Hla, D. J. Harris, C. Hasse, From laboratory-scale experiments to industrial-scale CFD simulations of entrained flow coal gasification, *Fuel* 152 (2015) 58–73. doi:[10.1016/j.fuel.2015.01.038](https://doi.org/10.1016/j.fuel.2015.01.038).
- [37] M. Saito, M. Sato, H. Murata, M. Sadakata, Combustion behaviour of pulverized coal particles in a high temperature and high oxygen concentration atmosphere, *Fuel* 70 (6) (1991) 709–712. doi:[10.1016/0016-2361\(91\)90066-J](https://doi.org/10.1016/0016-2361(91)90066-J).
- [38] G. L. Tufano, O. T. Stein, A. Kronenburg, G. Gentile, A. Stagni, A. Frassoldati, T. Faravelli, A. M. Kempf, M. Vascellari, C. Hasse, Fully-resolved simulations of coal particle combustion using a detailed multi-step approach for heterogeneous kinetics, *Fuel* 240 (2019) 75–83. doi:[10.1016/j.fuel.2018.11.139](https://doi.org/10.1016/j.fuel.2018.11.139).
- [39] S. C. Hill, L. D. Smoot, Modeling of nitrogen oxides formation and destruction in combustion systems (aug 2000). doi:[10.1016/S0360-1285\(00\)00011-3](https://doi.org/10.1016/S0360-1285(00)00011-3).
- [40] A. Molina, J. J. Murphy, F. Winter, B. S. Haynes, L. G. Blevins, C. R. Shaddix, Pathways for conversion of char nitrogen to nitric oxide during pulverized coal combustion, *Combustion and Flame* 156 (3) (2009) 574–587. doi:[10.1016/j.combustflame.2008.11.012](https://doi.org/10.1016/j.combustflame.2008.11.012).
- [41] P. Debiagi, C. Yildiz, J. Ströhle, B. Epple, T. Faravelli, C. Hasse, Systematic evaluation and kinetic modeling of low heating rate sulfur release in various atmospheres, *Fuel* 289 (2021) 119739. doi:[10.1016/j.fuel.2020.119739](https://doi.org/10.1016/j.fuel.2020.119739).
- [42] E. S. Hecht, C. R. Shaddix, J. A. S. Lighty, Analysis of the errors associated with typical pulverized coal char combustion modeling assumptions for oxy-fuel combustion, *Combustion and Flame* 160 (8) (2013) 1499–1509. doi:[10.1016/j.combustflame.2013.02.015](https://doi.org/10.1016/j.combustflame.2013.02.015).
- [43] K. Smith, L. Smoot, T. H. Fletcher, R. J. Pugmire, *The Structure and Reaction Processes of Coal*, Springer, Boston, MA, 1994.

- [44] R. H. Hurt, J. M. Calo, Semi-global intrinsic kinetics for char combustion modeling, *Combustion and Flame* 125 (3) (2001) 1138–1149. doi:[10.1016/S0010-2180\(01\)00234-6](https://doi.org/10.1016/S0010-2180(01)00234-6).
- [45] R. H. Essenhigh, Rate Equations for the Carbon-Oxygen Reaction: An Evaluation of the Langmuir Adsorption Isotherm at Atmospheric Pressure, *Energy and Fuels* 5 (1) (1991) 41–46. doi:[10.1021/ef00025a005](https://doi.org/10.1021/ef00025a005).
- [46] J. Hong, W. C. Hecker, T. H. Fletcher, Modeling high-pressure char oxidation using Langmuir kinetics with an effectiveness factor, *Proceedings of the Combustion Institute* 28 (2) (2000) 2215–2223. doi:[10.1016/S0082-0784\(00\)80631-1](https://doi.org/10.1016/S0082-0784(00)80631-1).
- [47] Z. Huang, J. Zhang, Y. Zhao, H. Zhang, G. Yue, T. Suda, M. Narukawa, Kinetic studies of char gasification by steam and CO₂ in the presence of H₂ and CO, in: *Fuel Processing Technology*, Vol. 91, Elsevier, 2010, pp. 843–847. doi:[10.1016/j.fuproc.2009.12.020](https://doi.org/10.1016/j.fuproc.2009.12.020).
- [48] C. Heinze, E. Langner, J. May, B. Epple, Determination of a complete conversion model for gasification of lignite char, *Applied Sciences (Switzerland)* 10 (6) (2020) 1916. doi:[10.3390/app10061916](https://doi.org/10.3390/app10061916).
- [49] M. B. Tilghman, N. E. L. Haugen, R. E. Mitchell, Comprehensive Char Particle Gasification Model Adequate for Entrained-Flow and Fluidized-Bed Gasifiers, *Energy and Fuels* 31 (3) (2017) 2164–2174. doi:[10.1021/acs.energyfuels.6b02148](https://doi.org/10.1021/acs.energyfuels.6b02148).
- [50] Y. Numazawa, Y. Saito, Y. Matsushita, H. Aoki, Large-scale simulation of gasification reaction with mass transfer for metallurgical coke: Model development, *Fuel* 266 (2020) 117080. doi:[10.1016/j.fuel.2020.117080](https://doi.org/10.1016/j.fuel.2020.117080).
- [51] C. Georgakis, C. W. Chang, J. Szekely, A changing grain size model for gas—solid reactions, *Chemical Engineering Science* 34 (8) (1979) 1072–1075. doi:[https://doi.org/10.1016/0009-2509\(79\)80012-3](https://doi.org/10.1016/0009-2509(79)80012-3).
- [52] S. K. Bhatia, D. D. Perlmutter, A random pore model for fluid-solid reactions: I. Isothermal, kinetic control, *AIChE Journal* 26 (3) (1980) 379–386. doi:<https://doi.org/10.1002/aic.690260308>.
- [53] S. K. Bhatia, D. D. Perlmutter, A random pore model for fluid-solid reactions: II. Diffusion and transport effects, *AIChE Journal* 27 (2) (1981) 247–254. doi:<https://doi.org/10.1002/aic.690270211>.

- [54] E. W. Thiele, Relation between Catalytic Activity and Size of Particle, *Industrial & Engineering Chemistry* 31 (7) (1939) 916–920. doi:[10.1021/ie50355a027](https://doi.org/10.1021/ie50355a027).
- [55] N. E. L. Haugen, M. B. Tilghman, R. E. Mitchell, The conversion mode of a porous carbon particle during oxidation and gasification, *Combustion and Flame* 161 (2) (2014) 612–619. doi:<https://doi.org/10.1016/j.combustflame.2013.09.012>.
- [56] H. S. Shim, R. H. Hurt, Thermal annealing of chars from diverse organic precursors under combustion-like conditions, *Energy and Fuels* 14 (2) (2000) 340–348. doi:[10.1021/ef9901286](https://doi.org/10.1021/ef9901286).
- [57] B. Feng, A. Jensen, S. K. Bhatia, K. Dam-Johansen, Activation energy distribution of thermal annealing of a bituminous coal, *Energy and Fuels* 17 (2) (2003) 399–404. doi:[10.1021/ef020108v](https://doi.org/10.1021/ef020108v).
- [58] R. H. Hurt, Structure, properties, and reactivity of solid fuels, *Symposium (International) on Combustion* 27 (2) (1998) 2887–2904. doi:[https://doi.org/10.1016/S0082-0784\(98\)80148-3](https://doi.org/10.1016/S0082-0784(98)80148-3).
- [59] N. V. Russell, J. R. Gibbins, C. K. Man, J. Williamson, Coal char thermal deactivation under pulverized fuel combustion conditions, *Energy and Fuels* 14 (4) (2000) 883–888. doi:[10.1021/ef990241w](https://doi.org/10.1021/ef990241w).
- [60] O. Senneca, P. Salatino, A semi-detailed kinetic model of char combustion with consideration of thermal annealing, *Proceedings of the Combustion Institute* 33 (2) (2011) 1763–1770. doi:[10.1016/j.proci.2010.08.011](https://doi.org/10.1016/j.proci.2010.08.011).
- [61] T. Kreitzberg, C. Bormann, S. Pielsticker, O. Hatzfeld, R. Kneer, Thermal deactivation of biogenic and fossil fuels: Experimental investigation and modeling approaches, in: *Energy Procedia*, Vol. 158, Elsevier, 2019, pp. 2025–2030. doi:[10.1016/j.egypro.2019.01.468](https://doi.org/10.1016/j.egypro.2019.01.468).
- [62] R. Hurt, J. K. Sun, M. Lunden, A Kinetic Model of Carbon Burnout in Pulverized Coal Combustion, *Combustion and Flame* 113 (1-2) (1998) 181–197. doi:[10.1016/S0010-2180\(97\)00240-X](https://doi.org/10.1016/S0010-2180(97)00240-X).
- [63] Y. Niu, C. R. Shaddix, A sophisticated model to predict ash inhibition during combustion of pulverized char particles, *Proceedings of the Combustion Institute* 35 (1) (2015) 561–569. doi:[10.1016/j.proci.2014.05.077](https://doi.org/10.1016/j.proci.2014.05.077).

- [64] S. Niksa, G. S. Liu, R. H. Hurt, Coal conversion submodels for design applications at elevated pressures. Part I. Devolatilization and char oxidation (jan 2003). [doi:10.1016/S0360-1285\(03\)00033-9](https://doi.org/10.1016/S0360-1285(03)00033-9).
- [65] G. S. Liu, S. Niksa, Coal conversion submodels for design applications at elevated pressures. Part II. Char gasification (jan 2004). [doi:10.1016/j.pecs.2004.08.001](https://doi.org/10.1016/j.pecs.2004.08.001).
- [66] D. Veynante, L. Vervisch, Turbulent combustion modeling (mar 2002). [doi:10.1016/S0360-1285\(01\)00017-X](https://doi.org/10.1016/S0360-1285(01)00017-X).
- [67] B. F. Magnussen, B. H. Hjertager, On mathematical modeling of turbulent combustion with special emphasis on soot formation and combustion, Symposium (International) on Combustion 16 (1) (1977) 719–729. [doi:10.1016/S0082-0784\(77\)80366-4](https://doi.org/10.1016/S0082-0784(77)80366-4).
- [68] B. Magnussen, On the structure of turbulence and a generalized eddy dissipation concept for chemical reaction in turbulent flow, American Institute of Aeronautics and Astronautics (AIAA), 1981. [doi:10.2514/6.1981-42](https://doi.org/10.2514/6.1981-42).
- [69] N. Peters, Laminar diffusion flamelet models in non-premixed turbulent combustion, Progress in Energy and Combustion Science 10 (3) (1984) 319–339. [doi:10.1016/0360-1285\(84\)90114-X](https://doi.org/10.1016/0360-1285(84)90114-X).
- [70] S. B. Pope, PDF methods for turbulent reactive flows (jan 1985). [doi:10.1016/0360-1285\(85\)90002-4](https://doi.org/10.1016/0360-1285(85)90002-4).
- [71] R. W. Bilger, Conditional moment closure for turbulent reacting flow, Physics of Fluids A 5 (2) (1992) 436–444. [doi:10.1063/1.858867](https://doi.org/10.1063/1.858867).
- [72] D. V. Flores, T. H. Fletcher, Use of two mixture fractions to treat coal combustion products in turbulent pulverized-coal flames, Combustion science and technology 150 (1) (2000) 1–26. [doi:10.1080/00102200008952115](https://doi.org/10.1080/00102200008952115).
- [73] M. Stöllinger, B. Naud, D. Roekaerts, N. Beishuizen, S. Heinz, PDF modeling and simulations of pulverized coal combustion - Part 2: Application, Combustion and Flame 160 (2) (2013) 396–410. [doi:10.1016/j.combustflame.2012.10.011](https://doi.org/10.1016/j.combustflame.2012.10.011).
- [74] X. Y. Zhao, D. C. Haworth, Transported PDF modeling of pulverized coal jet flames, Combustion and Flame 161 (7) (2014) 1866–1882. [doi:10.1016/j.combustflame.2013.12.024](https://doi.org/10.1016/j.combustflame.2013.12.024).

- [75] L. Zhao, M. J. Cleary, O. T. Stein, A. Kronenburg, A two-phase MMC-LES model for pyrolysing solid particles in a turbulent flame, *Combustion and Flame* 209 (2019) 322–336. doi:[10.1016/j.combustflame.2019.08.005](https://doi.org/10.1016/j.combustflame.2019.08.005).
- [76] J. Krüger, N. E. Haugen, D. Mitra, T. Løvås, The effect of turbulent clustering on particle reactivity, *Proceedings of the Combustion Institute* 36 (2) (2017) 2333–2340. doi:[10.1016/j.proci.2016.06.187](https://doi.org/10.1016/j.proci.2016.06.187).
- [77] N. E. L. Haugen, J. Krüger, D. Mitra, T. Løvås, The effect of turbulence on mass transfer rates of small inertial particles with surface reactions, *Journal of Fluid Mechanics* 836 (2018) 932–951. doi:[10.1017/JFM.2017.820](https://doi.org/10.1017/JFM.2017.820).
- [78] J. Bec, L. Biferale, M. Cencini, A. Lanotte, S. Musacchio, F. Toschi, Heavy particle concentration in turbulence at dissipative and inertial scales, *Physical Review Letters* 98 (8) (2007) 084502. arXiv:[0608045](https://arxiv.org/abs/0608045), doi:[10.1103/PhysRevLett.98.084502](https://doi.org/10.1103/PhysRevLett.98.084502).
- [79] E. Calzavarini, M. Kerscher, D. Lohse, F. Toschi, Dimensionality and morphology of particle and bubble clusters in turbulent flow, *Journal of Fluid Mechanics* 607 (2008) 13–24. doi:[10.1017/S0022112008001936](https://doi.org/10.1017/S0022112008001936).
- [80] E. W. Saw, R. A. Shaw, S. Ayyalasomayajula, P. Y. Chuang, Á. Gylfason, Inertial clustering of particles in high-reynolds-number turbulence, *Physical Review Letters* 100 (21) (2008) 214501. doi:[10.1103/PhysRevLett.100.214501](https://doi.org/10.1103/PhysRevLett.100.214501).
- [81] A. J. Petersen, L. Baker, F. Coletti, Experimental study of inertial particles clustering and settling in homogeneous turbulence, *Journal of Fluid Mechanics* 864 (2019) 925–970. doi:[10.1017/jfm.2019.31](https://doi.org/10.1017/jfm.2019.31).
- [82] L. Chen, S. Z. Yong, A. F. Ghoniem, Oxy-fuel combustion of pulverized coal: Characterization, fundamentals, stabilization and CFD modeling, *Progress in Energy and Combustion Science* 38 (2) (2012) 156–214. doi:[10.1016/j.pecs.2011.09.003](https://doi.org/10.1016/j.pecs.2011.09.003).
- [83] G. Sankar, D. S. Kumar, K. R. Balasubramanian, Computational modeling of pulverized coal fired boilers – A review on the current position, *Fuel* 236 (2019) 643–665. doi:[10.1016/j.fuel.2018.08.154](https://doi.org/10.1016/j.fuel.2018.08.154).
- [84] T. Poinso, D. Veynante, *Theoretical and Numerical Combustion*, R.T. Edwards Inc., 2005.

- [85] O. T. Stein, G. Olenik, A. Kronenburg, F. Cavallo Marincola, B. M. Franchetti, A. M. Kempf, M. Ghiani, M. Vascellari, C. Hasse, Towards comprehensive coal combustion modelling for les, in: *Flow, Turbulence and Combustion*, Vol. 90, Springer, 2013, pp. 859–884. doi:[10.1007/s10494-012-9423-y](https://doi.org/10.1007/s10494-012-9423-y).
- [86] B. M. Franchetti, F. Cavallo Marincola, S. Navarro-Martinez, A. M. Kempf, Large Eddy simulation of a pulverised coal jet flame, *Proceedings of the Combustion Institute* 34 (2) (2013) 2419–2426. doi:[10.1016/j.proci.2012.07.056](https://doi.org/10.1016/j.proci.2012.07.056).
- [87] M. Rabaçal, B. M. Franchetti, F. C. Marincola, F. Proch, M. Costa, C. Hasse, A. M. Kempf, Large Eddy Simulation of coal combustion in a large-scale laboratory furnace, *Proceedings of the Combustion Institute* 35 (3) (2015) 3609–3617. doi:[10.1016/j.proci.2014.06.023](https://doi.org/10.1016/j.proci.2014.06.023).
- [88] M. Muto, H. Watanabe, R. Kurose, Large eddy simulation of pulverized coal combustion in multi-burner system—effect of in-furnace blending method on NO emission, *Advanced Powder Technology* 30 (12) (2019) 3153–3162. doi:[10.1016/j.appt.2019.09.024](https://doi.org/10.1016/j.appt.2019.09.024).
- [89] X. Wen, H. Nicolai, H. Schneider, L. Cai, J. Janicka, H. Pitsch, C. Hasse, Flamelet les of a swirl-stabilized multi-stream pulverized coal burner in air and oxy-fuel atmospheres with pollutant formation, in: *Proceedings of the Combustion Institute*, Vol. 38, Elsevier, 2021, pp. 4141–4149. doi:[10.1016/j.proci.2020.05.061](https://doi.org/10.1016/j.proci.2020.05.061).
- [90] N. Abani, A. F. Ghoniem, Large eddy simulations of coal gasification in an entrained flow gasifier, *Fuel* 104 (2013) 664–680. doi:[10.1016/j.fuel.2012.06.006](https://doi.org/10.1016/j.fuel.2012.06.006).
- [91] S. Gupta, S. Choudhary, S. Kumar, S. De, Large eddy simulation of biomass gasification in a bubbling fluidized bed based on the multiphase particle-in-cell method, *Renewable Energy* 163 (2021) 1455–1466. doi:[10.1016/j.renene.2020.07.127](https://doi.org/10.1016/j.renene.2020.07.127).
- [92] W. P. Adamczyk, B. Isaac, J. Parra-Alvarez, S. T. Smith, D. Harris, J. N. Thornock, M. Zhou, P. J. Smith, R. Žmuda, Application of LES-CFD for predicting pulverized-coal working conditions after installation of NOx control system, *Energy* 160 (2018) 693–709. doi:[10.1016/j.energy.2018.07.031](https://doi.org/10.1016/j.energy.2018.07.031).

- [93] K. Luo, H. Wang, J. Fan, F. Yi, Direct Numerical Simulation of Pulverized Coal Combustion in a Hot Vitiated Co-flow, *Energy & Fuels* 26 (10) (2012) 6128–6136. doi:[10.1021/ef301253y](https://doi.org/10.1021/ef301253y).
- [94] Y. Bai, K. Luo, K. Qiu, J. Fan, Numerical investigation of two-phase flame structures in a simplified coal jet flame, *Fuel* 182 (2016) 944–957. doi:[10.1016/J.FUEL.2016.05.086](https://doi.org/10.1016/J.FUEL.2016.05.086).
- [95] K. Luo, Y. Bai, T. Jin, K. Qiu, J. Fan, Direct Numerical Simulation Study on the Stabilization Mechanism of a Turbulent Lifted Pulverized Coal Jet Flame in a Heated Coflow, *Energy & Fuels* 31 (8) (2017) 8742–8757. doi:[10.1021/acs.energyfuels.7b01342](https://doi.org/10.1021/acs.energyfuels.7b01342).
- [96] T. Hara, M. Muto, T. Kitano, R. Kurose, S. Komori, Direct numerical simulation of a pulverized coal jet flame employing a global volatile matter reaction scheme based on detailed reaction mechanism, *Combust. Flame* 162 (12) (2015) 4391–4407. doi:[10.1016/j.combustflame.2015.07.027](https://doi.org/10.1016/j.combustflame.2015.07.027).
- [97] M. Muto, K. Tanno, R. Kurose, A DNS study on effect of coal particle swelling due to devolatilization on pulverized coal jet flame, *Fuel* 184 (2016) 749–752. doi:[10.1016/j.fuel.2016.07.070](https://doi.org/10.1016/j.fuel.2016.07.070).
- [98] T. Brosh, N. Chakraborty, Effects of Equivalence Ratio and Turbulent Velocity Fluctuation on Early Stages of Pulverized Coal Combustion Following Localized Ignition: A Direct Numerical Simulation Analysis, *Energy & Fuels* 28 (9) (2014) 6077–6088. doi:[10.1021/ef501171n](https://doi.org/10.1021/ef501171n).
- [99] T. Brosh, D. Patel, D. Wacks, N. Chakraborty, Numerical investigation of localised forced ignition of pulverised coal particle-laden mixtures: A Direct Numerical Simulation (DNS) analysis, *Fuel* 145 (2015) 50–62. doi:[10.1016/j.fuel.2014.12.006](https://doi.org/10.1016/j.fuel.2014.12.006).
- [100] M. Muto, K. Yuasa, R. Kurose, Numerical simulation of ignition in pulverized coal combustion with detailed chemical reaction mechanism, *Fuel* 190 (2017) 136–144. doi:[10.1016/j.fuel.2016.11.029](https://doi.org/10.1016/j.fuel.2016.11.029).
- [101] M. Rieth, A. M. Kempf, A. Kronenburg, O. T. Stein, Carrier-phase DNS of pulverized coal particle ignition and volatile burning in a turbulent mixing layer, *Fuel* 212 (2018) 364–374. doi:[10.1016/j.fuel.2017.09.096](https://doi.org/10.1016/j.fuel.2017.09.096).
- [102] X. Wen, A. Shamooni, O. T. Stein, L. Cai, A. Kronenburg, H. Pitsch, A. M. Kempf, C. Hasse, Detailed analysis of early-stage NO_x formation

- in turbulent pulverized coal combustion with fuel-bound nitrogen, *Proceedings of the Combustion Institute* 38 (3) (2021) 4111–4119. doi:[10.1016/j.proci.2020.06.317](https://doi.org/10.1016/j.proci.2020.06.317).
- [103] A. Shamooni, P. Debiagi, B. Wang, T. D. Luu, O. T. Stein, A. Kronenburg, G. Bagheri, A. Stagni, A. Frassoldati, T. Faravelli, A. M. Kempf, X. Wen, C. Hasse, Carrier-phase DNS of detailed NO_x formation in early-stage pulverized coal combustion with fuel-bound nitrogen, *Fuel* 291 (2021) 119998. doi:[10.1016/j.fuel.2020.119998](https://doi.org/10.1016/j.fuel.2020.119998).
- [104] K. Wan, L. Vervisch, J. Xia, P. Domingo, Z. Wang, Y. Liu, K. Cen, Alkali metal emissions in an early-stage pulverized-coal flame: DNS analysis of reacting layers and chemistry tabulation, *Proceedings of the Combustion Institute* 37 (3) (2019) 2791–2799. doi:[10.1016/j.proci.2018.06.119](https://doi.org/10.1016/j.proci.2018.06.119).
- [105] J. Krüger, N. E. L. Haugen, T. Løvås, Correlation effects between turbulence and the conversion rate of pulverized char particles, *Combustion and Flame* 185 (2017) 160–172. doi:[10.1016/j.combustflame.2017.07.008](https://doi.org/10.1016/j.combustflame.2017.07.008).
- [106] A. W. Vreman, Particle-resolved direct numerical simulation of homogeneous isotropic turbulence modified by small fixed spheres, *Journal of Fluid Mechanics* 796 (2016) 40–85. doi:[10.1017/jfm.2016.228](https://doi.org/10.1017/jfm.2016.228).
- [107] J. Lee, A. Tomboulides, S. Orszag, R. Yetter, F. Dryer, A transient two-dimensional chemically reactive flow model: Fuel particle combustion in a nonquiescent environment, *Symposium (International) on Combustion* 26 (2) (1996) 3059–3065. doi:[10.1016/S0082-0784\(96\)80149-4](https://doi.org/10.1016/S0082-0784(96)80149-4).
- [108] J. C. Lee, R. A. Yetter, F. L. Dryer, Numerical simulation of laser ignition of an isolated carbon particle in quiescent environment, *Combustion and Flame* 105 (4) (1996) 591–599. doi:[10.1016/0010-2180\(96\)00221-0](https://doi.org/10.1016/0010-2180(96)00221-0).
- [109] R. E. Mitchell, L. Ma, B. J. Kim, On the burning behavior of pulverized coal chars, *Combustion and Flame* 151 (3) (2007) 426–436. doi:[10.1016/j.combustflame.2007.07.014](https://doi.org/10.1016/j.combustflame.2007.07.014).
- [110] R. Stauch, U. Maas, Transient detailed numerical simulation of the combustion of carbon particles, *International Journal of Heat and Mass Transfer* 52 (19-20) (2009) 4584–4591. doi:[10.1016/j.ijheatmasstransfer.2009.02.047](https://doi.org/10.1016/j.ijheatmasstransfer.2009.02.047).

- [111] E. S. Hecht, C. R. Shaddix, M. Geier, A. Molina, B. S. Haynes, Effect of CO₂ and steam gasification reactions on the oxy-combustion of pulverized coal char, *Combustion and Flame* 159 (11) (2012) 3437–3447. doi:10.1016/j.combustflame.2012.06.009.
- [112] J. McConnell, B. Goshayeshi, J. C. Sutherland, An evaluation of the efficacy of various coal combustion models for predicting char burnout, *Fuel* 201 (2017) 53–64. doi:10.1016/j.fuel.2016.11.052.
- [113] R. Schwarz, S. DeYoung, H. Spliethoff, Numerical simulation of gasification with a one-dimensional particle submodel for char structure evolution, *Fuel* 293 (2021) 120492. doi:10.1016/j.fuel.2021.120492.
- [114] F. J. Higuera, Combustion of a coal char particle in a stream of dry gas, *Combustion and Flame* 152 (1-2) (2008) 230–244. doi:10.1016/j.combustflame.2007.06.001.
- [115] M. Kestel, P. Nikrityuk, B. Meyer, Numerical study of partial oxidation of a single coal particle in a stream of air, in: 2010 14th International Heat Transfer Conference, IHTC 14, Vol. 3, American Society of Mechanical Engineers Digital Collection, 2010, pp. 33–42. doi:10.1115/IHTC14-22263.
- [116] M. Kestel, P. Nikrityuk, O. Hennig, C. Hasse, Numerical study of the partial oxidation of a coal particle in steam and dry air atmospheres, in: *IMA Journal of Applied Mathematics (Institute of Mathematics and Its Applications)*, Vol. 77, Oxford University Press, 2012, pp. 32–46. doi:10.1093/imamat/hxr071.
- [117] Z. Zhang, Z. Zhao, F. Wu, C. Luo, X. Li, Y. Chen, B. Lu, L. Zhang, C. Zheng, Reaction behaviors of a single coal char particle affected by oxygen and steam under oxy-fuel combustion, *Fuel* 291 (2021) 120229. doi:10.1016/j.fuel.2021.120229.
- [118] P. A. Nikrityuk, M. Gräbner, M. Kestel, B. Meyer, Numerical study of the influence of heterogeneous kinetics on the carbon consumption by oxidation of a single coal particle, *Fuel* 114 (2013) 88–98. doi:10.1016/j.fuel.2012.10.037.
- [119] A. Richter, P. A. Nikrityuk, M. Kestel, Numerical Investigation of a Chemically Reacting Carbon Particle Moving in a Hot O₂/CO₂ Atmosphere, *Industrial Engineering Chemistry Research* 52 (16) (2013) 5815–5824. doi:10.1021/ie302770j.

- [120] D. Safronov, M. Kestel, P. Nikrityuk, B. Meyer, Particle resolved simulations of carbon oxidation in a laminar flow, *Canadian Journal of Chemical Engineering* 92 (10) (2014) 1669–1686. doi:[10.1002/cjce.22017](https://doi.org/10.1002/cjce.22017).
- [121] A. Richter, M. Kestel, P. A. Nikrityuk, Pore-Resolved Simulation of Char Particle Combustion/Gasification, *Gasification Processes: Modeling and Simulation* 9783527335503 (2014) 243–270. doi:[10.1002/9783527673186.CH9](https://doi.org/10.1002/9783527673186.CH9).
- [122] A. Richter, P. A. Nikrityuk, B. Meyer, Three-dimensional calculation of a chemically reacting porous particle moving in a hot O₂/CO₂ atmosphere, *International Journal of Heat and Mass Transfer* 83 (2015) 244–258. doi:[10.1016/j.ijheatmasstransfer.2014.11.090](https://doi.org/10.1016/j.ijheatmasstransfer.2014.11.090).
- [123] Z. Xue, Q. Guo, Y. Gong, J. Xu, G. Yu, Numerical study of a reacting single coal char particle with different pore structures moving in a hot O₂/CO₂ atmosphere, *Fuel* 206 (2017) 381–389. doi:[10.1016/j.fuel.2017.06.035](https://doi.org/10.1016/j.fuel.2017.06.035).
- [124] Z. Xue, Y. Gong, Q. Guo, Y. Wang, G. Yu, Conversion characteristics of a single coal char particle with high porosity moving in a hot O₂/CO₂ atmosphere, *Fuel* 256 (2019) 115967. doi:[10.1016/j.fuel.2019.115967](https://doi.org/10.1016/j.fuel.2019.115967).
- [125] A. Richter, M. Vascellari, P. A. Nikrityuk, C. Hasse, Detailed analysis of reacting particles in an entrained-flow gasifier, *Fuel Processing Technology* 144 (2016) 95–108. doi:[10.1016/j.fuproc.2015.12.014](https://doi.org/10.1016/j.fuproc.2015.12.014).
- [126] S. Schulze, P. Nikrityuk, F. Compant, A. Richter, B. Meyer, Particle-resolved numerical study of char conversion processes in packed beds, *Fuel* 207 (2017) 655–662. doi:[10.1016/j.fuel.2017.05.071](https://doi.org/10.1016/j.fuel.2017.05.071).
- [127] S. Schulze, P. Nikrityuk, Z. Abosteif, S. Guhl, A. Richter, B. Meyer, Heat and mass transfer within thermogravimetric analyser: From simulation to improved estimation of kinetic data for char gasification, *Fuel* 187 (2017) 338–348. doi:[10.1016/j.fuel.2016.09.048](https://doi.org/10.1016/j.fuel.2016.09.048).
- [128] M. Vascellari, H. Xu, C. Hasse, Flamelet modeling of coal particle ignition, *Proceedings of the Combustion Institute* 34 (2) (2013) 2445–2452. doi:[10.1016/j.proci.2012.06.152](https://doi.org/10.1016/j.proci.2012.06.152).
- [129] M. Vascellari, G. L. Tufano, O. T. Stein, A. Kronenburg, A. M. Kempf, A. Scholtissek, C. Hasse, A flamelet/progress variable approach for mod-

- eling coal particle ignition, *Fuel* 201 (2017) 29–38. doi:[10.1016/j.fuel.2016.09.005](https://doi.org/10.1016/j.fuel.2016.09.005).
- [130] G. L. Tufano, O. T. Stein, A. Kronenburg, A. Frassoldati, T. Faravelli, L. Deng, A. M. Kempf, M. Vascellari, C. Hasse, Resolved flow simulation of pulverized coal particle devolatilization and ignition in air- and O₂/CO₂-atmospheres, *Fuel* 186 (2016) 285–292. doi:[10.1016/j.fuel.2016.08.073](https://doi.org/10.1016/j.fuel.2016.08.073).
- [131] G. L. Tufano, O. T. Stein, B. Wang, A. Kronenburg, M. Rieth, A. M. Kempf, Coal particle volatile combustion and flame interaction. Part I: Characterization of transient and group effects, *Fuel* 229 (2018) 262–269. doi:[10.1016/j.fuel.2018.02.105](https://doi.org/10.1016/j.fuel.2018.02.105).
- [132] G. L. Tufano, O. T. Stein, B. Wang, A. Kronenburg, M. Rieth, A. M. Kempf, Coal particle volatile combustion and flame interaction. Part II: Effects of particle Reynolds number and turbulence, *Fuel* 234 (2018) 723–731. doi:[10.1016/j.fuel.2018.07.054](https://doi.org/10.1016/j.fuel.2018.07.054).
- [133] Q. Xiong, S. C. Kong, High-Resolution Particle-Scale Simulation of Biomass Pyrolysis, *ACS Sustainable Chemistry and Engineering* 4 (10) (2016) 5456–5461. doi:[10.1021/acssuschemeng.6b01020](https://doi.org/10.1021/acssuschemeng.6b01020).
- [134] K. Luo, C. Mao, J. Fan, Z. Zhuang, N. Haugen, Fully resolved simulations of single char particle combustion using a ghost-cell immersed boundary method, *AIChE Journal* 64 (7) (2018) 2851–2863. doi:[10.1002/aic.16136](https://doi.org/10.1002/aic.16136).
- [135] H. Zhang, K. Luo, N. E. L. Haugen, C. Mao, J. Fan, Drag force for a burning particle, *Combustion and Flame* 217 (2020) 188–199. doi:[10.1016/j.combustflame.2020.02.016](https://doi.org/10.1016/j.combustflame.2020.02.016).
- [136] A. M. Beckmann, J. Bibrzycki, M. Mancini, A. Szłęk, R. Weber, Mathematical modeling of reactants' transport and chemistry during oxidation of a millimeter-sized coal-char particle in a hot air stream, *Combustion and Flame* 180 (2017) 2–9. doi:[10.1016/j.combustflame.2017.02.026](https://doi.org/10.1016/j.combustflame.2017.02.026).
- [137] F. Dierich, A. Richter, P. Nikrityuk, A fixed-grid model to track the interface and porosity of a chemically reacting moving char particle, *Chemical Engineering Science* 175 (2018) 296–305. doi:[10.1016/j.ces.2017.09.055](https://doi.org/10.1016/j.ces.2017.09.055).

- [138] K. Wittig, P. A. Nikrityuk, S. Schulze, A. Richter, Three-dimensional modeling of porosity development during the gasification of a char particle, *AIChE Journal* 63 (5) (2017) 1638–1647. doi:10.1002/aic.15526.
- [139] G. H. Fong, S. Jorgensen, S. L. Singer, Pore-resolving simulation of char particle gasification using micro-CT, *Fuel* 224 (2018) 752–763. doi:10.1016/j.fuel.2018.03.117.
- [140] D. Liang, S. Singer, Pore-resolving simulations to study the impacts of char morphology on zone II combustion and effectiveness factor models, *Combustion and Flame* 229 (2021) 111405. doi:10.1016/j.combustflame.2021.111405.
- [141] C. B. Nguyen, J. Scherer, M. Hartwich, A. Richter, The morphology evolution of char particles during conversion processes, *Combustion and Flame* 226 (2021) 117–128. doi:10.1016/j.combustflame.2020.11.038.
- [142] C. B. Nguyen, J. Scherer, Q. Guo, S. Kriebitzsch, A. Richter, The shape development of spherical and non-spherical char particles in the flame zone of an entrained-flow gasifier – A numerical study, *International Journal of Heat and Mass Transfer* 149 (2020) 119220. doi:10.1016/j.ijheatmasstransfer.2019.119220.
- [143] S. Farazi, M. Sadr, S. Kang, M. Schiemann, N. Vorobiev, V. Scherer, H. Pitsch, Resolved simulations of single char particle combustion in a laminar flow field, *Fuel* 201 (2017) 15–28. doi:10.1016/j.fuel.2016.11.011.
- [144] T. Sayadi, S. Farazi, S. Kang, H. Pitsch, Transient multiple particle simulations of char particle combustion, *Fuel* 199 (2017) 289–298. doi:10.1016/j.fuel.2017.02.096.
- [145] A. Brandenburg, A. Johansen, P. A. Bourdin, W. Dobler, W. Lyra, M. Rheinhardt, S. Bingert, N. E. L. Haugen, A. Mee, F. Gent, N. Babkovskaia, C.-C. Yang, T. Heinemann, B. Dintrans, D. Mitra, S. Candelaresi, J. rn Warnecke, P. J. Käpylä, A. Schreiber, P. Chatterjee, M. J. Käpylä, X.-Y. Li, J. K. ger, J. rgen R. Arnes, G. R. Sarson, J. S. Oishi, J. Schober, R. Plasson, C. Sandin, E. Karchniwy, L. F. S. Rodrigues, A. Hubbard, G. Guerrero, A. Snodin, I. R. Losada, J. Pekkilä, C. Qian, The pencil code, a modular mpi code for partial differential equations and particles: multipurpose and multiuser-maintained, *Journal of Open Source Software* 6 (58) (2021) 2807. doi:10.21105/joss.02807.

- [146] J. R. Aarnes, N. E. L. Haugen, H. I. Andersson, High-order overset grid method for detecting particle impaction on a cylinder in a cross flow, *International Journal of Computational Fluid Dynamics* 33 (1-2) (2019) 43–58. [doi:10.1080/10618562.2019.1593385](https://doi.org/10.1080/10618562.2019.1593385).
- [147] J. R. Aarnes, T. Jin, C. Mao, N. E. L. Haugen, K. Luo, H. I. Andersson, Treatment of solid objects in the Pencil Code using an immersed boundary method and overset grids, *Geophysical & Astrophysical Fluid Dynamics* 114 (1-2) (2020) 35–57. [doi:10.1080/03091929.2018.1492720](https://doi.org/10.1080/03091929.2018.1492720).
- [148] A. Makino, T. Namikiri, K. Kimura, Combustion rates of graphite rods in the forward stagnation field with high-temperature airflow, *Combustion and Flame* 132 (4) (2003) 743–753. [doi:10.1016/S0010-2180\(02\)00537-0](https://doi.org/10.1016/S0010-2180(02)00537-0).

Chapter 5

Research papers

5.1 Paper I

The effect of turbulence on mass transfer rates between inertial polydisperse particles and fluid

Ewa Karchniwy, Adam Klimanek, Nils Erland L. Haugen

Journal of Fluid Mechanics, vol. 874, pp. 1147-1168, 2019

The effect of turbulence on mass transfer rates between inertial polydisperse particles and fluid

Ewa Karchniwy^{1,3,†}, Adam Klimanek³ and Nils Erland L. Haugen^{1,2}

¹Department of Energy and Process Engineering, Norwegian University of Science and Technology, Kolbjørn Hejes vei 1B, 7491 Trondheim, Norway

²SINTEF Energi AS, Sem Saelands vei 11, 7034 Trondheim, Norway

³Institute of Thermal Technology, Silesian University of Technology, Konarskiego 22, 44-100 Gliwice, Poland

(Received 4 April 2018; revised 12 June 2019; accepted 13 June 2019;
first published online 15 July 2019)

The current work investigates how turbulence affects the mass transfer rate between inertial particles and fluid in a dilute, polydisperse particle system. Direct numerical simulations are performed in which all scales of turbulence are fully resolved and particles are represented in a Lagrangian reference frame. The results show that, similarly to a monodisperse system, the mass transfer rate between particles and fluid decreases as a result of particle clustering. This occurs when the flow time scale (based on the turbulence integral scale) is long relative to the chemical time scale, and is strongest when the particle time scale is one order of magnitude smaller than the flow time scale (i.e. the Stokes number is around 0.1). It is also found that for larger solid mass fractions, the clustering of the heavier particles is enhanced by the effect of drag force from the particles on the fluid (momentum back-reactions or two-way coupling). In particular, when two-way coupling is accounted for, locations of particles of different sizes are much more correlated, which leads to a stronger effect of clustering, and thus a greater reduction of the particle–fluid mass transfer rate.

Key words: combustion, reacting multiphase flows, turbulent reacting flows

1. Introduction

Numerical simulations of multiphase systems in which small particles react with the embedding turbulent fluid are very complex. However, such systems are frequently encountered, especially in industry. Two excellent examples of this are pulverised coal combustion and fluidised bed combustion, which are two of the most popular technologies for thermal power generation. Given their popularity, it is not surprising that a lot of research is devoted to optimise and improve these processes. Representative examples of recent numerical studies are the works of Choi & Kim (2009) aimed at reduction of NO_x emission from pulverised coal combustion, Al-Abbas, Naser & Dodds (2012) who focused on oxy-fuel combustion of low-rank coal, Gubba *et al.* (2012) who investigated pulverised coal and biomass co-firing

† Email address for correspondence: ewa.karchniwy@polsl.pl

and Adamczyk *et al.* who examined different combustion technologies in fluidised bed (Adamczyk *et al.* 2015) and pulverised coal (Adamczyk *et al.* 2017) boilers. In all of the aforementioned publications, the focus is on industrial-scale simulations, which would not be feasible without the aid of modelling. Heat and momentum exchange between phases as well as all the stages of coal conversion, such as drying, devolatilisation and char burnout, are usually taken into account. All of these processes can be strongly influenced by turbulence and these interactions have to be modelled. Thus, it is apparent that the accuracy of such simulations depends on the completeness of the models and their capability of reflecting real-life phenomena.

On the other hand, the amount of modelling can be greatly reduced by using an extremely fine computational grid such that the entire range of turbulent scales, together with the associated effects on mass, momentum and heat transfer, are resolved. Such an approach, called a direct numerical simulation (DNS), has lately been applied in studies of pulverised coal combustion by Luo *et al.* (2012, 2017), Brosh & Chakraborty (2014), Brosh *et al.* (2015), Hara *et al.* (2015) and Muto, Yuasa & Kurose (2017), allowing for very detailed examination of coal ignition, flame stabilisation or interactions between vortices and coal particles. However, the DNS technique is restricted in its use to small-scale simulations (or very low Reynolds numbers) since its application to industrial-scale problems is prohibitively expensive in terms of computational power. It should also be mentioned that the smallest fluid scale that is resolved in the simulations presented in the literature cited above is the Kolmogorov scale. The Kolmogorov scale is defined as the scale of the smallest turbulent eddies, i.e. the scale where the kinetic energy is dissipated into heat. The boundary layer of the particles, which are smaller than the Kolmogorov size, is, however, not resolved. Hence, the boundary layer effects have to be modelled.

Over the years, extensive investigations of turbulent flows have been conducted, resulting in an abundance of models accounting for the effect of turbulence on flow transport properties. Amongst the well-established ones are the k - ϵ (Launder & Spalding 1974) and k - ω (Wilcox 1988) models, which relate the Reynolds stresses to the mean flow stresses through the eddy viscosity. There are also a number of models suitable for homogeneously reacting turbulent flows, such as the eddy dissipation model (Magnussen & Hjertager 1977), probabilistic descriptions relating instantaneous scalar fluctuations to their mean values (Pope 1985) or models for computing the turbulent flame speed (Zimont *et al.* 1998). In addition to this, there is much more modelling required when dealing with reacting multiphase flows; for example, the particle dispersion caused by the turbulence in particle-laden flows can be described using stochastic transport models (Baxter & Smith 1993; Graham 1996).

The above models are mature and well-tested, and most of them have numerous extensions. However, until very recently, no models existed that represent the impact of turbulence on heterogeneous reactions, such as char conversion. Therefore, in all industrial-scale simulations of pulverised coal combustion this effect is not captured. This knowledge gap was addressed by Krüger *et al.* (2017a) who proposed the first model to account for the mass transfer rate modifications due to turbulence for isothermal reactions. This work was later extended to non-isothermal reactions (Krüger, Haugen & Løvås 2017b). The numerical studies of Krüger *et al.* showed that under some circumstances, turbulence may cause the particles to form clusters, inside which the reactant is quickly consumed. As a result, there exist regions that are rich in reactants but lack particles, and regions where the particle density is very high but the reactant concentration is low. This leads to a considerable decrease in the overall mass transfer rate, which should not be neglected when performing

simulations of turbulent flows containing reacting particles. The work of Krüger *et al.* (2017a) was further extended by Haugen *et al.* (2018) who showed that turbulence may also enhance the mass transfer since it causes an increase in the relative velocity between phases. They proposed a model that accounts for both effects of turbulence on the reactant consumption rate. It was shown that which effect dominates depends on the Damköhler number, which is given by $Da = \tau_L / \tau_c$, where τ_L and τ_c are typical fluid (turbulence) and chemical time scales, respectively. For the remainder of this paper, τ_L is set to be equal to the turnover time of the integral-scale eddies. In these studies, monodisperse particle systems were studied, but in real situations, such as in pulverised coal-fired boilers, particles with different sizes are present. The current work aims to verify the previous findings of Krüger *et al.* (2017a) and Haugen *et al.* (2018) for polydisperse systems and to further investigate how the mass transfer is affected by the turbulence under different conditions.

Clustering of particles due to turbulence in an embedding fluid has been studied in a large number of papers (Eaton & Fessler 1994; Bec *et al.* 2007; Calzavarini *et al.* 2008; Toschi & Bodenschatz 2009; Baker *et al.* 2017; Haugen *et al.* 2018). It has been shown that for turbulence with a sufficient scale separation, clustering will occur for a range of Stokes numbers (Baker *et al.* 2017; Haugen *et al.* 2018). Conceptually, one can argue that particle clusters should be found at least for $\tau_\eta \leq \tau_p \leq \tau_L$, where τ_η is the Kolmogorov time scale and τ_p is the response time of the particles. Or, in other words, particle clusters should be found when $St_\eta = \tau_p / \tau_\eta > 1$ and $St_L = \tau_p / \tau_L < 1$. With this being said, it is clear that the sharpest clusters are found for $St_\eta \approx 1$ (Bec *et al.* 2007; Calzavarini *et al.* 2008; Toschi & Bodenschatz 2009). Even though the sharpest clusters are found at scales around the Kolmogorov scale, this does not necessarily mean that these clusters have the most influence on the mass transfer coefficients. The reason for this is that in order for the clustering to slow down the mass transfer, the life time of the clusters should be longer than the time it takes for the particles to consume most of the reactants within the cluster. This is typically not the case for these smallest clusters since their life times are too short.

2. Governing equations and numerical methods

As mentioned before, there is a large number of applications where heavy inertial particles are embedded in a turbulent flow. For many of these applications, there is also mass transfer between the particles and the fluid. The mass transfer may yield a net molar production (e.g. char oxidation to carbon monoxide or the reduction of a metal oxide by natural gas to produce steam and carbon dioxide), a net molar reduction (e.g. oxidation of a metal oxide) or it may be molar neutral (e.g. oxidation of char to carbon dioxide). On top of this, the reactions may be exothermic (e.g. oxidation of char or a metal oxide) or endothermic (e.g. gasification of char). The mass transfer rate may also be dependent on temperature, through the kinetic reaction rates at the particle surface. An example of the complexity can be seen in the detailed conversion model for single point particle char as described in, for example, Haugen, Tilghman & Mitchell (2014) and Haugen, Mitchell & Tilghman (2015). In order to make the results obtained in the following as general as possible, and to be able to isolate the effects of the turbulence alone, we will here use a simplified description of the chemical reactions. The main simplifications made in this work are that (1) heterogeneous reaction kinetics is assumed to be infinitely fast, (2) the reaction occurs only on the external surface of the spherical particles, (3) the reaction is of one step, unimolar and isothermal and (4) the evolution of particle size and density is not accounted for, i.e. the particle acts as a catalyst.

2.1. Fluid-phase equations

Fluid motion is governed by the continuity

$$\frac{D\rho}{Dt} + \rho \nabla \cdot \mathbf{u} = 0 \quad (2.1)$$

and the momentum equation

$$\rho \frac{D\mathbf{u}}{Dt} = \nabla \cdot \underline{\underline{\sigma}} + \rho \mathbf{f} - \mathbf{F}, \quad (2.2)$$

where $D/Dt = \partial/\partial t + \mathbf{u} \cdot \nabla$ is the advective derivative, ρ is the density of the fluid, \mathbf{u} is the velocity vector and $\underline{\underline{\sigma}}$ is the total stress tensor, which is defined as

$$\underline{\underline{\sigma}} = -p\underline{\underline{I}} + 2\mu\underline{\underline{S}} - \frac{2}{3}\mu(\nabla \cdot \mathbf{u})\underline{\underline{I}}, \quad (2.3)$$

when p and μ are pressure and dynamic viscosity, respectively. The rate of strain tensor is given by

$$\underline{\underline{S}} = \frac{1}{2}[\nabla \otimes \mathbf{u} + (\nabla \otimes \mathbf{u})^T]. \quad (2.4)$$

The remaining terms in (2.2) are \mathbf{f} and \mathbf{F} . The former is a forcing function, which is responsible for injecting kinetic energy into the domain (see Haugen *et al.* (2012) for details), while the latter represents momentum exchange between the fluid and particles and will be introduced in the next section.

Thermodynamic properties are coupled through the ideal gas equation:

$$p = \rho c_s^2, \quad (2.5)$$

in which c_s is the isothermal speed of sound. Additionally, the equation governing the reactant is given as

$$\frac{\partial X}{\partial t} + \mathbf{u} \cdot \nabla X = D\nabla^2 X - R, \quad (2.6)$$

where X stands for the reactant mole fraction, D is its diffusivity and R represents the rate of reaction occurring on the particle surface.

2.2. Dispersed-phase equations

Particles are represented as point sources and are tracked in a Lagrangian reference frame. For the point particle approach to be applicable, the particle size cannot be greater than the size of a fluid grid cell. Furthermore, a two-way coupling is applied, i.e. there are mutual interactions between particles and the fluid phase. Since the particle distribution is assumed to be dilute, particle collisions are neglected. The i th particle obeys the following equations of motion:

$$\frac{d\mathbf{x}_i}{dt} = \mathbf{v}_i, \quad (2.7)$$

$$m_i \frac{d\mathbf{v}_i}{dt} = m_i \mathbf{a}_i, \quad (2.8)$$

where m_i denotes its mass while \mathbf{x}_i and \mathbf{v}_i are its position and velocity vectors, respectively. Assuming that no forces other than drag act on the particle, its acceleration can be expressed as

$$\mathbf{a}_i = \frac{1}{\tau_i}(\mathbf{u}(\mathbf{x}_i) - \mathbf{v}_i), \quad (2.9)$$

where the particle response time is given by

$$\tau_i = \frac{1}{1 + f_i} \tau_{p,i}, \tag{2.10}$$

and the correction factor to account for the Reynolds number effect, as given by the empirical correlation of Schiller & Naumann (1933), is $f_i = 0.15Re_i^{0.687}$. Here, $Re_i = \rho|\mathbf{u}(\mathbf{x}_i) - \mathbf{v}_i|d_{p,i}/\mu$ is the particle Reynolds number. The Stokesian particle response time is given by

$$\tau_{p,i} = \frac{\rho_{p,i}d_{p,i}^2}{18\mu}, \tag{2.11}$$

where $d_{p,i}$ is the particle diameter and the particle material density is $\rho_{p,i}$. Momentum exchange is incorporated in the fluid-phase equations through the last term on the right-hand side of (2.2):

$$\mathbf{F} = \frac{1}{V_c} \sum_i m_i \mathbf{a}_i, \tag{2.12}$$

in which V_c is the volume of the relevant grid cell and the summation is over all particles located inside the same grid cell. Similarly, the term representing the rate of reaction in (2.6) is given as

$$R = \frac{1}{V_c} \sum_i A_i \kappa_i X, \tag{2.13}$$

where X is the reactant mole fraction in the cell in which the particle is located, $A_i = \pi d_{p,i}^2$ is the particle surface area and

$$\kappa_i = DSh_i/d_{p,i} \tag{2.14}$$

stands for the mass transfer coefficient, while

$$Sh_i = 2 + 0.6Re_i^{1/2} Sc^{1/3} \tag{2.15}$$

is the Sherwood number, as given by the empirical correlation of Ranz & Marshall (1952), and $Sc = \mu/(D\rho)$ is the Schmidt number. In obtaining (2.13) it has been assumed that the particle reactions are diffusion controlled, i.e. that a reactant will react instantly when it reaches the particle surface.

2.3. Characteristic scales and non-dimensional numbers

Before presenting the results, it is worthwhile introducing some relevant dimensionless numbers. There are two characteristic time scales for turbulent flows: the turnover time of the integral scale

$$\tau_L = \frac{L}{u_{rms}} \tag{2.16}$$

and the time scale of the Kolmogorov scale eddies at which energy is dissipated

$$\tau_\eta = \left(\frac{\nu}{\epsilon}\right)^{1/2}. \tag{2.17}$$

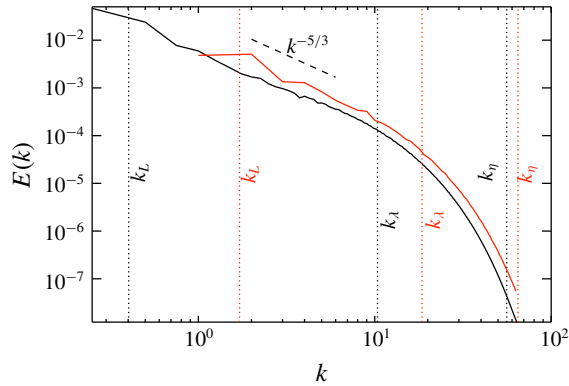


FIGURE 1. (Colour online) Kinetic energy spectrum; black: $Re_\lambda \approx 350$, red: $Re_\lambda \approx 150$ (cases A and M in table 1). The wavenumbers k_L , k_λ and k_η correspond to the integral, Taylor and Kolmogorov scales, respectively.

Here, u_{rms} is the root-mean-square velocity and the integral length scale of turbulence is given by (Pope 2000)

$$L = \frac{k^2}{u_{rms}\epsilon} = \frac{u_{rms}^3}{4\epsilon}, \quad (2.18)$$

where $\nu = \mu/\rho$ represents kinematic viscosity and ϵ is the dissipation rate of turbulent kinetic energy. Note that the above definition of the integral scale is different from the one employed by Krüger *et al.* (2017a) and Haugen *et al.* (2018). In their work, a turbulent forcing scale $L_f = L_x/(2\pi k_f)$, where L_x is the domain size and k_f is the forcing wavenumber, was used as the integral scale. The two scales, L and L_f , are not the same. Indeed, $L \approx 2\pi L_f$, which means that also several non-dimensional numbers, such as the Damköhler number and the Stokes number based on the integral scale, are roughly a factor 2π different from the ones used by Krüger *et al.* (2017a) and Haugen *et al.* (2018). The reason for defining the integral scale differently from what was done in Krüger *et al.* (2017a) and Haugen *et al.* (2018) was that L_f was not really an integral scale but merely a scale that was used to define a suitable Reynolds number. It can be seen from comparing the integral wavenumber, $k_L = 2\pi/L$, with the energy spectrum, which is what is done in figure 1, that the current integral scale does indeed represent a size that is reasonably close to the real integral scale. In the figure, also the Taylor microscale and the Kolmogorov scales are shown, for both $Re_\lambda = 150$ (red) and $Re_\lambda = 350$ (black).

Under the assumption of Stokes flow, the particle time scale (τ_p) is given by (2.11). Yet another scale, characteristic for reacting flows, is the chemical time scale. The reactant consumption rate for homogeneous reactant and particle distributions can be defined as

$$\alpha_{hom} = \overline{R/X} = \overline{Sh\pi n_p D \overline{d_p}}, \quad (2.19)$$

where overline means volume averaging and (2.13) and (2.14) have been employed. If we assume that the relative velocity between the particles and the fluid is negligible, such that $Sh = 2$ (see (2.15)), the reactant consumption rate then becomes

$$\alpha_{qsc} = 2\pi n_p \overline{D d_p}. \quad (2.20)$$

Case	\bar{d}_p	ρ_p	L_x	\bar{Sh}	Re_λ	\bar{St}_L	α_c	Da_2	Range of St_L	Range of St_η	τ_L/τ_η
Compensated distribution											
A	0.013	1.0	2π	2.4	150	0.005	1.11	38.6	0.0013–0.013	0.04–0.4	28
B	0.013	2.5	2π	2.5	150	0.01	0.67	22.2	0.0035–0.035	0.1–1.0	28
C	0.013	10	2π	2.8	150	0.05	0.38	11.9	0.014–0.14	0.39–3.9	28
D	0.013	25	2π	2.9	150	0.1	0.29	8.5	0.035–0.35	0.98–9.8	28
E	0.013	75	2π	3.1	150	0.35	0.34	9.25	0.1–1.0	2.9–29.9	28
F	0.013	250	2π	3.3	150	1.2	0.52	13.3	0.34–3.4	9.7–96.9	28
G	0.013	750	2π	3.4	150	3.5	0.70	17.4	1.0–10.2	28.8–288	28
L	0.021	1.3	8π	2.6	350	0.005	0.31	30.5	0.001–0.018	0.07–1.2	69
M	0.021	3.3	8π	2.8	350	0.01	0.19	17.7	0.0026–0.044	0.17–3.0	69
N	0.021	10	8π	3.0	350	0.04	0.13	10.9	0.0079–0.13	0.53–9.2	69
O	0.021	25	8π	3.2	350	0.09	0.11	8.6	0.02–0.34	1.36–23.2	69
P	0.021	332	8π	3.9	350	1.2	0.19	12.8	0.26–4.4	18–98.9	69
Uniform distribution											
Q	0.010	202	8π	3.0	350	0.26	n/a	n/a	0.034–0.85	2.0–49.4	69
H	0.00047	33567	2π	2.2	150	0.29	n/a	n/a	0.038–0.96	0.93–23.3	28
I	0.015	10	2π	2.8	150	0.06	0.37	11.0	0.014–0.14	0.39–3.9	28
J	0.015	20	2π	2.9	150	0.1	0.32	9.1	0.028–0.28	0.78–7.8	28
Gaussian distribution											
K	0.015	20	2π	3.0	150	0.1	0.31	8.9	0.027–0.27	0.78–7.8	28

TABLE 1. Simulation parameters. The total number of grid points varies between 64^3 and 512^3 , depending on Re_λ and Da . In all cases, the Schmidt number is equal to 0.2. The parameter Da_2 quantifies the effect of particle clustering and is explained in a later subsection.

Here, n_p is the particle number density and \bar{d}_p is the average particle diameter. The chemical time scale is now defined as

$$\tau_c = \frac{1}{\alpha_{qsc}}. \tag{2.21}$$

By combining the above time scales, one can define several dimensionless numbers, such as the Damköhler number

$$Da = \frac{\tau_L}{\tau_c}, \tag{2.22}$$

the Stokes number based on the integral scale

$$St_L = \frac{\tau_p}{\tau_L} \tag{2.23}$$

and the Kolmogorov-based Stokes number

$$St_\eta = \frac{\tau_p}{\tau_\eta}. \tag{2.24}$$

Naturally, in a polydisperse system, a range of Stokes numbers can be identified since the Stokes number is a function of the particle diameter. However, to make the

analysis clear, the mean Stokes number will in the following be calculated based on a mean particle diameter, such that

$$\overline{St}_L = \overline{\tau}_p / \tau_L \quad (2.25)$$

when

$$\overline{\tau}_p = \frac{\rho_p \overline{d}_p^2}{18\mu}. \quad (2.26)$$

While it is generally accepted that the particle clustering is strongest when $St_\eta \approx 1$, we chose to present the results in terms of St_L . This is, as already discussed in the introduction, because we expect these larger-scale clusters (i.e. clusters formed by the larger eddies) to have a greater influence on the mass transfer rate due to their longer life times.

2.4. Reactant decay rate

It has been confirmed by numerous numerical and experimental studies that particles embedded in a turbulent flow have a tendency to cluster (Eaton & Fessler 1994; Yoshimoto & Goto 2007; Monchaux, Bourgoïn & Cartellier 2012). The formation of such clusters is primarily due to the turbulent eddies that have time scales that are comparable to the particle response time. From this, it follows that also the cluster size depends on the Stokes number, as shown by Haugen *et al.* (2018). For very low St , mainly the smallest eddies lead to clustering, which results in many small clusters present in the flow. When the Stokes number is close to or above unity, clustering is caused by the integral scale eddies, and thus the clusters are larger.

As Krüger *et al.* (2017a) demonstrated, the extent to which particle clustering affects the rate of mass transfer depends on the Damköhler number. If $\tau_c > \tau_L$, i.e. Da is low, the amount of reactant inside the particle clusters is similar to what it is outside of the clusters; thus, the effect of the clustering is negligible and the reactant consumption rate is similar to what is found for homogeneous particle and reactant distributions, and as such, can be computed from (2.19). However, if $\tau_c < \tau_L$, which corresponds to high Da , a significant fraction of the reactant inside the clusters is consumed during the life time of the cluster. In this situation, clustering plays an important role as it leads to a decrease of the rate at which the reactant is consumed because the average particle sees a reactant concentration that is significantly lower than the average reactant concentration in the fluid. Krüger *et al.* (2017a) proposed to incorporate this effect in a formulation of the reactant decay rate, such that the real decay rate is given by

$$\alpha_{mod} = 1 / \left(\frac{1}{\alpha_{hom}} + \frac{1}{\alpha_c} \right), \quad (2.27)$$

where α_c may be interpreted as a cluster characteristic decay rate. This parameter is generally dependent on the cluster properties, such as size, shape and number density.

While clustering of particles will decrease the mass transfer rate between particles and fluid, there is another turbulence-induced effect that will enhance the mass transfer rate. This effect is due to the fact that particles will not be significantly accelerated by turbulent eddies that have time scales that are shorter than the response time of the particles. This means that such fast turbulent eddies will yield a relative velocity

difference between the particles and the fluid. Haugen *et al.* (2018) demonstrated the effect of this and described how it can be modelled (see their equation (3.14)).

Finally, Haugen *et al.* (2018) showed that the combined effect of turbulence on the mass transfer rate between particles and fluid can be expressed solely through a modified Sherwood number, which is given by

$$Sh_{mod} = 2\tilde{\alpha} = 2 \frac{\alpha_{mod}}{\alpha_{qsc}}. \quad (2.28)$$

Using the above while employing (2.19)–(2.22) together with (2.27) yields

$$\tilde{\alpha} = \frac{\overline{Sh}}{2} \frac{\alpha_c \tau_L}{\alpha_c \tau_L + Da \overline{Sh}/2}. \quad (2.29)$$

In the following, the predictions of (2.29) will be compared with the time-averaged reactant decay rate obtained from the DNS

$$\langle \alpha \rangle = \frac{1}{t - t_0} \int_{t_0}^t \alpha(t) dt, \quad (2.30)$$

where $\langle \cdot \rangle$ represents time averaging,

$$\alpha(t) = - \frac{1}{\overline{X}} \frac{d\overline{X}}{dt} \quad (2.31)$$

is the volume-averaged decay rate and the integration starts at t_0 , which is when the statistically stationary state is reached and \overline{X} is initialised to unity.

2.5. Computational methods and simulation set-up

A cubic computational domain with sides of length 2π and periodic conditions prescribed for all boundaries is considered. Initially, particles are randomly distributed in a turbulent flow field. This is achieved by performing simulations only of the fluid phase until the turbulence is statistically stationary before inserting the particles. Also, the turbulent field is statistically invariant under translations and rotations, i.e. it is homogeneous and isotropic.

The modelling approach employed in the current work is almost identical to the one used by Krüger *et al.* (2017a) and Haugen *et al.* (2018) with the difference that now a polydisperse particle system is considered. The key points of the approach are as follows. The DNS technique is applied, which means that the flow is resolved on the numerical grid down to the smallest turbulent scales. Therefore, since all the scales of the turbulence are resolved on the numerical mesh, only the interactions between phases (such as mass and momentum exchange between fluid and particles) require modelling due to the point-particle approximation. The accuracy of results is ensured by using high-order numerical methods, i.e. a third-order Runge–Kutta scheme for time advancement and a sixth-order finite-difference scheme for spatial derivatives, as implemented in the Pencil Code (Pencil Code), which is the software used for all simulations.

Various particle size distributions are studied, where the upper and lower particle diameter cut-offs are given by d_{max} and d_{min} , respectively. The first distribution is referred to as the ‘uniform distribution’ and corresponds to the situation when the

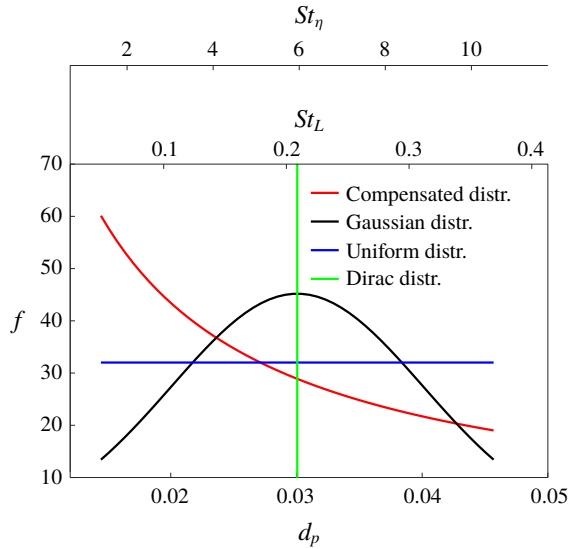


FIGURE 2. (Colour online) Particle size distributions used in the current work (for $Re_\lambda = 150$, $\overline{St}_L = 0.1$).

probability of picking a random particle with a given diameter is equal for all diameters between d_{max} and d_{min} . Since the Damköhler number associated with a given particle size is proportional to the particle diameter, it follows that for this particle size distribution, the contribution to the total Damköhler number is larger for the larger particles. To see the effect when the contribution to the total Damköhler number is the same for all particle sizes, the particles are distributed such that the particle number density is given by $n_p(d_p) \sim 1/d_p$, which is referred to as the ‘compensated distribution’. Finally, a Gaussian distribution (with a standard deviation $\sigma = 1/12(d_{max} - d_{min})$) is considered. The above-mentioned particle size distributions are shown in figure 2. A Dirac distribution is also included, which corresponds to a single particle size, as used by Haugen *et al.* (2018) for simulations of monodisperse systems.

Although we characterise the polydisperse system using the Stokes number defined based on the average-sized particle, it is important to remember that a broad range of Stokes numbers is contained in such a system. Figure 2 shows the normalised particle number density as a function of the Stokes numbers computed based on the integral (St_L , middle axis) and the Kolmogorov (St_η , top axis) time scales. (The values of Stokes numbers on the axes are relevant to the case in which the compensated distribution was used and the average Stokes number was approximately equal to 0.1.) It can be seen that for the smallest particles St_η is close to unity, while for large particles St_L is around 0.3. In order for particles to cluster, the time scale of the particles must be similar to some of the time scales in the flow (i.e. $\tau_\eta \leq \tau_p \leq \tau_L$). This means that in the case of these polydisperse systems, a wide range of eddies can contribute to clustering. Furthermore, since the size of the cluster depends on the Stokes number, clusters of various sizes may be present.

3. Results

In this section, the influence of turbulence on the mass transfer in polydisperse particle systems is studied by numerical simulations and the results are discussed and compared with previous results for monodisperse systems (Krüger *et al.* 2017a; Haugen *et al.* 2018). Simulation parameters are presented in table 1. For each case, a series of simulations with different Damköhler numbers were performed. The Damköhler number was altered by changing the particle number density. To control the Stokes number, the particle material density was varied. In most cases, the Taylor microscale Reynolds number, defined as $Re_\lambda = u'\lambda/\nu$, where the Taylor microscale is given by $\lambda = u'\sqrt{15\nu/\epsilon}$ and $u' = u_{rms}/\sqrt{3}$, is approximately 150. Additionally, for selected cases the domain size and the root-mean-square velocity (u_{rms}) were increased, resulting in a higher Reynolds number ($Re_\lambda \approx 350$). This was done in order to obtain a larger-scale separation in the flow in order to better understand the effect of a polydisperse particle size distribution. Kinetic energy spectra for both Reynolds numbers are shown in figure 1. It can be seen that for the higher Reynolds number the spectra extends to lower wavenumbers, while the wavenumbers of the Kolmogorov scale (k_η) are similar for both Re .

3.1. Shape of size distribution

The normalised reactant decay rate ($\tilde{\alpha} = \langle \alpha \rangle / \alpha_{qsc}$) obtained from the DNS for different particle size distributions is shown in figure 3 as a function of Damköhler number. Since the normalising factor is the decay rate computed as if the flow was quiescent, $\tilde{\alpha}$ shows the range of Da for which the mass transfer is enhanced ($\tilde{\alpha} > 1$) or decreased ($\tilde{\alpha} < 1$) due to turbulence. For the purpose of comparison, the equivalent results obtained by Haugen *et al.* (2018) with monodisperse particles are included as well ('Dirac distr.'). The error bars in figure 3, as well as in all of the following figures, represent the standard deviation of the results. In the model (2.29), the reactant consumption rate for high Da is controlled by the cluster decay rate (α_c). This parameter is generally unknown; therefore, it was used as a fit parameter to make the model predictions (2.29) fit the simulation results (2.30). Its values are listed in table 1.

From figure 3, it can be seen that there is no significant difference between the normalised decay rates computed for $\overline{St}_L = 0.1$ with Gaussian, uniform and compensated distributions (cases K, J and D, respectively). The effect of the Dirac distribution will be discussed in a later sub-section.

3.2. Particle clustering and the effect of momentum back-reactions

It is not possible to change the Damköhler number while maintaining Re_λ and St constant, since variations in particle mass loading will influence the root-mean-square velocity. Indeed, as was shown by Krüger *et al.* (2017a), u_{rms} , and consequently also the Reynolds and Stokes numbers, decrease when the mass loading is high. In order to verify if this impacts the results, a series of simulations without back-reaction from the particles to the fluid, i.e. where $\mathbf{F} = 0$ in (2.2), were performed. Without particle feedback, the results are less representative in terms of physics but u_{rms} remains unchanged irrespective of Da . Figure 4 compares the obtained normalised reactant consumption rate as a function of Da . It can be seen that as long as the Stokes number is low, the difference between the results with and without back-reactions from particles to fluid is almost negligible. However, this is not the case for higher

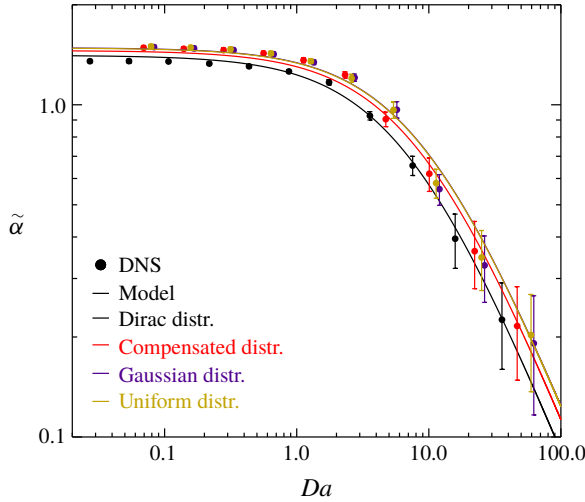


FIGURE 3. (Colour online) Normalised decay rate as a function of Damköhler number obtained for different particle size distributions for $\overline{St}_L = 0.1$ (cases D, J, K).

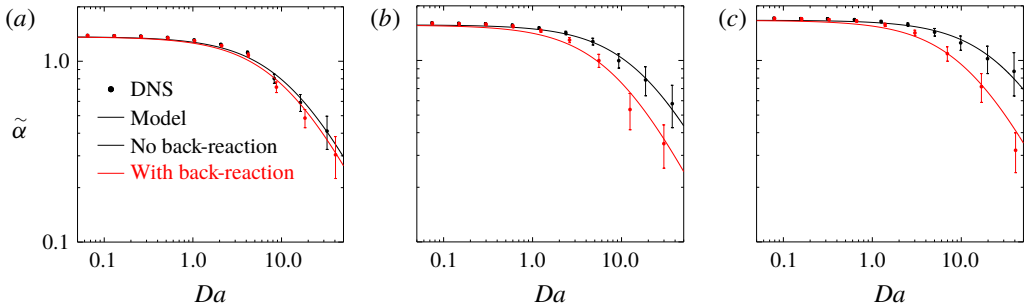


FIGURE 4. (Colour online) Comparison of the normalised decay rate obtained with and without particle back-reaction for simulations with $\overline{St}_L = 0.05$ (a), 0.35 (b) and 1.2 (c) (cases C, E, F).

\overline{St}_L , for which the difference becomes significant at high Damköhler numbers. This is because the mass loading is proportional to the Stokes number for a given Damköhler number. An expression for the mass loading as a function of non-dimensional numbers is given in appendix A.

The assumption has been that particles cluster purely due to turbulent eddies that are associated with a time scale that is similar to the particle response time. Then, if the location of turbulent eddies of different sizes were not correlated, particles of different sizes should cluster in uncorrelated positions. This is however not the case, as can be seen from the particle number density plots in figure 5. Here, the three upper (lower) panels present the results of a single simulation in which particle back-reactions were (were not) included, and the reported Stokes numbers correspond to different particle sizes. The strength of the dependency between particle locations can be demonstrated in a quantitative manner using correlation numbers. The correlation

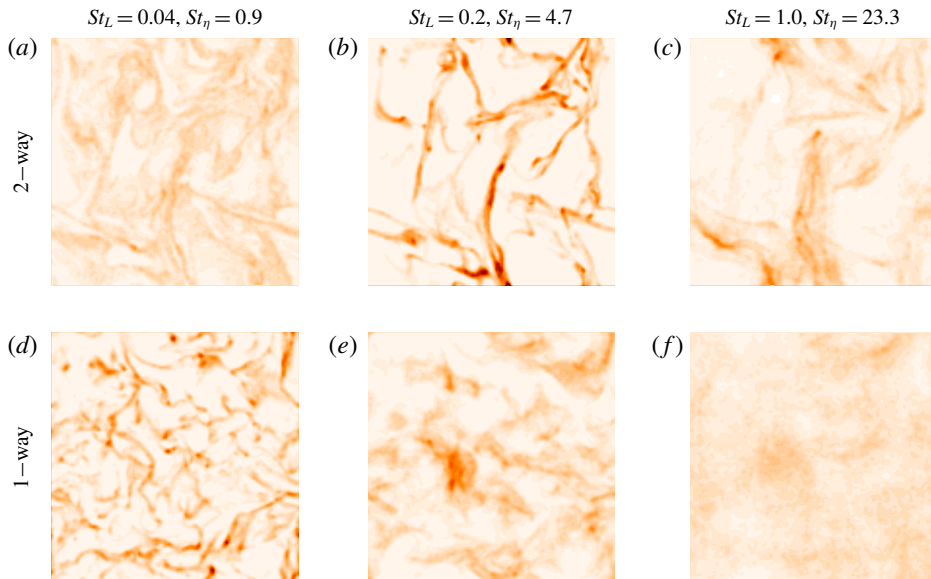


FIGURE 5. (Colour online) Particle number density for different Stokes numbers (case H). (*a–c*) Simulations with two-way coupling between particles and fluid; (*d–f*) only one-way coupling (no back-reactions from particles on fluid) is accounted for. White corresponds to zero particle number density, while black represents a particle number density that is 23 times larger than the average.

number of the number density of particles with different sizes is given as

$$C_{ij} = \frac{\overline{\tilde{n}_i \tilde{n}_j}}{\sqrt{\overline{\tilde{n}_i^2}} \sqrt{\overline{\tilde{n}_j^2}}}, \quad (3.1)$$

where $\tilde{n}_i = n_i - \bar{n}_i$ and n_i is the particle number density of particles with size i . The corresponding values are presented in table 2 for simulations with and without back-reactions (i.e. one-way and two-way coupling). The Stokes numbers of the three different particle sizes are 0.04, 0.2 and 1, the same as in figure 5. It is clear from the table that the clusters of particles with different particle sizes are more correlated when the fluid can feel the presence of the particles (two-way coupling). The exception is the correlation between the two largest particle sizes, which is independent of back-reactions.

It is also clear, however, that there is still some correlation between the position of clusters of different sizes also for the case with only one-way coupling. This correlation is due to the fact that the locations of turbulent eddies of different sizes are (weakly) correlated, even for isotropic turbulence that does not feel the presence of the particles.

By inspecting the ‘strength’ or ‘sharpness’ of the clusters in figure 5 it can be observed that for the one-way coupling the sharpest structures are found for the smallest Stokes number. This is as expected since this case has a Kolmogorov-based Stokes number of $St_\eta \approx 1$, which is known to yield the sharpest clustering (Bec *et al.* 2007). For the one-way coupling, the sharpness of the clusters is decreasing with increasing Stokes numbers. If we now consider the case with two-way coupling, we

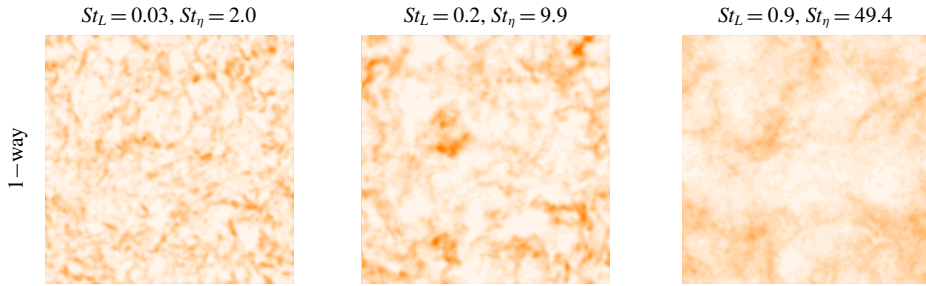


FIGURE 6. (Colour online) Particle number density for different Stokes numbers (case Q), one-way coupling, $Re_\lambda \approx 350$.

	C_{12}	C_{13}	C_{23}
One-way	0.29	0.10	0.26
Two-way	0.35	0.22	0.25

TABLE 2. The correlation number between different Stokes numbers ($St = 0.04, 0.2$ and 1), for simulations with and without back-reactions.

see that the trends are different. For the two-way coupling, the sharpest clusters are found for the intermediate Stokes number ($St_\eta \approx 5$), while also the largest Stokes number has sharper structures than is the case for the largest Stokes number with one-way coupling.

It is now interesting to see what happens if the Reynolds number is increased while St_L is kept unchanged. In figure 6 a contour plot of the particle number density is shown for $Re_\lambda \approx 350$ when particle back-reactions are turned off (one-way coupling). This is comparable to what is shown for $Re_\lambda \approx 150$ in figure 5(d–f). In figure 6, the integral-based Stokes numbers are the same as they are in figure 5, but the Kolmogorov-based Stokes numbers are different. From the figure, we see that for the case with $Re_\lambda \approx 350$ the clusters for the smallest Stokes number are not as sharp as for $Re_\lambda \approx 150$. This difference is actually not due to the difference in Reynolds number, but rather due to the fact that the Kolmogorov-based Stokes number is 2 for the case with $Re_\lambda \approx 350$ while it is 1 for the smallest Stokes number case with $Re_\lambda \approx 150$. This difference in sharpness when increasing the Kolmogorov-based Stokes number slightly beyond unity is consistent with previous findings by Bec *et al.* (2007). For the larger Stokes numbers we see that, within error bars, the clustering is independent of Re_λ . This is reasonable since the particles with $\tau_p \gg \tau_\eta$ are essentially independent of what happens at the Kolmogorov scale.

It can also be observed from figure 5 that cluster size and strength depend on the Stokes number and the way the fluid–particle coupling is handled. These features can be analysed using the auto-correlation function of the particle number density, which is given by

$$C_i(r) = \langle \tilde{n}_i(\mathbf{x}) \tilde{n}_i(\mathbf{x} + \mathbf{r}) \rangle \quad (3.2)$$

and is shown in figure 7. The faster the auto-correlation function decreases the more compact are the clusters. The distance at which $C(r)$ crosses the x -axis indicates the cluster length scale. Thus, for the smallest particles the clusters are larger and more diffusive in the case of two-way coupling, whereas the opposite is true for larger

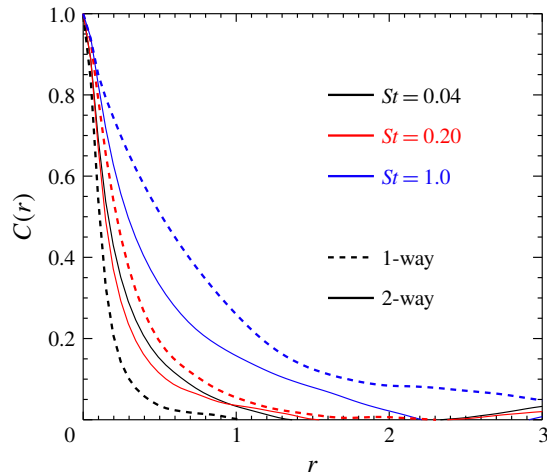


FIGURE 7. (Colour online) The auto-correlation function of the particle number density for simulations with and without back-reactions and for different particle sizes (case H).

particles. It is also interesting to note that for the larger particle sizes, the clustering is stronger when two-way coupling is invoked. The reason for the stronger clustering with two-way coupling is most likely that turbulence inside the heavy clusters will be suppressed by the presence of the particles, which means that the clusters will be relatively stable, while more particles can still be transported to the cluster. This transport of particles from volumes of high turbulence intensity to volumes of low turbulence is similar to the turbophoretic transport that is experienced for isotropic and non-homogeneous turbulence (Mitra, Haugen & Rogachevskii 2018).

In order to understand this effect better, we plot the probability density function (p.d.f.) of the particle number density for simulations with different mean Stokes numbers and for realisations with and without momentum back-reactions in figure 8. By inspecting the figure, it can be seen that the p.d.f. of the particle number density for simulations with $St_L = 1.2$ (figure 8*a,c*) is significantly wider for the case with back-reactions (figure 8*a,b*) than for the case without back-reactions (figure 8*c,d*). In particular we see that for the smallest particle sizes, there is a much higher probability of finding sub-volumes where there are no particles. Likewise, the probability of finding sub-volumes with high particle number densities is also higher. This means that the particle clustering is stronger for cases with back-reactions. It can also be seen that back-reactions have a stronger effect for large \bar{St}_L (figure 8*a,c*), while the effect is much less pronounced for smaller \bar{St}_L (figure 8*b,d*). This is due to the fact that the mass loading scales with the Stokes number, which means that for small Stokes numbers the effect of back-reactions on the fluid is negligible.

3.3. Effect of back-reactions on reactant concentrations

From figure 4 it is seen (through the fact that $\tilde{\alpha}$ is above unity for larger Da) that the effect of clustering is less when momentum back-reactions from the particles to the fluid are neglected, i.e. when \mathbf{F} in (2.2) is set to zero. The reason for this can be understood from the previous sub-section, which showed that particle clustering is stronger due to momentum back-reactions. More insight into this can be gained from

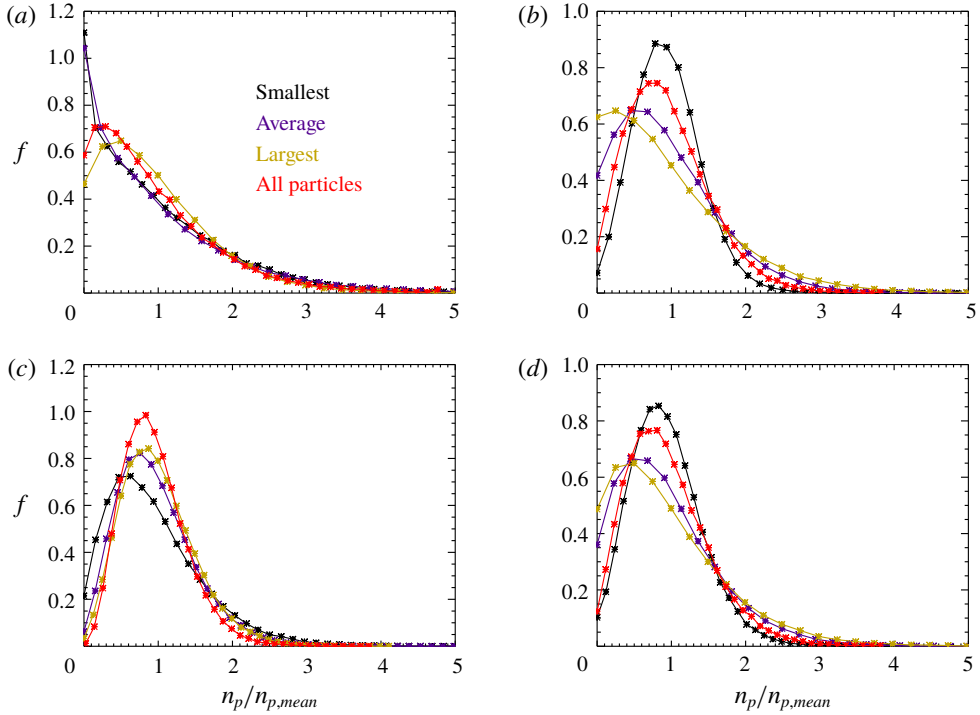


FIGURE 8. (Colour online) The p.d.f. of n_p/\bar{n}_p for different particle sizes, $Re_\lambda \approx 150$, compensated distr., (a,b) with back-reaction, (c,d) no back-reaction, (a,c) $\overline{St}_L = 1.2$, (b,d) $\overline{St}_L = 0.05$, in all cases $Da \approx 35$ (cases C and F).

figure 9, which shows the p.d.f. of the reactant mole fraction normalised by its mean value. Here, the curves referred to as ‘constrained’ are given by

$$f_C(z) = \frac{1}{N_{part}} \sum_{j=1}^{N_{part}} \delta(z - X(\mathbf{r}_j)), \quad (3.3)$$

and represent the p.d.f. obtained if data are collected at the position of the particles, δ is the Dirac delta function, N_{part} is the total number of particles in the domain and $X(\mathbf{r}_j)$ is the reactant concentration at the position of particle j . The ‘not constrained’ curves are obtained based on the reactant mole fraction present in the entire domain and are given by

$$f_{NC}(z) = \frac{1}{N_{grid}} \sum_{i=1}^{N_{grid}} \delta(z - X_i) \quad (3.4)$$

when N_{grid} is the total number of grid points and X_i is the reactant concentration in grid cell i . It becomes clear from figure 9 that the reactant distribution is significantly narrower when $\mathbf{F} = 0$, which is particularly pronounced for $\overline{St}_L = 1.2$ (figure 9a). A narrow distribution means that all particles have access to a similar amount of reactant. Hence, the clustering does not slow down the conversion rate so much.

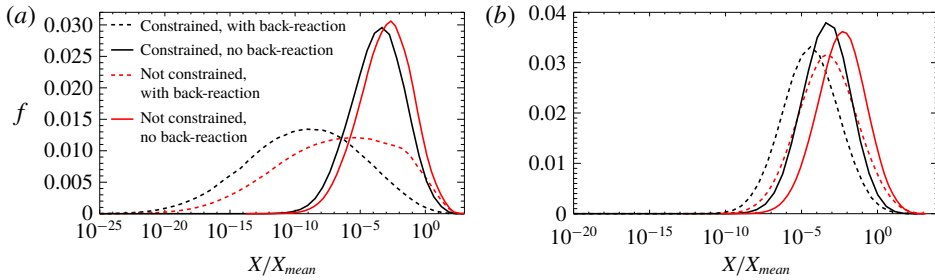


FIGURE 9. (Colour online) The p.d.f. of X/\bar{X} , (a) $\bar{St}_L = 1.2$, (b) $\bar{St}_L = 0.005$, compensated distribution, $Da \approx 35$ (cases C and F).

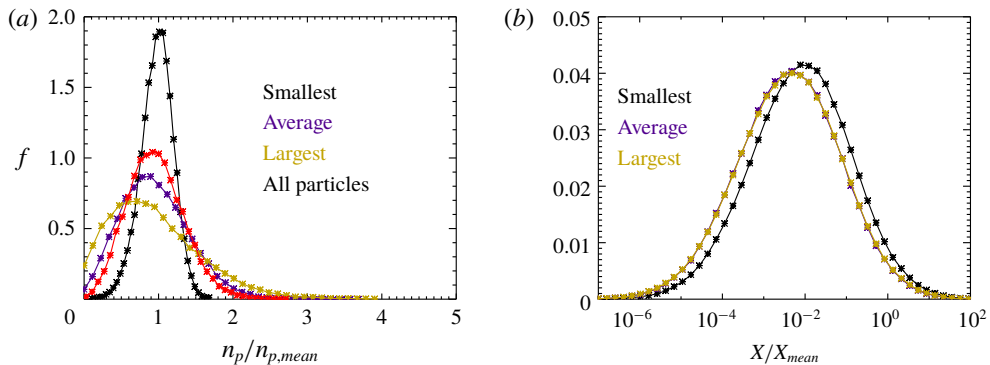


FIGURE 10. (Colour online) The p.d.f.s of (a) n_p/\bar{n}_p and (b) X/\bar{X} for different particle sizes, $Re_\lambda \approx 350$, compensated distr., with back-reaction, $\bar{St}_L = 0.04$, $Da = 25$ (case N).

3.4. The effect of turbulence on the overall mass transfer rate

Having gained an understanding of the interactions between differently sized particles in a polydisperse system, we can now study how the mass transfer rate is influenced due to turbulence. We begin by analysing p.d.f.s of particle number density and reactant mole fraction for different particle sizes for case N, in which $\bar{St}_L = 0.04$ and $Re_\lambda \approx 350$. These results, presented in figure 10, are the most representative for the considered polydisperse particle system since $\tau_{p,min} \approx \tau_\eta$ and $\tau_{p,max} < \tau_L$, which means that for all particle time scales there exists a turbulent flow time scale of the same order. Hence, turbulence can potentially make all particle sizes cluster. Despite the fact that the range of flow scales was significantly narrower for cases studied in previous sections (with $Re_\lambda \approx 150$), the p.d.f. of the particle number density presented in figure 10(a) verifies previous findings for the smaller Reynolds number. Here, again, the broadest p.d.f. is obtained for particles with St_L of the order of 0.1 (which corresponds to the largest particles in this simulation). As a consequence, we expect that the mass transfer rate will be mostly affected by clustering of these largest particles. The corresponding p.d.f.s of the reactant mole fraction (figure 10b) show that there is indeed slightly less reactant available at the locations of the largest particles. This is not surprising since they are more clustered and the clusters are larger, yielding longer cluster life times.

Normalised reactant decay rates for a compensated particle size distribution, $Re_\lambda \approx 150$ and different mean Stokes numbers (corresponding to cases A, B, D and F)

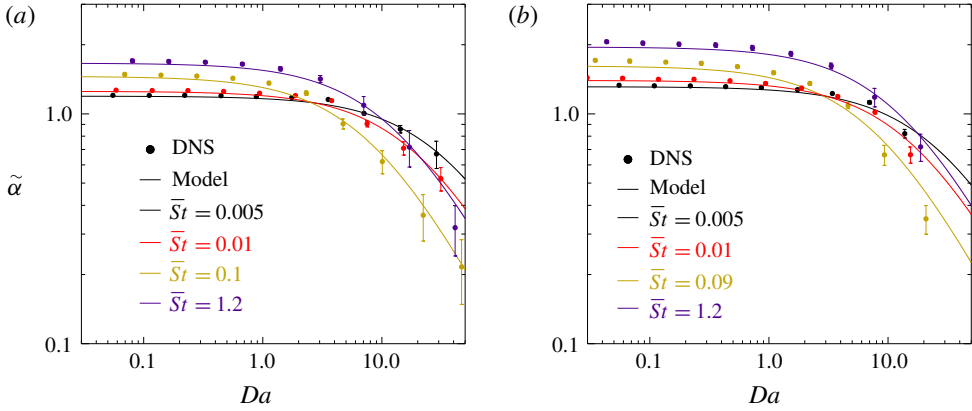


FIGURE 11. (Colour online) Normalised decay rate as a function of Damköhler number obtained for different \overline{St}_L using a compensated distribution for (a) $Re_\lambda \approx 150$ (cases A, B, D, F) and (b) $Re_\lambda \approx 350$ (cases L, M, O, P).

are shown in figure 11(a). The tendency here is the same as previously observed by Haugen *et al.* (2018). As long as the Damköhler number is low (or, in other words, as long as the mass transfer is not affected by the particle clustering), a higher normalised reactant decay rate is obtained for higher St_L , which is a consequence of the fact that the mean Sherwood number increases with Stokes number (see table 1). For higher Damköhler numbers, the reactant consumption rate starts to be dependent on the cluster decay rate. As expected, in the case of $\overline{St}_L = 0.005$, $\tilde{\alpha}$ begins to decrease only for relatively high Da , which can be interpreted as a weak effect of particle clustering due to the fact that for smaller Stokes numbers the corresponding clusters have shorter life times. As the Stokes number increases, the effect of clustering leads to a fast decrease of the normalised decay rate. This effect is again less when \overline{St}_L is further increased beyond unity since these heavy particles are less sensitive to the flow. The equivalent results for $Re_\lambda \approx 350$ (cases L, M, O and P) are presented in figure 11(b) from which it can be seen that the conclusions drawn for $Re_\lambda \approx 150$ are also true for the higher Reynolds number.

In order to assess if the effect of particle clustering is significant for a given set of parameters we employ the following quantitative description. It follows from (2.29) that when $Sh_{mod}/\overline{Sh} = 1/2$, i.e. when the effect of particle clustering has reduced the mass transfer rate to half of what it would have been if particle clustering was neglected, the Damköhler number is given by

$$Da_2 = \frac{2\alpha_c \tau_L}{\overline{Sh}}. \quad (3.5)$$

This is presented in figure 12, from which it is seen that in all of the investigated cases the effect of turbulence is at its strongest when $\overline{St}_L \approx 0.1$, which is where Da_2 takes the lowest value (note that the lower the value of Da_2 , the greater the influence of particle clustering). This is due to the fact that this yields a combination of relatively large and sharp clusters. For $\overline{St}_L < 0.1$ the clusters are smaller, while for $\overline{St}_L \gg 0.1$ the clusters are weaker because $St_L > 1$ for the largest particles, meaning that the particle concentrations are more homogeneous. For $Re_\lambda \approx 350$ (figure 12b), there is almost no difference between mono- and polydisperse particle systems. The same trend is

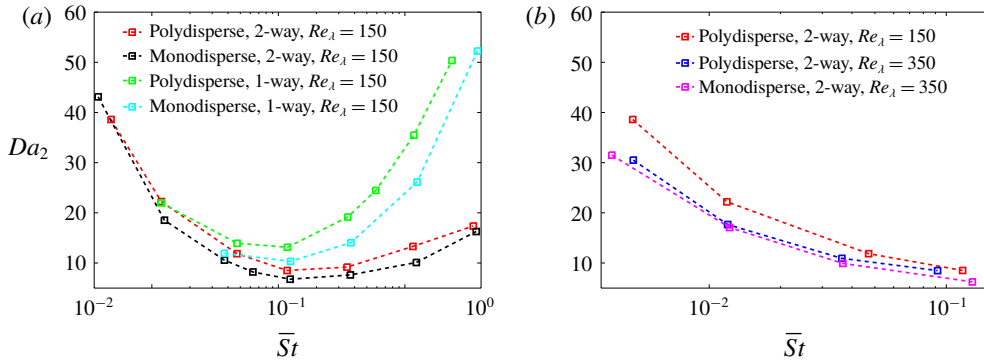


FIGURE 12. (Colour online) Damköhler number Da_2 as a function of Stokes number, all cases with compensated and Dirac distributions.

also seen for $Re_\lambda \approx 150$ (figure 12a), although slightly lower values of Da_2 indicate a stronger tendency to clustering of the monodisperse system. It can also be observed that the effect of turbulence is slightly stronger for higher Re_λ . This is probably due to the fact that in this case a broader range of flow scales contribute to particle clustering, i.e. there are more particles for which $\tau_\eta < \tau_p < \tau_L$. While for $\overline{St}_L < 0.1$, Da_2 is not much affected when the back-reaction from particles is neglected, there is a significant difference in the results when $\overline{St}_L > 0.1$, which is in line with the conclusions already drawn in previous sections.

We have shown that the effect of turbulence on reactive particles is due to a modified mass transfer coefficient, i.e. a modified Sherwood number. Chemical kinetics, however, is not directly affected by the turbulence, only indirectly through the reactant concentration. For purely kinetics-controlled reactions, this means that turbulence would not affect the conversion rate at all. The results presented in this work are formally applicable only to cases with diffusion-controlled reactions (fast kinetics). In reality, however, using the modified Sherwood number as described in this work will be correct also when the reactions are not diffusion-controlled. That is, for all kinetic rates, the correct rate of the reactions is obtained by using the traditional approach, which combines both kinetics and diffusion (see e.g. Haugen *et al.* 2015), as long as the diffusion is described with the use of the modified Sherwood number.

4. Conclusions

The effect of turbulence on the mass transfer rate in a dilute, polydisperse particle system was analysed over a range of conditions. We show that for polydisperse systems, the reaction rate is affected by particle clustering in the same way as for monodisperse systems. Even though particles of various sizes differ in the way they are distributed in the domain, this effect can be as strong as in a monodisperse system, provided that the scale separation in the flow is sufficiently large, or in other words, the Reynolds number is sufficiently high. When \overline{St}_L is of the order of 10^{-1} , the rate of mass transfer can be reduced by 50% even for Da lower than 10. It is therefore clear that, when studying real systems, the effect of turbulence on the overall mass transfer rate should be accounted for. The model given by (2.28) and (2.29) allows the incorporation of this effect directly in Reynolds-averaged Navier–Stokes-based

codes so that the model can be applied in simulations of large-scale reactors and boilers. It is found that the mass transfer rate is not very dependent on the shape of the particle size distribution, it is the width that matters.

We also observed that, despite having different sizes and hence different Stokes numbers, particles cluster in correlated positions. This correlation is greater when momentum transfer between fluid and particles is two-way. Both the distribution of reactant and particle number density are found to be broader when two-way coupling is applied. A direct consequence of this is that the mass transfer rate between the particles and the fluid is reduced due to the back-reaction of particle momentum to the fluid when the mass loading is significant.

Finally, it is worth pointing out that in reality the particle diameter (and/or material density) decreases as the surface reaction progresses. This will cause the Stokes number and the Damköhler number to decrease since $Da \sim d_p$ and $St \sim d_p^2$. As a result, the effect of turbulence may be different at initial and final stages of particle conversion. If the particle shrinkage model is used in a simulation, the effect it has on the particle conversion rate will be automatically included by recomputing the reactant decay rate every time step, such that $\tilde{\alpha} = \tilde{\alpha}(d_p(t))$.

Acknowledgements

The research leading to these results has received funding from the research project ‘Gaspro’, financed by the Research Council of Norway (267916). N.E.L.H. also acknowledges the Research Council of Norway under the FRINATEK grant 231444. This research was supported in part with computational resources provided by NOTUR (grant NN9405K). The work of A.K. was supported by the statutory research fund of the Silesian University of Technology, Faculty of Energy and Environmental Engineering, Gliwice, Poland.

Appendix A. Mass loading

The mass loading is given by

$$M = \frac{\tilde{\rho}_p}{\rho}, \quad (\text{A } 1)$$

when

$$\tilde{\rho}_p = \sum_i V_{p,i} n_{p,i} \rho_p, \quad (\text{A } 2)$$

and $V_{p,i} = (\pi/6)d_{p,i}^3$, $n_{p,i}$ and $d_{p,i}$ are the volume, radius and particle number density of particles with size i . The chemical time scale is now given by

$$\tau_c = \frac{1}{2\pi D \sum d_{p,i} n_{p,i}}, \quad (\text{A } 3)$$

such that

$$Da = 2\pi D \tau_f n_p \bar{d}_p, \quad (\text{A } 4)$$

when

$$\bar{d}_p^j = \frac{1}{n_p} \sum n_{p,i} d_{p,i}^j. \quad (\text{A } 5)$$

By this, the average Stokes number becomes

$$\bar{St}_L = \frac{\rho_p \bar{d}_p^2}{\rho \tau_f 18\nu}. \quad (\text{A } 6)$$

Combining the above equations yields

$$M = \frac{3}{2} Sc Da \bar{St}_L \frac{\bar{d}_p^3}{d_p^2 d_p} = \frac{3}{2} \frac{Sc Da \bar{St}_\eta}{\sqrt{Re}} \frac{\bar{d}_p^3}{d_p^2 d_p}, \quad (\text{A } 7)$$

since $\bar{St}_L = \bar{St}_\eta / \sqrt{Re}$. One can also avoid all reference to any turbulence property by introducing the non-dimensional number

$$\gamma = Da \bar{St}_L = \frac{\tau_p}{\tau_c}, \quad (\text{A } 8)$$

such that

$$M = \frac{3}{2} Sc \gamma \frac{\bar{d}_p^3}{d_p^2 d_p}. \quad (\text{A } 9)$$

REFERENCES

- ADAMCZYK, W. P., BIAŁECKI, R. A., DITARANTO, M., GLADYSZ, P., HAUGEN, N. E. L., KATELBACH-WOZNIAK, A., KLIMANEK, A., SLADEK, S., SZLEK, A. & WECHEL, G. 2017 CFD modeling and thermodynamic analysis of a concept of a mild-oxy combustion large scale pulverized coal boiler. *Energy* **140**, 1305–1315.
- ADAMCZYK, W. P., KOZOŁUB, P., KLIMANEK, A., BIAŁECKI, R. A., ANDRZEJCZYK, M. & KLAJNY, M. 2015 Numerical simulations of the industrial circulating fluidized bed boiler under air- and oxy-fuel combustion. *Appl. Therm. Engng* **87**, 127–136.
- AL-ABBAS, A. H., NASER, J. & DODDS, D. 2012 CFD modelling of air-fired and oxy-fuel combustion in a large-scale furnace at Loy Yang A brown coal power station. *Fuel* **102**, 646–665.
- BAKER, L., FRANKEL, A., MANI, A. & COLETTI, F. 2017 Coherent clusters of inertial particles in homogeneous turbulence. *J. Fluid Mech.* **833**, 364–398.
- BAXTER, L. L. & SMITH, P. J. 1993 Turbulent dispersion of particles: the STP model. *Energy Fuels* **7**, 852–859.
- BEC, J., BIFERALE, L., CENCINI, M., LANOTTE, A., MUSACCHIO, S. & TOSCHI, F. 2007 Heavy particle concentration in turbulence at dissipative and inertial scales. *Phys. Rev. Lett.* **98** (8), 084502.
- BROSH, T. & CHAKRABORTY, N. 2014 Effects of equivalence ratio and turbulent velocity fluctuation on early stages of pulverized coal combustion following localized ignition: a direct numerical simulation analysis. *Energy Fuels* **28**, 6077–6088.
- BROSH, T., PATEL, D., WACKS, D. & CHAKRABORTY, N. 2015 Numerical investigation of localised forced ignition of pulverised coal particle-laden mixtures: a direct numerical simulation (DNS) analysis. *Fuel* **145**, 50–62.
- CALZAVARINI, E., KERSCHER, M., LOHSE, D. & TOSCHI, F. 2008 Dimensionality and morphology of particle and bubble clusters in turbulent flow. *J. Fluid Mech.* **607**, 13–24.
- CHOI, C. R. & KIM, C. N. 2009 Numerical investigation on the flow, combustion and NO_x emission characteristics in a 500 MWe tangentially fired pulverized-coal boiler. *Fuel* **88**, 1720–1731.
- EATON, J. K. & FESSLER, J. R. 1994 Preferential concentration of particles by turbulence. *Intl J. Multiphase Flow* **20**, 169–209.

- GRAHAM, D. I. 1996 An improved eddy interaction model for numerical simulation of turbulent particle dispersion. *J. Fluids Engng* **118**, 819–823.
- GUBBA, S. R., INGHAM, D. B., LARSEN, K. J., MA, L., POURKASHANIAN, M., TAN, H. Z., WILLIAMS, A. & ZHOU, H. 2012 Numerical modelling of the co-firing of pulverised coal and straw in a 300 MWe tangentially fired boiler. *Fuel Process. Technol.* **104**, 181–188.
- HARA, T., MUTO, M., KITANO, T., KUROSE, R. & KOMORI, S. 2015 Direct numerical simulation of a pulverized coal jet flame employing a global volatile matter reaction scheme based on detailed reaction mechanism. *Combust. Flame* **162**, 4391–4407.
- HAUGEN, N. E. L., KRÜGER, J., MITRA, D. & LØVÅS, T. 2018 The effect of turbulence on mass transfer rates of small inertial particles with surface reactions. *J. Fluid Mech.* **836**, 932–951.
- HAUGEN, N. E. L., KLEEORIN, N., ROGACHEVSKII, I. & BRANDENBURG, A. 2012 Detection of turbulent thermal diffusion of particles in numerical simulations. *Phys. Fluids* **24**, 075106.
- HAUGEN, N. E. L., MITCHELL, R. E. & TILGHMAN, M. B. 2015 A comprehensive model for char particle conversion in environments containing O₂ and CO₂. *Combust. Flame* **162**, 1455–1463.
- HAUGEN, N. E. L., TILGHMAN, M. B. & MITCHELL, R. E. 2014 The conversion mode of a porous carbon particle during oxidation and gasification. *Combust. Flame* **161**, 612–619.
- KRÜGER, J., HAUGEN, N. E. L., MITRA, D. & LØVÅS, T. 2017a The effect of turbulent clustering on particle reactivity. *Proc. Combust. Inst.* **36**, 2333–2340.
- KRÜGER, J., HAUGEN, N. E. L. & LØVÅS, T. 2017b Correlation effects between turbulence and the conversion rate of pulverized char particles. *Combust. Flame* **185**, 160–172.
- LAUNDER, B. E. & SPALDING, D. B. 1974 The numerical computation of turbulent flows. *Comput. Meth. Appl. Mech. Engng* **3**, 269–289.
- LUO, K., BAI, Y., JIN, T., QIU, K. & FAN, J. 2017 Direct numerical simulation study on the stabilization mechanism of a turbulent lifted pulverized coal jet flame in a heated coflow. *Energy Fuels* **31**, 8742–8757.
- LUO, K., WANG, H., FAN, J. & YI, F. 2012 Direct numerical simulation of pulverized coal combustion in a hot vitiated co-flow. *Energy Fuels* **26**, 6128–6136.
- MAGNUSSEN, B. F. & HJERTAGER, B. H. 1977 On mathematical modeling of turbulent combustion with special emphasis on soot formation and combustion. *Symp. Combust.* **16** (1), 719–729.
- MITRA, D., HAUGEN, N. E. L. & ROGACHEVSKII, I. 2018 Turbulent Soret effect. *Eur. Phys. J.* **133**, 35.
- MONCHAUX, R., BOURGOIN, M. & CARTELLIER, A. 2012 Analyzing preferential concentration and clustering of inertial particles in turbulence. *Intl J. Multiphase Flow* **40**, 1–18.
- MUTO, M., YUASA, K. & KUROSE, R. 2017 Numerical simulation of ignition in pulverized coal combustion with detailed chemical reaction mechanism. *Fuel* **190**, 136–144.
- Pencil Code <http://www.nordita.org/software/pencil-code/>.
- POPE, S. B. 1985 PDF methods for turbulent reactive flows. *Prog. Energy Combust. Sci.* **11**, 119–192.
- POPE, S. B. 2000 Turbulent Flows, chap. 6, pp. 182–263. Cambridge University Press.
- RANZ, W. E. & MARSHALL, W. R. 1952 Evaporation from drops. Parts I and II. *Chem. Engng Prog.* **48**, 141–173.
- SCHILLER, L. & NAUMANN, A. Z. 1933 Über die grundlegenden berechnungen bei der schwerkraftaufbereitung. *Ver. Deut. Ing.* **77**, 318–320.
- TOSCHI, F. & BODENSCHATZ, E. 2009 Lagrangian properties of particles in turbulence. *Annu. Rev. Fluid Mech.* **41**, 375–404.
- WILCOX, D. C. 1988 Reassessment of the scale-determining equation for advanced turbulence models. *AIAA J.* **26** (11), 1299–1310.
- YOSHIMOTO, H. & GOTO, S. 2007 Self-similar clustering of inertial particles in homogeneous turbulence. *J. Fluid Mech.* **577**, 275–286.
- ZIMONT, V., POLIFKE, W., BETTELINI, M. & WEISENSTEIN, W. 1998 An efficient computational model for premixed turbulent combustion at high Reynolds numbers based on a turbulent flame speed closure. *Trans. ASME J. Engng Gas Turbines Power* **120**, 526–532.

5.2 Paper II

The effect of turbulence on mass transfer in solid fuel combustion: RANS model

Ewa Karchniwy, Nils Erland L. Haugen, Adam Klimanek, Øyvind Langørgen,
Sławomir Śladek

Combustion and Flame, vol. 227, pp. 65-78, 2021



Contents lists available at ScienceDirect

Combustion and Flame

journal homepage: www.elsevier.com/locate/combustflame

The effect of turbulence on mass transfer in solid fuel combustion: RANS model



Ewa Karchniwy^{a,b,*}, Nils Erland L. Haugen^c, Adam Klimanek^a, Øyvind Langørgen^c, Sławomir Śladek^a

^a Department of Thermal Technology, Silesian University of Technology, Konarskiego 22, Gliwice 44-100, Poland

^b Department of Energy and Process Engineering, Norwegian University of Science and Technology, Kolbjørn Hejes vei 1B, Trondheim NO-7491, Norway

^c SINTEF Energi A.S., Sem Saelands vei 11, Trondheim 7034, Norway

ARTICLE INFO

Article history:

Received 20 August 2020

Revised 14 December 2020

Accepted 28 December 2020

Available online 12 January 2021

Keywords:

Combustion kinetics

Combustion rates

Char oxidation

Diffusion regime

ABSTRACT

In this paper, a kinetic-diffusion surface combustion model is examined. The model is modified such that two effects of turbulence are included: 1) enhancement of the mass transfer due to relative velocity between particles and fluid and 2) reduction of the mass transfer due to turbulence-induced particle clustering. Details of the implementation are discussed and the influence of parameters such as air-fuel ratio, particle number density, particle diameter, turbulence intensity and characteristic length scales are studied theoretically. A simplified numerical model of a combustion chamber is created to explore the effects of the combustion model predictions. Finally, the model is incorporated into simulations of an industrial-scale boiler to investigate the effect of turbulence on the net surface reaction rate in a real system. The study shows that although on average this effect is rather minor, there exist regions in which the carbon conversion rate is either decreased or increased by turbulence.

© 2021 The Authors. Published by Elsevier Inc. on behalf of The Combustion Institute.

This is an open access article under the CC BY license (<http://creativecommons.org/licenses/by/4.0/>)

1. Introduction

Modelling of solid fuels combustion and gasification requires taking into account several important processes occurring during fuel conversion. A solid fuel particle injected into a hot environment is first heated up and dried. In the next stage devolatilization starts, which is a complex decomposition process associated with the release of multiple gaseous products. During the last stage of conversion, the remaining char is converted through reactions with the surrounding gas. In reality, a distinct separation between the processes can typically not be distinguished, and the drying and devolatilization, as well as devolatilization and char surface reactions overlap [1,2], in particular for large particles. The devolatilization is much faster than the char conversion, especially in gasification systems, where slow endothermic reactions are responsible for the char conversion rate. Many parameters affect the devolatilization process leading to different volatile compositions, total yield and reaction rate. A range of models have previously been developed, differing considerably by their complexity and accuracy, see

[2–5] for more detailed information on the process and its modelling.

The final stage of fuel conversion, i.e. the char conversion process, is affected by: the diffusion of reactants from the surrounding fluid to the particle surface, diffusion within particle pores, heterogeneous reactions at external and internal particle surfaces (including reactant gas adsorption and desorption), evolution of the char internal structure of pores, ash inhibition and thermal annealing [6]. Several approaches to char conversion modeling have been proposed in the literature. Among the most commonly used is the kinetic-diffusion surface reaction rate model [7,8] according to which the overall reaction rate can be influenced both by the reaction kinetics and the reactant diffusion. This model uses global kinetics and is computationally very efficient but it does not explicitly account for processes such as evolution of the char intrinsic surface area and pore diffusion, nor does it consider changes in particle diameter and density, variations in the particle reactivity [9], thermal deactivation or ash inhibition. A much more detailed approach that includes all of the above-mentioned processes is the Carbon Burnout Kinetics (CBK) model proposed by Hurt et al. [10] and further extended to oxidation and gasification at elevated pressure by Niksa et al. [11] and Liu & Niksa [12]. The CBK model was developed specifically to correctly predict char burnout and is able to capture a lower reactivity of chars at the final stage of

* Corresponding author at: Department of Thermal Technology, Silesian University of Technology, Konarskiego 22, Gliwice 44-100, Poland.

E-mail address: ewa.karchniwy@polsl.pl (E. Karchniwy).

conversion. However, the computational expense makes the model impractical to use in large-scale simulations [6]. More recently, groups at Stanford University and SINTEF have developed a model similar to the CBK model [13–15]. This model has a more accurate description of the size and density evolution of the char, together with a detailed intrinsic reaction mechanism. Annealing is, however, not included in this model.

Solid fuel combustion in industrial-scale facilities most often occurs under turbulent conditions. From the processes involved in char conversion mentioned above, turbulence primarily affects the efficiency of the reactant transport towards the particle surface. This effect of turbulence has been a subject of several recent studies [16–19]. Using Direct Numerical Simulations (DNS) and a simplified case in which a passive scalar (reactant) was consumed isothermally, the authors of [16,17] showed that turbulence might have two effects that counteract each other. Krüger et al. [16] demonstrated that the overall conversion rate can be reduced if the turbulent flow promotes particle clustering. This is related to the rapid oxidizer depletion due to increased concentration of particles in the clusters. These studies were extended by Haugen et al. [17] who showed that, in addition to particle clustering, turbulence can also increase the rate of heterogeneous reactions through velocity fluctuations that intensify the reactant transfer towards the particle surface. Furthermore, Haugen et al. [17] formulated a model that modifies the mass transfer coefficient to account for the two effects of turbulence and verified the model against their DNS results. These investigations were further extended to more realistic, non-isothermal conditions [18] and systems of polydisperse particles [19].

In the current study, we focus on the effects of turbulence on the mass transfer from the bulk gas to the particle surface. We discuss the model developed by Haugen et al. [17] and apply it to realistic combustion cases by utilizing the Reynolds Averaged Navier-Stokes (RANS) approach. Both main effects are considered: the enhancement of mass transfer through velocity fluctuations and the mass transfer rate reduction due to turbulence-induced particle clustering. We study the parameters affecting the process and show how the two effects of turbulence influence the char conversion in a jet of particles and in an industrial-scale boiler.

2. Theory

The reactant consumption rate of a fuel particle can be defined as the normalized quantity relating the rate of change of particle mass, m_p , and its initial mass, $m_{p,0}$,

$$\Theta = -\frac{1}{m_{p,0}} \frac{dm_p}{dt} \quad (1)$$

In order to reduce complexity of the analysis we limit our discussion to the context of char burnout. We apply a simple kinetic-diffusion model, with apparent rate kinetics. It should be stressed, however, that the analysis can be easily extended to more detailed models.

2.1. Kinetic-diffusion model

One of the most frequently used approaches in CFD modelling of solid fuels combustion and gasification is to apply the kinetic-diffusion model, given by

$$\Theta = \frac{\pi d_p^2 p_{ox}}{m_{p0}} \frac{1}{1/R_{dif} + 1/R_{kin}}, \quad (2)$$

where d_p is the particle diameter, p_{ox} is the partial pressure of oxidizer, R_{dif} is the reaction rate due to diffusion defined as

$$R_{dif} = \frac{C}{d_p} \left(\frac{T + T_p}{2} \right)^{3/4} \quad (3)$$

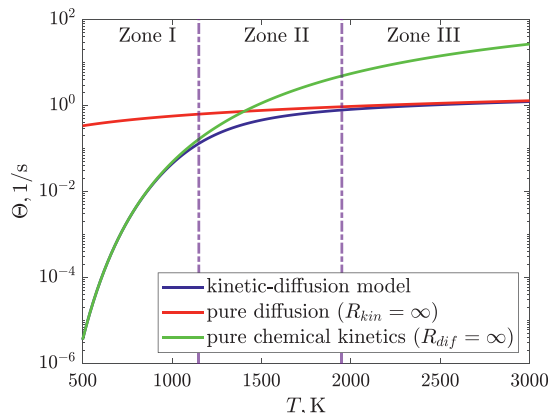


Fig. 1. The kinetic-diffusion model for $T_p = T$, $\rho_p = 800 \text{ kg/m}^3$, $d_p = 500 \text{ }\mu\text{m}$, $A = 0.002 \text{ s/m}$, $E = 79 \text{ kJ/mol}$, $C = 5 \cdot 10^{-12} \text{ sK}^{-3/4}$.

and R_{kin} is the kinetic reaction rate, which is often written in the Arrhenius form

$$R_{kin} = A \exp\left(-\frac{E}{RT_p}\right). \quad (4)$$

In the above equations C is a constant, T_p and T are the temperatures of the particle and of the gas surrounding the particle, respectively, A is the pre-exponential factor, E is the activation energy, and R is the universal gas constant. The kinetic rate R_{kin} is the apparent rate, therefore the intrinsic reactivity and pore diffusion is already accounted for in parameters A and E . The model can be extended to account for these effects explicitly, see for example [20–22]. The kinetic-diffusion model, as given in Eq. (2), was derived with the assumption that the reaction is first order with respect to the oxidizer ox , see Smith [20] for details. In Fig. 1 the prediction of the kinetic-diffusion model is plotted as a function of temperature for a given condition. The effects of pure chemical kinetics ($R_{dif} = \infty$) and pure diffusion ($R_{kin} = \infty$) are also shown. As can be seen, the chemical reactions are slow at low temperatures and limits the overall reaction rate (Zone I). At high temperatures, the chemical reactions are fast, and the overall reaction rate is limited by the transport of oxidizer to the particle surface (Zone III). Between zones I and III, an intermediate temperature range exists (Zone II) in which both chemical kinetics and diffusion are important in determining the overall reaction rate.

2.2. The effect of mean gas-particle velocity difference

The constant C entering Eq. (3) incorporates all the effects responsible for mass transfer to the particle surface, i.e. the stoichiometry of the reaction, diffusion to the particle surface and the effect of convection. Chen et al. [23] proposed that for the i th reaction

$$C_i = s_i \frac{M_C}{M_i} \frac{\bar{M}}{RT_0^{7/4}} \frac{p_0}{p} \text{Sh}D_{i,0}. \quad (5)$$

This is an extension of a formula derived by Baum et al. [7] for a single oxidation reaction. Here, s_i is the ratio of the stoichiometric coefficients of carbon and reactant (e.g. $s_i = 1$ for $\text{C} + \text{O}_2 \rightarrow \text{CO}_2$; $s_i = 2$ for $2\text{C} + \text{O}_2 \rightarrow 2\text{CO}$), M_C and M_i are the molecular weights of carbon and the reactant of reaction i , respectively, \bar{M} is the mean molecular weight of the gas in the particle boundary layer, Sh is the Sherwood number, D_i is the diffusion coefficient of the gaseous

reactant of reaction i , p is pressure and subscript 0 denotes the reference state. Assuming that the particles can be treated as spheres, the Sherwood number can be determined from the Ranz-Marshall formula [24]

$$\text{Sh} = 2.0 + 0.6\text{Re}_p^{1/2}\text{Sc}^{1/3}, \quad (6)$$

where $\text{Sc} = \nu/D$ is the Schmidt number, and Re_p is the particle Reynolds number defined as

$$\text{Re}_p = \frac{|u_p - u|d_p}{\nu}, \quad (7)$$

where u is the mean gas velocity, u_p is the particle velocity and ν is the kinematic viscosity. It has frequently been argued [20], that for fine pulverized fuel particles the relative particle-gas velocity is small, and thus $\text{Re}_p \rightarrow 0$ and $\text{Sh} \rightarrow 2$. However, the particle Reynolds numbers can become higher for pressurized systems such as entrained-flow gasification reactors [25]. Also, for larger particles, characterized by larger Stokes numbers, the effect can become important as well.

In modelling of dilute, particulate flows, the effect of turbulence on particle dispersion is often included. One of the most frequently used approaches is to apply a stochastic tracking method. In such a case the particle trajectory is computed based on the instantaneous fluid velocity, which is a sum of the mean fluid velocity and its fluctuating component,

$$u' = \zeta \sqrt{2k/3}, \quad (8)$$

where ζ is a normally distributed random number and k is the turbulent kinetic energy. Even though this method may produce realistic particle dispersion, it gives rise to unphysically large relative velocity differences between particle and fluid. Remember that even tracer particles will experience this unphysical relative velocity, even though they in reality will always follow the fluid in which they are embedded. This is because it is the unresolved turbulent eddies that transport the particles. In turn, such an exaggerated relative velocity gives too large Sherwood number and hence too high transport rate of mass between fluid and particle. Therefore, in the following, we use a constant value of the Sherwood number when calculating C from Eq. (5), and include the effect of turbulence by applying a correction factor $\tilde{\alpha}$, as will be explained below.

2.3. The effect of turbulence and particle clustering

In practical systems the burning particle is exposed to rapid gas velocity fluctuations occurring due to turbulence. The turbulent motion can be responsible for considerable increase of oxidizer transport to the particle surface due to the induced velocity difference between the particle and the surrounding fluid, as discussed in the former section. However, the particles can also form clusters due to turbulence, which can lead to local oxidizer depletion and reduction of the reaction rate. These effects were studied by Direct Numerical Simulation in [16–19] and the following model was formulated for the turbulence correction factor

$$\tilde{\alpha} = \frac{\text{Sh}_{\text{mod}}}{2} = \frac{\overline{\text{Sh}}}{2} \underbrace{\frac{B}{B + \text{DaSt}/2}}_{=\alpha_{\text{cluster}}} \quad (9)$$

where $\frac{1}{2}\overline{\text{Sh}}$ is the part corresponding to the effect of the relative velocity between the particles and the fluid, while α_{cluster} is the part that corresponds to clustering. The model parameter B was shown by Haugen et al. [17] to vary with Stokes number as

$$B = 0.08 + \text{St}/3. \quad (10)$$

Apart from the average Sherwood number, $\overline{\text{Sh}}$, two dimensionless numbers enter Eq. (9), namely the Stokes number (St) and the

Damköhler number (Da). They are defined as

$$\text{St} = \tau_p/\tau_L, \quad (11)$$

$$\text{Da} = \tau_L/\tau_c, \quad (12)$$

where τ_p is the particle response time, τ_L is the integral time scale of turbulence and τ_c is the chemical time scale, related to the combustion time. The particle response time is defined by the Stokes time

$$\tau_p = \frac{\rho_p d_p^2}{18\rho\nu}, \quad (13)$$

where ρ_p is the particle (material) density and ρ is the gas density. The integral time scale can be written as

$$\tau_L = \frac{2k}{3\varepsilon} \quad (14)$$

and the chemical time scale is defined as

$$1/\tau_c = n_p A_p \frac{\overline{\text{Sh}}}{D} d_p, \quad (15)$$

where $A_p = \pi d_p^2$ is the particle external surface area and

$$n_p = \frac{6\rho_s}{\rho_p \pi d_p^3} \quad (16)$$

is the particle number density with ρ_s being the solids density in the mixture. Please note that ρ_p is the material (or apparent) density of the particle, which is very different from the solid density in the mixture, ρ_s . For example, the solid density of char in air at 1000 K and stoichiometric conditions is around 0.03 kg/m³. This corresponds to nearly one hundred 100 μm -sized char particles per cubic centimeter for char particles with an apparent density of 600 kg/m³.

In the following, the physical reasoning on which Eq. (9) was derived will be described. If the lifetime of a particle cluster (τ_{cluster}) is short relative to the chemical time scale (τ_c), the reactant concentration can be assumed to be uniform across the cluster and equal to the concentration outside the cluster. In this case, the relevant reactant consumption rate is given by Eq. (15), which is valid for homogeneous distributions of particles and reactant. For clusters with long lifetimes compared to the chemical time scale, the reactant concentration inside the cluster is reduced. This means that the overall consumption rate becomes dependent on cluster characteristics, such as cluster dimension and particle number density. The resulting reactant consumption rate (r) is therefore limited both by the rate due to Eq. (15) ($r_{\text{uniform}} = 1/\tau_c$) and the cluster-characteristic rate ($r_{\text{cluster}} = 1/\tau_{\text{cluster}}$). This means that the reactant consumption rate, which equals the mass transfer rate, can be written as:

$$r = \frac{r_{\text{uniform}} r_{\text{cluster}}}{r_{\text{uniform}} + r_{\text{cluster}}}. \quad (17)$$

Therefore, when the above formulation is normalized using the reactant consumption rate from Eq. (15) with $\overline{\text{Sh}} = 2$, denoted as $r_{\text{uniform}, \overline{\text{Sh}}=2}$, one obtains a factor by which the mass transfer rate is altered relative to the rate typically used in RANS simulations:

$$\tilde{\alpha} = \left(\frac{r_{\text{uniform}} r_{\text{cluster}}}{r_{\text{uniform}} + r_{\text{cluster}}} \right) / r_{\text{uniform}, \overline{\text{Sh}}=2}. \quad (18)$$

Using Eqs. (12) and (15), and after some rearranging, Eq. (9) can be recovered with $B = r_{\text{cluster}} \tau_L \text{St}/2 = r_{\text{cluster}} \tau_p/2$. Since r_{cluster} is unknown, an approximate expression for the parameter B was found using DNS (see Eq. (10)). The details on the fitting procedure are given in [17].

Previous studies [16,17] showed that the intensified transport of oxidizer towards the particle surface is the dominating effect of

turbulence at relatively low Da. However, as the Damköhler number gets larger, the impeded reactant transport associated with the particle clustering becomes the major phenomenon controlling the overall surface reaction rate. It was also found that the effect of clustering is strongest when the Stokes number is of the order of unity. The reason for that is that such conditions (i.e. similar magnitudes of particle and flow time scales) are the most conducive to the formation of relatively long-lived clusters. (It is well known that particle clusters at the Kolmogorov scale, which are due to particles with Kolmogorov based Stokes numbers around unity, are the strongest and sharpest, but these clusters typically have too short lifetimes to have any relevance for the reactant transport.)

The Sherwood number \overline{Sh} entering Eq. (9) can still be determined from Eq. (6), however, the particle Reynolds number should now be calculated as

$$Re_p = \frac{u_{rel} d_p}{\nu} \quad (19)$$

such that the effect of turbulent velocity fluctuations is taken into account through the relative velocity, u_{rel} . Based on physical arguments, Haugen et al. [17] proposed the following expression for the average relative velocity difference caused by the turbulence:

$$u_{rel} = \beta u_{rms} \sqrt{\frac{St k_L^{-2/3} - k_\eta^{-2/3}}{k_L^{-2/3} - k_\eta^{-2/3}}}, \quad (20)$$

where $\beta = 0.41$ is a model constant, k_L and k_η are the integral and Kolmogorov scale wavenumbers, respectively. The wave numbers can be linked to the turbulent kinetic energy k , its dissipation rate ε , and kinematic viscosity ν as

$$k_L = 2\pi \varepsilon \left(\frac{3}{2k}\right)^{3/2} \quad (21)$$

$$k_\eta = 2\pi \left(\frac{\varepsilon}{\nu^3}\right)^{1/4}. \quad (22)$$

The main assumption behind Eq. (20) is that the relative velocity is induced only by those turbulent eddies that have turnover times, τ_{eddy} , that are shorter than the particle response time, τ_p . In this way, the relative velocity is proportional to the square root of the kinetic energy ($E(k)$) of the corresponding eddies, such that:

$$u_{rel} \sim \left(\int_{k_\eta}^{k_{eddy}} E(k) dk\right)^{1/2} \sim \left(\int_{k_\eta}^{k_{eddy}} \varepsilon^{2/3} k^{-5/3} dk\right)^{1/2} \quad (23)$$

where $k_{eddy} = 2\pi / \tau_{eddy} u_{eddy}$. Furthermore, Kolmogorov scaling for the inertial sub-range was assumed in order to relate k_{eddy} with k_L , while the model constant, β , was obtained by fitting the model with a large variation of highly accurate direct numerical simulations. It should be mentioned that for very small Stokes numbers the numerator of Eq. (20) might become negative. However, at these conditions no significant relative velocity between particles and fluid can exist. Therefore, if this is the case, we assume that $u_{rel} = 0$. This will result in a tiny discontinuities in the model prediction that will be visible in figures presented in Section 3.2.

By calculating the particle Reynolds number based on the relative velocity obtained from Eq. (20), the Ranz-Marshall model (see Eq. (6)) can now be used to find the average Sherwood number, \overline{Sh} . As can be seen from Eqs. (19) and (20), the Sherwood number \overline{Sh} is affected by the turbulence only. The reaction rate due to diffusion given by Eq. (3) can now be modified to take into account the effect of turbulence and particle clustering as

$$R_{dif} = \tilde{\alpha} \frac{C}{d_p} \left(\frac{T + T_p}{2}\right)^{3/4}. \quad (24)$$

The model can therefore incorporate the effect of mean gas-particle velocity through Eqs. (5)–(7), as well as the effect of turbulence and particle clustering through Eqs. (9)–(15). As mentioned

Table 1

The value of γ_{st} for some mixtures.

Mixture	Reaction	γ_{st}
Char particles in air	$C + O_2 \rightarrow CO_2$	11.4
Char particles in 100% CO_2	$C + CO_2 \rightarrow 2CO$	3.7
Char particles in 100% O_2	$C + O_2 \rightarrow CO_2$	2.7
Char particles in steam	$C + H_2O \rightarrow CO + H_2$	1.5
Ilmenite particles in air	$4FeTiO_3 + O_2 \rightarrow 4TiO_2 + 2Fe_2O_3$	0.225

above, care should be taken when applying Eqs. (5)–(7) with the stochastic tracking method. It should also be stressed that Eqs. (9)–(15) are suitable to be applied in RANS models, and their form allows to determine all the required variables during the simulation. In this study, the model was implemented into ANSYS Fluent by means of a User Defined Function (UDF) mechanism. The UDF is provided as a supplementary file to this paper.

3. Model sensitivity

In this section, numerical examples are presented in which the model applicability and the influence of the main model parameters is presented. The first two examples are just general calculations, while the last one is a simplified CFD simulation. This enables us to examine the potential conditions in which the effect of turbulence can be significant in practical systems.

3.1. Numerical example 1

Eq. (11) can be re-organized to yield the following expression for the integral time scale:

$$\tau_L = \frac{\rho_p d_p^2}{18 \rho \nu St}. \quad (25)$$

The Damköhler number is then given as

$$Da = \frac{\tau_L}{\tau_c} = \frac{\tau_L 2Dn_p A_p}{d_p} = \frac{\rho_p d_p^2 2Dn_p A_p}{18 \rho \nu St d_p}, \quad (26)$$

where, for the considerations in this section, it has been assumed that $\overline{Sh} = 2$. Furthermore, the solids density in the domain can be expressed as

$$\rho_s = \rho_g / \gamma_{st}, \quad (27)$$

where ρ_g is the gas density in the gas-solid mixture and γ_{st} is the stoichiometric air-fuel ratio. The value of γ_{st} for some mixtures is given in Table 1. Apart from char-based mixtures, ilmenite was also included due to its possible application since the ilmenite particles can serve as oxygen carriers in Chemical Looping Combustion. The particle number density can now be expressed as

$$n_p = \frac{6\rho_g}{\pi d_p^3 \rho_p \gamma_{st}}. \quad (28)$$

The intrinsic density of the gas, ρ , is, however, almost the same as the gaseous density of the mixture, ρ_g , as long as the solid volume fraction is low. From the above, and by using that $A_p = \pi d_p^2$, it can be shown that

$$Da = \frac{\rho_p d_p^2 12D \rho_g \pi d_p^2}{18 \rho \nu St \pi d_p^3 \rho_p \gamma_{st} d_p} = \frac{2\rho_g}{3ScSt\gamma_{st}\rho} \approx \frac{2}{3ScSt\gamma_{st}}. \quad (29)$$

In Fig. 2, the Damköhler number, as calculated from Eq. (29), is shown as a function of Stokes number for the same cases as listed in Table 1. Clustering is expected to slow down the reactions for Damköhler numbers around or greater than unity [17]. From Fig. 2, it can be seen that for carbon oxidation in air the Damköhler number is larger than unity only for Stokes numbers smaller than 0.1.

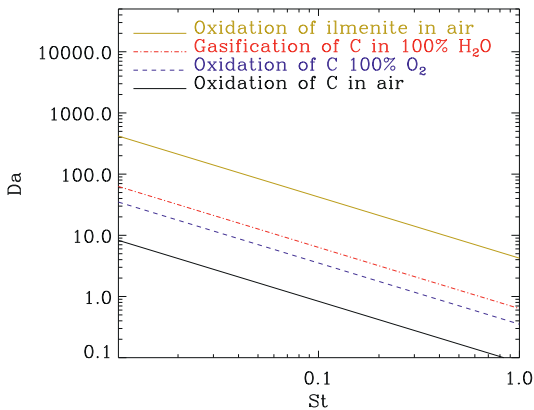


Fig. 2. Damköhler number at stoichiometric conditions as a function of Stokes number for the cases listed in Table 1. Here, the Schmidt number is set to $Sc = 0.7$.

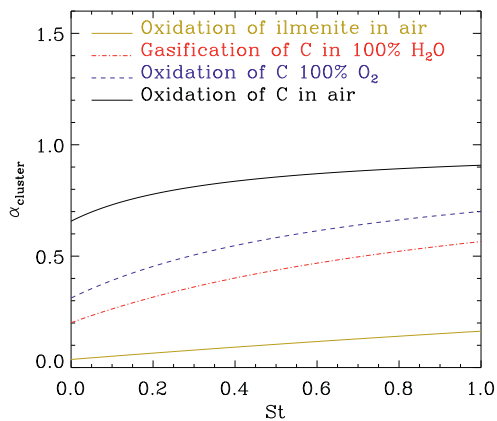


Fig. 3. Effect of clustering ($\alpha_{cluster}$) as a function of Stokes number for the cases listed in Table 1.

For oxidation of ilmenite in air, however, the Damköhler number is above 4 even for Stokes number as large as one. Using Eqs. (10) and (29) the part due to clustering can be expressed as

$$\alpha_{cluster} = \frac{B}{B + DaSt/2} = \frac{0.08 + St/3}{0.08 + St/3 + 1/(3Sc\gamma_{st})}. \quad (30)$$

The value of $\alpha_{cluster}$ as a function of Stokes number is shown in Fig. 3, from which it is clear that the potential to reduce the reaction rate highly depends on the composition of the mixture. At stoichiometric conditions the reaction rate due to clustering can be reduced up to 35% in the case of char combustion in air, while for char combustion in pure O_2 or H_2O the effect of clustering can be twice as large. Finally, for oxidation of ilmenite in air, the reduction due to clustering is dramatic.

3.2. Numerical example 2

In this example we discuss the influence of selected model parameters on $\bar{\alpha}$. The magnitudes of the studied parameters and other essential model parameters are presented in Table 2. They were selected such that they reflect, to some extent, conditions typically found in industrial scale facilities (reactors and combustion chambers). The required turbulence parameters, as would be known in a RANS simulation, were estimated.

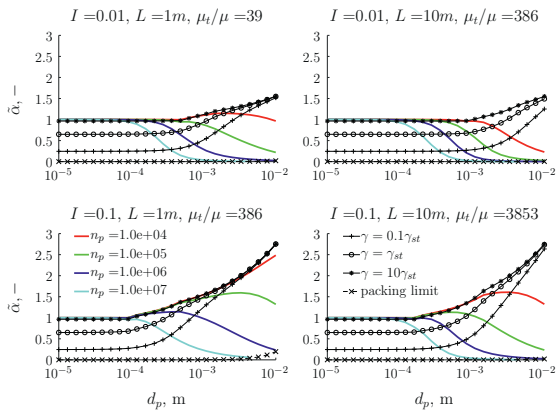


Fig. 4. The influence of parameters from Table 2 on $\bar{\alpha}$ for char particles in air ($\rho_p = 800 \text{ kg/m}^3$, $\gamma_{st} = 11.4$). The legend included in the bottom panels apply to the entire figure.

Table 2
Studied model input parameters.

Name	Symbol	Unit	Value
Mean gas velocity	u	m/s	10
Turbulence intensity	I	-	$10^{-2}; 10^{-1}$
Domain length scale	L	m	1; 10
Particle number density	n_p	m^{-3}	$10^4 - 10^7$
Gas density	ρ	kg/m^3	0.35
Gas kinematic viscosity	ν	m^2/s	10^{-4}
Diffusion coefficient	D	m^2/s	10^{-4}
Particle (material) density	ρ_p	kg/m^3	800

In order to calculate the turbulence kinetic energy k and its dissipation ε the following expressions were used

$$u_{rms} = ul, \quad (31)$$

$$k = \frac{3}{2} u_{rms}^2, \quad (32)$$

$$\varepsilon = C_\mu^{3/4} \frac{k^{3/2}}{l}, \quad (33)$$

where l is the integral length scale, approximated as $l = 0.07L$ [26], and $C_\mu = 0.09$ [27]. It should be noted that by using such a definition of l for large systems, the integral length scale is likely to be overestimated, which in turn leads to unrealistically high turbulent viscosity since

$$\mu_t = \rho C_\mu \frac{k^2}{\varepsilon} = \rho C_\mu^{1/4} k^{1/2} l. \quad (34)$$

Nevertheless, in the absence of problem-specific details, we stick to the above estimation.

The particle time scale τ_p , the time scale of the integral scale eddies τ_L and the chemical time scale τ_c are calculated from Eqs. (13)–(15), respectively. These time scales are then used to calculate St and Da , and the mean Sherwood number Sh is calculated using Eqs. (19)–(22) together with Eq. (6). The results, in the form of $\bar{\alpha}(d_p)$ for selected particle number densities, are presented in Fig. 4 for the case of char particles in air. In the two upper panels, cases with low turbulence intensity ($I = 1\%$) are presented, whereas for the lower panels $I = 10\%$. Furthermore, the results shown in the left-hand side panels differ from those on the right side by the turbulence length scale, as stated in the title of the figure. There are four black lines in Fig. 4. The line with circle-shaped markers divides the figure into regions of rich (below the

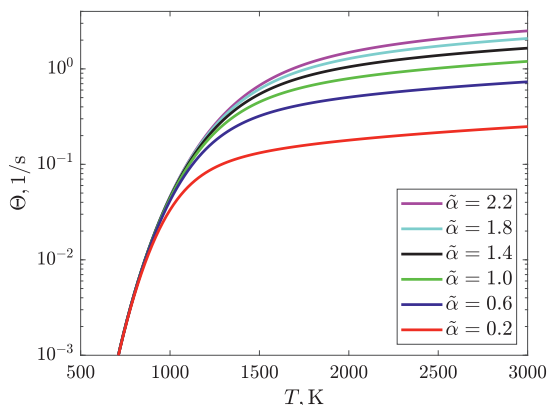


Fig. 5. The influence of $\tilde{\alpha}$ on the reactant consumption rate for $\rho_p = 800 \text{ kg/m}^3$, $d_p = 500 \text{ }\mu\text{m}$, $A = 0.002 \text{ s/m}$, $E = 79 \text{ kJ/mol}$, $C = 5 \cdot 10^{-12} \text{ sK}^{-3/4}$.

line) and lean (above the line) conditions, while the line with x-shaped markers corresponds to the packing limit of particles, i.e. the maximum volume fraction of the particles. For spherical particles, the volume fraction at the packing limit is assumed to be equal to 0.63, which is a typical limit for randomly packed, spherical particles of the same size. The remaining two lines encompass the region inside which the air-fuel ratio, γ , is between 0.1 and 10. It is expected that conditions in real systems correspond to the region limited by these two lines. Details regarding the derivation of the packing limit line and the stoichiometric line can be found in Appendix A.

From Fig. 4 it is clear that for the range of examined particle number densities, the turbulence do not have any effect on the mass transfer if the particles are too small. This is because particles for which $\tau_p \ll \tau_\eta$ immediately follow the motion of the fluid, so it is not possible for them to form clusters or for the turbulence to enhance the mass transfer due to any relative velocity between fluid and particle. (Please note that for d_p of the order of $10^{-5} - 10^{-4}$ Eq. (20) yields negative number inside the square root and in this region $u_{rel} = 0$ was assumed.) For larger particles, which have longer response times, both effects of turbulence can be observed. The largest mass transfer enhancement is, as expected, observed for the high turbulence intensity cases (lower panels of Fig. 4), in which $\tilde{\alpha}$ becomes greater than 1 if the particle number density is sufficiently low. For all cases above a certain n_p , the effect of particle clustering becomes dominant ($\tilde{\alpha} < 1$). This decrease in the reactant transfer rate is particularly strong for the low turbulence intensity cases (upper panels of Fig. 4) and it is more intense in larger facilities (right panels). It is also worth noticing that both scenarios are probable around the stoichiometric conditions, i.e. we can expect both effects of turbulence to be observed in real systems.

Finally, the influence of $\tilde{\alpha}$ on the reactant consumption rate Θ , as given by Eq. (2) in which R_{diff} is found from Eq. (24), is presented in Fig. 5 as a function of temperature. Resorting also to the results shown in Fig. 4, a factor of 2 enhancement of reaction rate due to turbulence ($\tilde{\alpha} > 1$) can be expected at favorable flow conditions and high temperatures. The reduction of the rate ($\tilde{\alpha} < 1$) can potentially be much stronger. In the following, we will investigate how $\tilde{\alpha}$ may vary in more realistic applications.

3.3. Numerical example 3

In order to visualize and quantify the effect of turbulence on pulverized char conversion, a simplified CFD model was developed.

Table 3
Stoichiometric coefficients for reaction (36) and volatiles composition.

	$C_k H_l O_m N_n S_o$	ν_i	
k	1.034	O_2	1.258
l	2.682	CO	1.034
m	0.899	H_2O	1.341
n	0.0274	SO_2	0.0034
o	0.0034	N_2	0.0137

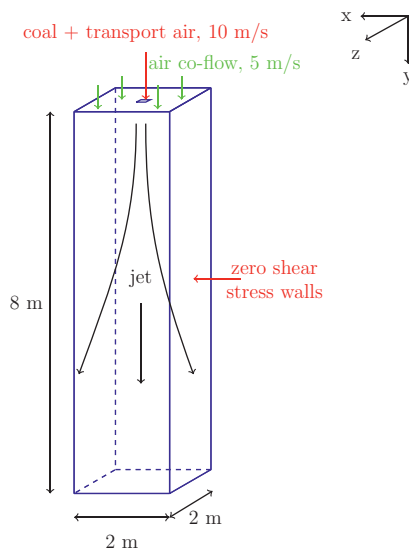
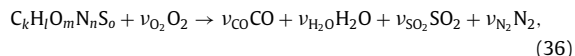


Fig. 6. Schematics of the geometry and boundary conditions.

The geometry of the model was selected to be a $2\text{ m} \times 2\text{ m} \times 8\text{ m}$ cuboid to which coal particles are introduced through a square ($4\text{ cm} \times 4\text{ cm}$) inlet together with a co-flowing hot air. Inside the domain the particles form a jet and undergo devolatilization and char combustion. The main features of the numerical approach are as follows. The Navier-Stokes equations are solved in a steady-state and incompressible form, turbulence is modelled using the standard $k - \varepsilon$ model, radiation is accounted for with the Discrete Ordinates model and the particles are tracked in a Lagrangian reference frame. For simplicity, and since the focus of the paper is on char conversion, the devolatilization rate is assumed constant ($=50 \text{ 1/s}$). A single surface reaction is considered:



where the corresponding Arrhenius parameters are $A = 0.002 \text{ s/m}$, $E = 7.9 \cdot 10^7 \text{ J/kmol}$ and the diffusion constant from Eq. (3) is given by $C = 5 \cdot 10^{-12} \text{ s/K}^{-3/4}$, while the combustion rate of volatiles is computed using the Finite-Rate/Eddy-Dissipation model, according to the reaction:



where the stoichiometric coefficients ν_i and the composition of the fictitious volatiles species $C_k H_l O_m N_n S_o$ are given in Table 3. A schematic representation of the geometry and boundary conditions are given in Fig. 6, coal properties are given in Table 4, and the main model parameters are presented in Table 5. The selection of this particular configuration was motivated by the fact that it reflects typical conditions for fuel supply to the combustion cham-

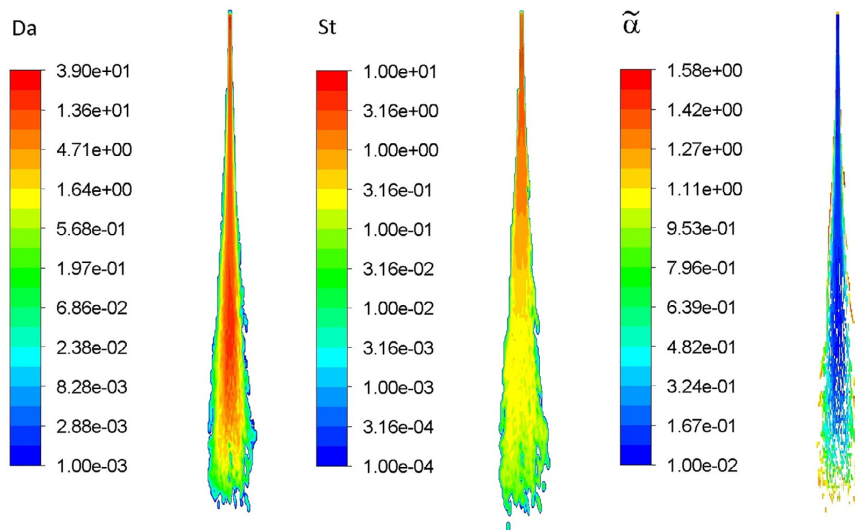


Fig. 7. Distribution of Da, St and $\tilde{\alpha}$ inside the jet.

Table 4

Coal properties.

Proximate analysis		Ultimate analysis (daf)	
Moisture	0.107	C	0.674
Volatiles	0.446	H	0.05
Fixed carbon	0.357	O	0.267
Ash	0.09	N	0.007
HCV (AR)	22.5 MJ/kg	S	0.002

Table 5

CFD model input parameters.

Name	Symbol	Unit	Value
Coal mass flow rate	m_f	kg/s	$1.5 \cdot 10^{-2}$
Transport air mass flow rate	$m_{air,1}$	kg/s	0.0056
Transport air temperature	$T_{air,1}$	K	1000
Coflow air mass flow rate	$m_{air,2}$	kg/s	7.0
Coflow air temperature	$T_{air,2}$	K	1000
Turbulence intensity	I	–	10^{-2}
Viscosity ratio	μ_t/μ	–	50
Coal (material) density	ρ_p	kg/m ³	1400
Coal particle diameter	d_p	m	$2.5 \cdot 10^{-4}$

ber. Moreover, the input parameters are chosen such that this setup corresponds (to a certain degree) to the upper, left-hand side panel of Fig. 4, which means that the turbulence is most likely to reduce the mass transfer rate. The right panel of Fig. 7 shows the distribution of $\tilde{\alpha}$ in a cross section inside the jet. Please note that: 1) no interpolation (no smoothing between cell values) is used to produce contours of $\tilde{\alpha}$ in order to avoid a false impression of low $\tilde{\alpha}$ at the edges of the jet; 2) only regions with burning particles are displayed. From the figure it can be seen that, for the configuration considered, the effect of clustering is significant. In fact, $\tilde{\alpha}$ is of the order of 10^{-1} for the most part of the jet. An intensification in the mass transfer is predicted only at the edges of the jet, where the particle number density is lower and the turbulence intensity is highest. The reason the effect of turbulence is so strong can be understood by inspecting the Damköhler and Stokes numbers inside the jet. These two dimensionless numbers are shown in the left and middle panels of Fig. 7. Even though St decreases by 2–3

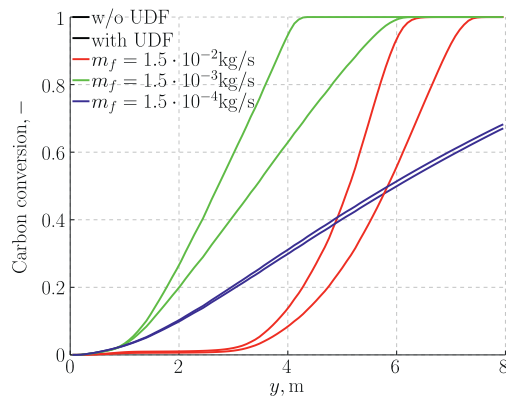


Fig. 8. Char conversion as a function of distance from the inlet - effect of fuel mass flow rate (in all cases $d_p = 2.5 \cdot 10^{-4}$ m).

orders of magnitude along the particle jet, Da remains sufficiently high (of the order of 1) in the entire volume of the jet to yield $\tilde{\alpha} < 1$. It should also be noted that, based on Fig. 4, for $\tilde{\alpha}$ to decrease below 0.5 the local conditions must correspond to very rich mixture. For the case we study here, a relatively high fuel mass flow rate ($m_f = 1.5 \cdot 10^{-2}$ kg/s) was chosen to obtain such conditions but in reality the existence of large volumes with rich mixture is rather unlikely and mostly restricted to regions next to the fuel supply. Therefore, in the following we attempt to verify if the effect of turbulence still remains significant for lower fuel mass flow rates.

In Fig. 8 char conversion along the jet for three different fuel mass flow rates is presented. For each mass flow rate, two cases are shown. In the first, the baseline case, the effect of turbulence was not accounted for in the numerical model. In the second case, the effect of turbulence was introduced through the User Defined Function (UDF). This was done by modifying the reaction rate due to diffusion according to Eqs. (9), (10) and (24). In order to produce

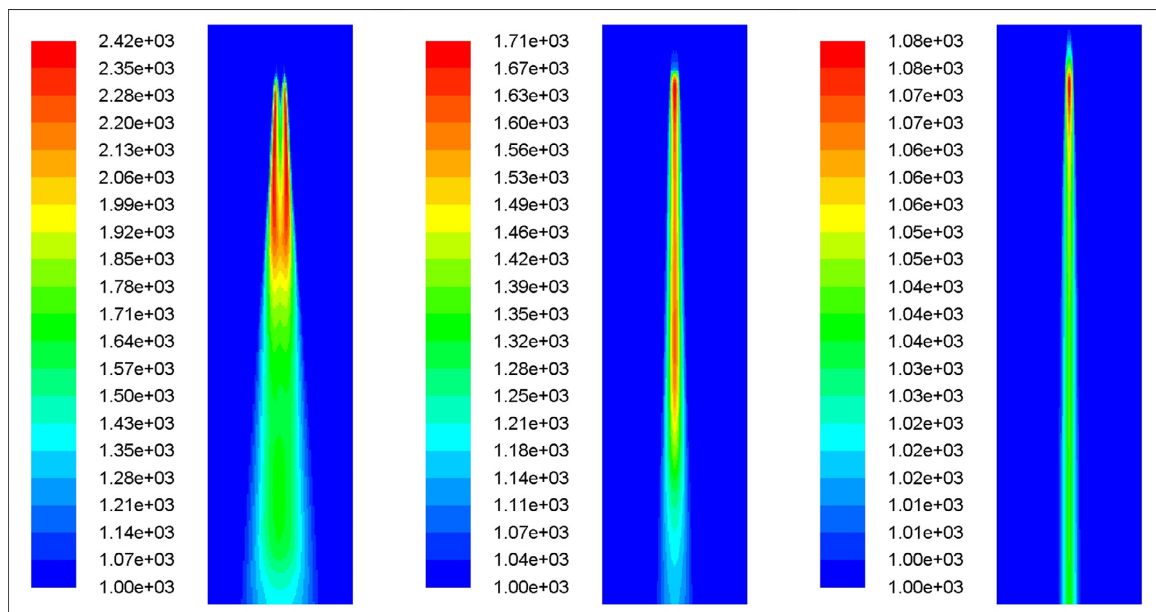


Fig. 9. Contours of temperature (in K) inside the particle jet, from left to right: $m_f = 1.5 \cdot 10^{-2}$ kg/s, $m_f = 1.5 \cdot 10^{-3}$ kg/s and $m_f = 1.5 \cdot 10^{-4}$ kg/s.

Fig. 8 the domain was divided into N segments along its height. For each such segment an average carbon conversion (\bar{X}) was computed for particles within the given section as

$$\bar{X} = \frac{1}{n_{part}} \sum_{i=1}^{n_{part}} X_i = \frac{1}{n_{part}} \sum_{i=1}^{n_{part}} \left(1 - \frac{m_c}{m_{c,0}} \right). \quad (37)$$

In the above, n_{part} is the number of particles passing through the given segment, m_c and $m_{c,0}$ are the current and initial particle char masses, respectively. The selected fuel mass flow rates can be thought of as rich ($m_f = 1.5 \cdot 10^{-2}$ kg/s), around-stoichiometric ($m_f = 1.5 \cdot 10^{-3}$ kg/s) and lean ($m_f = 1.5 \cdot 10^{-4}$ kg/s) mixtures, although we deliberately do not provide the exact magnitudes of air-fuel ratio (γ) as it varies significantly from cell to cell. It can be seen that turbulence has only a very weak positive effect on the conversion rate if the mass flow rate is very low or, in other words, if $\gamma \gg \gamma_{st}$. The reason for that is a very low particle number density, and hence low Damköhler number. In regions with low Da, no dense clusters can be formed, so there is no reduction of the reaction rate due to clustering, but a weak increase due to turbulence ($\tilde{\alpha} > 1$). This behavior is also in agreement with the results presented in Fig. 4. In the cases with higher fuel mass flow rates in Fig. 8 (red and green lines), the particle number densities in the core of the jet are much higher, and a strong effect due to particle clustering can be observed as the conversion is much slower in the cases where the reaction rate is modified by the UDF. The conversion profiles are similar in both cases, but the conversion begins further downstream for the case with the highest mass flow rate.

It should be stressed that the results presented in Fig. 8 are strongly affected by the temperature. Even though the same boundary conditions were used, the cases with lower fuel mass flow rates are characterized by lower temperatures in the system due to the smaller amounts of released and burned volatiles. This is confirmed in Fig. 9, where the contours of temperature are presented. The consequence of higher temperature is higher reaction rate. This can be observed by comparing the slopes of the conversion profiles in Fig. 8, i.e. the higher the mass flow rate, the

steeper the slope. At the same time, as the temperature increases, the diffusion rate becomes more important in the overall reaction rate, and thus the observed effect of turbulence is stronger. The difference in the reaction rates is more clearly visible in Fig. 10, which shows contours of the relative rate difference, defined as $(\Theta - \Theta_0)/\Theta_0$, where Θ is the modified rate including the effect of turbulence, and Θ_0 is the unmodified rate. The highest relative rate difference is observed for the highest mass flow rate, and it is smaller for the lower flow rate. It can be seen that the differences occur mostly in the core of the jet, where the particle number density, and hence the Damköhler number, are the highest, and thus the rate is considerably reduced. However, also regions of increased reaction rate are observed further away from the jet core. For the smallest mass flow rate the relative rate difference is not reduced in the center of the jet. Instead a slightly increased reaction rate can be observed at the jet outskirts, where the turbulence is strongest and the particle number density is quite low. Based on the results discussed above, we can conclude that the effect of particle clustering can be significant for a quite wide range of fuel mass flow rates or, in other words, for a wide range of stoichiometric conditions.

Another important parameter that influences how strong the effect of turbulence is, is the particle size. We examine this parameter by changing the particle diameter, but keeping the mass flow rate constant and equal to $1.5 \cdot 10^{-3}$ kg/s, corresponding to roughly stoichiometric conditions, for all cases. The particle sizes were chosen such that the particle number density n_p is decreasing by a factor of 10 as the particle diameter increases ($n_p \sim d_p^{-3}$). As can be seen in Fig. 11, for the smallest particles (red lines) the effect of turbulence amounts to essentially no difference when the total conversion is considered (i.e. the distance from the inlet to the point at which full conversion is reached). On the other hand, the local reduction of the conversion rate is actually of the same magnitude for all particle sizes. The reason the decreased reaction rate does not affect the total conversion time for the smallest particles is depletion of the available oxygen, seen as a flattening of the

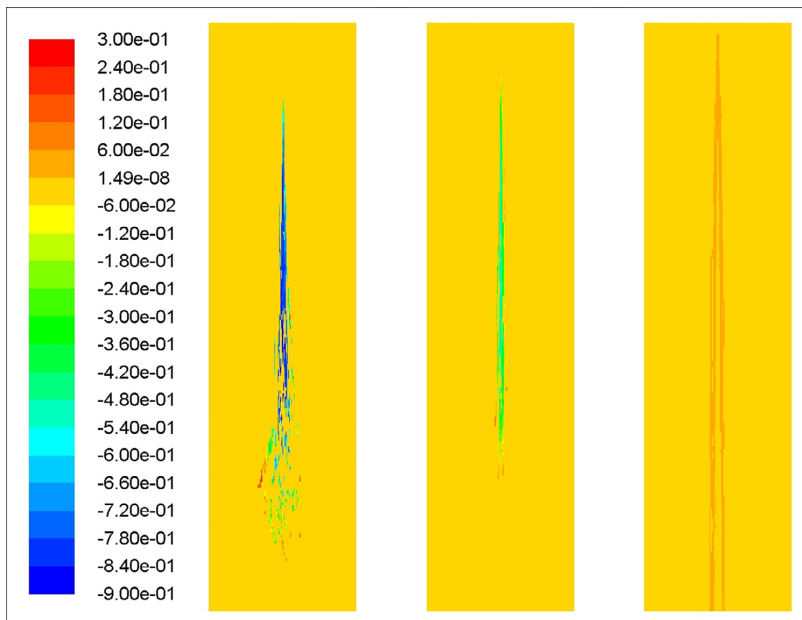


Fig. 10. Contours of relative rate differences $(\Theta - \Theta_0)/\Theta_0$ inside the particle jet, from left to right: $m_f = 1.5 \cdot 10^{-2}$ kg/s, $m_f = 1.5 \cdot 10^{-3}$ kg/s and $m_f = 1.5 \cdot 10^{-4}$ kg/s.

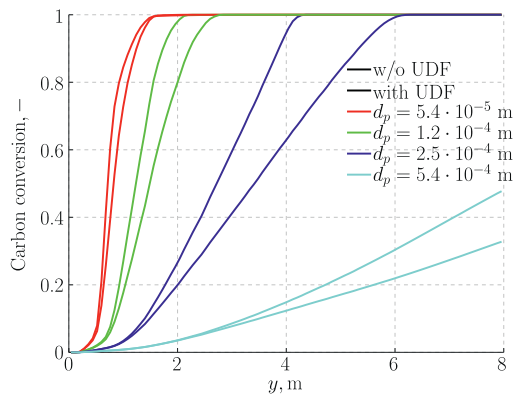


Fig. 11. Char conversion as a function of distance from the inlet – effect of particle diameter (in all cases $m_f = 1.5 \cdot 10^{-3}$ kg/s).

'without UDF' profile at the final stage of conversion. As the particle size becomes larger, particles travel further downstream before they reach a complete burnout. This is because these larger particles are less affected by fluid motions. Also, on average, they burn in lower temperatures as they still undergo conversion long after they have passed the regions of highest temperature, i.e. regions of volatile burning. For these larger particles, the effect of turbulence is more pronounced, e.g. particles with $d_p = 2.5 \cdot 10^{-4}$ m (dark blue lines) need to travel around 50% longer to reach complete burnout when the effect of turbulence is accounted for. This is opposite to what can be expected based on Fig. 4, since for a given stoichiometric condition $\tilde{\alpha}$ increases for larger particle sizes. Nevertheless, the degree to which the conversion rate is reduced depends not only on $\tilde{\alpha}$ but also on the relative magnitudes of R_{kin} and R_{dif} . As the particle diameter increases the conversion rate be-

comes more diffusion-controlled since $R_{dif} \sim 1/d_p$ (see Eq. (3)). At the same time, the rate due to kinetics varies only slightly. The resulting shift towards diffusion-controlled regime outweighs the effect of higher $\tilde{\alpha}$ and leads to the conversion rate being reduced by the same amount, irrespective of the particle size. Finally, it should be noted that for even larger particles, at some point $\tilde{\alpha} \geq 1$ (see Fig. 4), such that no reduction in the conversion rate due to clustering will be possible, even for a fully diffusion-controlled reaction. This was observed for particles with $d_p \sim 1 \cdot 10^{-3}$ m but was not shown in Fig. 11 due to much longer time scale required to reach even a fractional burnout.

The degree to which the turbulence influences the surface reaction rate might also depend on the characteristics of the turbulence itself, such as turbulence intensity or the viscosity ratio, μ_t/μ , as they are linked to turbulence kinetic energy and its dissipation. These two parameters can affect the integral time scale, and thus, the Damköhler and Stokes numbers. Their influence is shown in Fig. 12 from which it can be seen that the conversion rate is affected in almost exactly the same way for all parameter combinations that we study. The only difference is that a sufficiently strong turbulence causes the particles to be converted slightly faster as a result of enhanced mixing.

Finally, we observed that the effect of clustering weakens if the jet velocity (velocity at which the transport air and particles are introduced) is increased, as shown in Fig. 13. This is due to the Damköhler number being reduced as the jet velocity increases. At even higher jet velocity, the only effect of turbulence would be to increase the conversion rate as a result of enhanced mass transfer to the particle surface.

4. Application to an industrial scale boiler

In the previous section we explored potential conditions in which turbulence can enhance or decrease the surface reactions through the mass transfer rate. As shown by Haugen et al. [17] these conditions can be reduced to only two dimension-

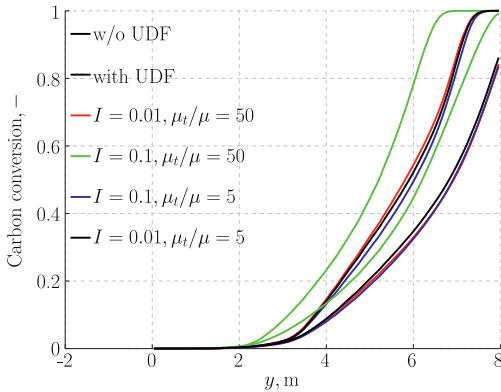


Fig. 12. Char conversion as a function of distance from the inlet – effect of inlet turbulence ($d_p = 2.5 \cdot 10^{-4}$ m, $m_f = 1.5 \cdot 10^{-2}$ kg/s, $T_{air} = 600$ K).

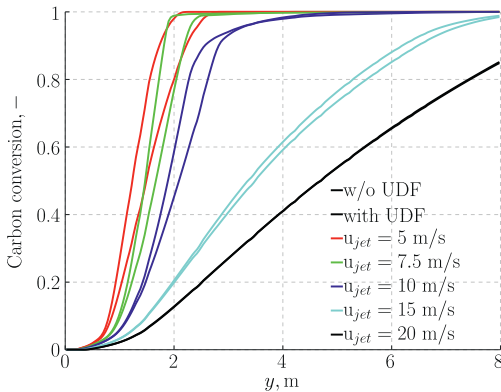


Fig. 13. Char conversion as a function of distance from the inlet – effect of jet inlet velocity ($d_p = 1.2 \cdot 10^{-4}$ m, $m_f = 1.5 \cdot 10^{-3}$ kg/s)

less numbers, the Stokes number and the Damköhler number. This implies that, in theory, one should be able to predict the effect of turbulence on the mass transfer rate in practical systems, such as large scale boilers, by a simple estimation of Da and St characterizing the given system. This is however not so straight forward since one has to deal with a certain range of these two parameters, often varying by several orders of magnitude. Thus, in order to verify how our theoretical considerations translate into reality, we examine a real-scale industrial boiler OP-430. This is a middle size boiler fired with a pulverized coal and producing 430 tones of steam per hour (at 532 °C, 12.7 MPa). Tangential firing is applied in the boiler, i.e. the burners are located in each of four corners of the furnace. A detailed description of the boiler geometry and operating conditions can be found in Adamczyk et al. [28]. A similar numerical approach to that described in Section 3.3 is utilized here, the main differences being: 1) lower devolatilization rate (=13 1/s), 2) slightly more accurate chemistry and 3) a different coal type. The considered reactions are:



Table 6
Stoichiometric coefficients for reaction (36) and volatiles composition.

$C_kH_lO_mN_nS_o$	ν_j		
k	1.19	O ₂	1.54
l	4.41	CO	1.35
m	0.58	H ₂ O	2.17
n	0.068	SO ₂	0.018
o	0.0027	N ₂	0.040

Table 7
Coal properties.

Proximate analysis		Ultimate analysis (daf)	
Moisture	0.022	C	0.803
Volatiles	0.290	H	0.056
Fixed carbon	0.48	O	0.118
Ash	0.208	N	0.012
HCV (AR)	24.7 MJ/kg	S	0.011

Table 8
Kinetic parameters for reactions (38) and (39).

Reaction	A	E [J/kmol]	C [s/K ^{-3/4}]
(38)	0.001	$7.9 \cdot 10^7$	$5 \cdot 10^{-12}$
(39)	$2.239 \cdot 10^{12}$	$1.7 \cdot 10^8$	-

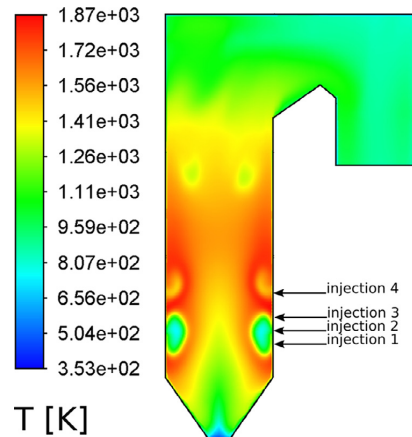


Fig. 14. Contours of temperature in the boiler central cross section. Arrows indicate elevations of fuel injection ports.

and the combustion of volatiles follow reaction (36) with the coefficients given in Table 6. The coal properties are listed in Table 7 and kinetic parameters given in Table 8.

In order to observe any effect of turbulence on the overall reaction rate it is required that the conditions inside the boiler correspond to zones II or III conversion. Otherwise, the conversion rate is fully limited by the reaction kinetics and the turbulence-affected mass transfer rate will have no influence on the process. Conditions in zones II and III are characterized by relatively high temperatures. Figure 14 shows the temperature distribution in the boiler central cross section. Four elevations at which coal is injected are also shown and marked with arrows. The pockets of low temperature located symmetrically close to the walls coincide with coal and air injections (pockets in the lower part) and overfire air ports (pockets in the upper part). The highest temperature can be observed around the particle injections and in the central part of the

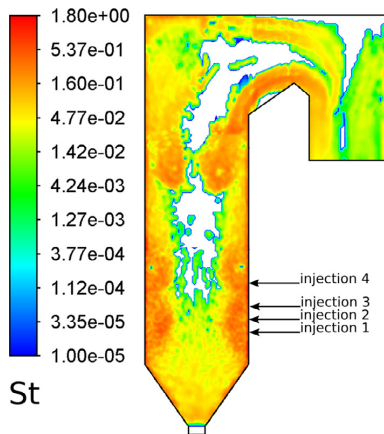


Fig. 15. Contours of the Stokes number. Arrows indicate elevations of fuel injection ports.

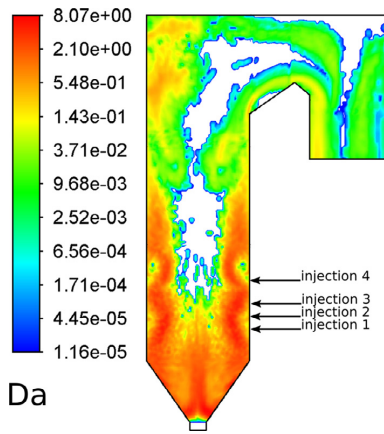


Fig. 16. Contours of the Damköhler number. Arrows indicate elevations of fuel injection ports.

boiler. These are the regions in which we can expect the conversion rate to be influenced by the turbulence.

The distribution of the Stokes and Damköhler numbers in the boiler cross section is shown in Figs. 15 and 16, respectively. In both figures, white zones in the central part correspond to regions in which there are no particles undergoing char combustion. The much higher density of particles in the vicinity of the boiler walls is caused by the specific design of injections, i.e. the particles are injected from the corners in a way that induces a spiraling motion (see Fig. 17, which shows pathlines in the injection area and locations at which the coal is injected). It can be seen that close to the walls in the lower part of the boiler both Da and St are relatively high. These conditions are favorable to particle clustering, thus, it is expected that the conversion process will slow down in these regions. This is in agreement with Fig. 18 which shows that $\tilde{\alpha}$ for these areas can be significantly less than one. On the other hand, in the upper part of the boiler, the Damköhler number is much lower. This is because of the particle number density, which is lower by around 2–3 orders of magnitude. In such regions the only effect turbulence can have is to intensify the reactant transport towards the particle surface, which is equivalent to saying that $\tilde{\alpha} > 1$, as can be seen in Fig. 18.

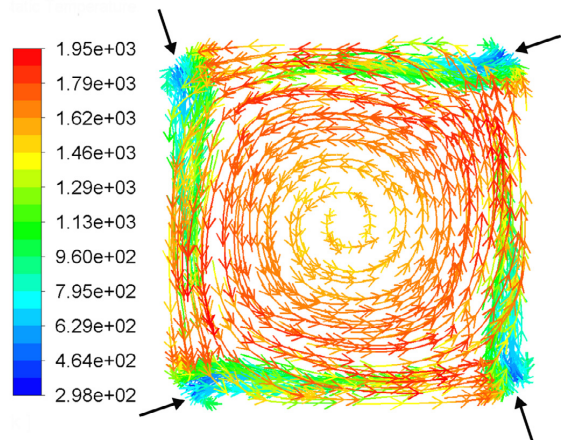


Fig. 17. Pathlines in the plane of injection 3 coloured by temperature [K]. Black arrows indicate locations and directions at which particles are introduced.

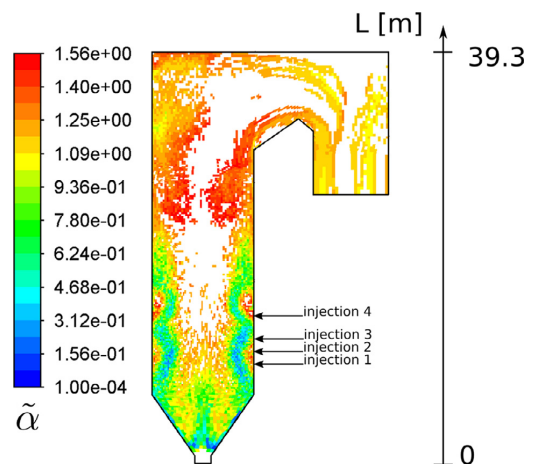


Fig. 18. Distribution of $\tilde{\alpha}$ in the boiler central cross section. Arrows indicate elevations of fuel injection ports.

To investigate the effect of turbulence in this particular boiler, we compared the degree of carbon conversion along the boiler height in Fig. 19. These results were obtained in an equivalent way to Fig. 8. The four panels in the figure correspond to the four levels of particle injections as they are located at different heights in the boiler, as marked in Fig. 18. The points at which carbon conversion is lowest reveals where the particles are injected. Please note that the coal is introduced through all four injections simultaneously so the particles from different injections influence each other; it is only for clarity that we follow particles introduced through each injection separately and divide the results into four panels. It can be seen that for particles spiraling up the boiler the effect of turbulence on the conversion rate is rather insignificant, there is only a slight increase in the conversion rate for most injections, except for the injection 4 which is located the highest in the boiler. The situation changes for particles that travel down the boiler, i.e. the particles that are introduced mostly by injections 1 and 2. There, a clear reduction in the conversion rate can be observed which means that in these regions the conditions are just right for turbu-

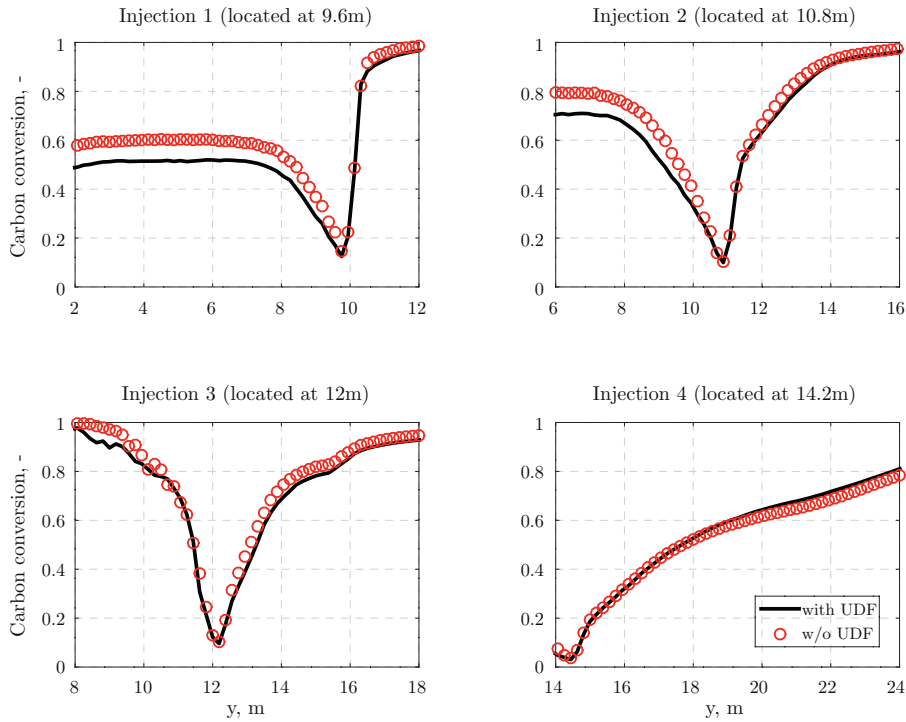


Fig. 19. Char conversion as a function of boiler height as predicted for the baseline case and the case with the UDF.

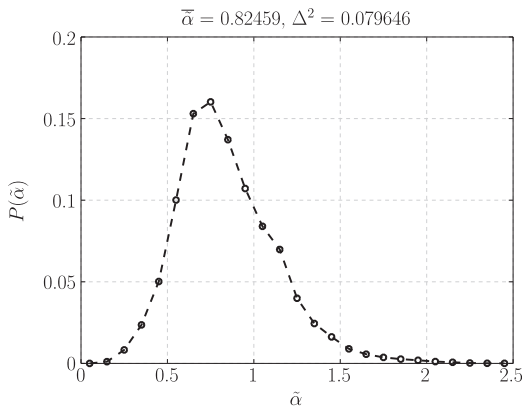


Fig. 20. Probability distribution of $\tilde{\alpha}$ inside the boiler.

lence to cause particle clustering. This is consistent with Fig. 18 in which $\tilde{\alpha}$ is smallest in the lower part of the boiler.

It should be noted that from Fig. 19 it is still not possible to deduce to what extent the overall conversion rate is affected and what fraction of particles has their conversion rate affected by clustering. This important information can be conveyed through Fig. 20, which presents probability distribution of $\tilde{\alpha}$ inside the boiler. From the figure, it can be seen that for majority (79.2%) of reacting particles $\tilde{\alpha} < 1$ and that on average $\tilde{\alpha} = 0.825$. Taking into account results in Fig. 18, it can be concluded that the particle concentration is much higher in the lower part of the boiler

where $\tilde{\alpha} < 1$. However, despite the fact that such a large fraction of particles is affected by the effect of clustering, the global rate reduction given by

$$\text{Rate reduction} = 1 - \left(\sum_{i=1}^{n_{\text{part}}} \frac{m_{c,0,i}}{t_{c,i}} \right)_{\text{withUDF}} / \left(\sum_{i=1}^{n_{\text{part}}} \frac{m_{c,0,i}}{t_{c,i}} \right)_{\text{w/oUDF}} \quad (40)$$

is equal to 2.02% (in the above, t_c is a total combustion time). The reason that the global rate reduction is so low for this particular boiler, is that it is relatively cold in the volumes where $\tilde{\alpha}$ is small, which is typically in the bottom part of the boiler. This means that the conversion rate is largely controlled by kinetics in the same areas where the clustering happens to be slowing down the mass transfer. Hence, the effect of the slow mass transfer is diminished.

Overall, for this boiler, the influence of turbulence on the conversion rate is weaker than what could be anticipated based on our theoretical predictions. This highlights that many variables and the interplay between them are relevant when predicting the effect of turbulence on the char conversion rate. It also shows that it is difficult to determine a priori if this effect needs to be accounted for. Based on what we have learned from this study, we do believe that the effect of char clustering may have significantly more effect on other applications or boiler geometries.

5. Conclusions

It has recently been shown that turbulence may both increase and decrease the mass transfer rate to reacting pulverized particles. More specifically, turbulence may decrease the fluid-particle mass transfer rate when the life time of turbulence induced particle clusters is comparable to the consumption rate of any gaseous

reactant. If particle clustering is not important, the mass transfer rate to the particles may be *increased* due to turbulence induced relative velocity between particle and fluid. Both of these effects are accounted for in a natural manner if all relevant turbulent scales are resolved on the numerical mesh. This is the case for DNS and potentially also for well resolved large eddy simulations (LES), but it is *not* the case for RANS simulations. Naively, one may think that the classical turbulence particle dissipation model that is commonly used in many RANS simulations may accurately account for the relative velocity between particle and fluid. This is, however, not the case. Instead they are grossly overpredicting the relative velocity between particles and fluid and, hence, the mass transfer rate. This is particularly the case for smaller particles.

In the present work, we use the numerical model that was developed by Haugen et al. [17] to assess the effect of turbulence on the char conversion rate for two realistic cases. The first case is a simplified jet burner while the other is an industrial scale boiler. In addition, several theoretical examples are given to show the influence of the selected parameters. The most promising conditions to observe the effect of turbulence on the conversion rate were found to include relatively large particles, large-scale facilities, fuel-rich conditions, moderate turbulence intensity and a low stoichiometric air-fuel ratio.

From the simplified jet burner, we show that the effect of turbulence can be significant for a quite wide range of parameters, such as fuel mass flow rates, particle sizes and jet velocities. It is, however, crucial to consider how the selected parameters influence not only the mass transfer rate ($\tilde{\alpha}$), but also the ratio of the diffusion and kinetic rates. The reason for this is that for low temperatures, where the reactions are kinetically dominated, a reduction in the mass transfer rate will not have any effect on the conversion rate of char. Nevertheless, for some of the cases studied, the distance where full conversion of char was achieved was increased by 50% when proper account was made for the effect of turbulence.

The industrial scale boiler was studied as an example of a real practical system in which the turbulence can play a role. Inside the boiler, we did observe regions where the char conversion rate was both increased and decreased due to the turbulence. However, the density of particles in this kind of boiler is typically too low to observe a strong decrease in the global conversion rate of char. Similarly, the effect associated with relative velocity differences is rather minor. We expect this effect to show a greater importance in systems characterized by larger particles (higher Stokes numbers) since small particles quickly adjust to fluid motions without any significant relative velocity between them and the fluid.

Even though the effect of turbulence is not very dramatic in the industrial boiler studied here, we know from the example with the simplified burner that for certain conditions it will indeed have a strong effect. One should therefore always include the effect of turbulence in RANS simulations used for accurate predictions of char burnout.

In the future one should also study how turbulence affect the reaction rates of solid particles in other industrial facilities, such as char conversion in e.g. gasifiers or MILD combustors. Another interesting application would be oxidation of ilmenite in the air reactor of a Chemical Looping Combustion (CLC) system.

Declaration of Competing Interest

The authors declare that they have no known competing financial interests or personal relationships that could have appeared to influence the work reported in this paper.

Acknowledgments

The research leading to these results has received funding from the research projects: 'CHEERS', financed by the European Union's [Horizon 2020](#) research and innovation program (grant agreement No. 764697), 'GASPRO', financed by the [Research Council of Norway](#) (grant agreement No. 267916) and Opus 13 operated by the Polish National Science Centre (project contract No. UMO-2017/25/B/ST8/00957). This study has been partially supported by the statutory research fund of the Silesian University of Technology, Faculty of Energy and Environmental Engineering, Institute of Thermal Technology, Gliwice, Poland.

Appendix A. Derivation of the stoichiometric number density $n_{p,st}$ and packing limit

The gas and solids volume fractions sum up to unity

$$\epsilon_s + \epsilon_g = \frac{V_s}{V} + \frac{V_g}{V} = 1 \quad (\text{A.1})$$

$$\rho_s = \frac{m_s}{V} = n_p m_p = n_p \rho_p \frac{\pi d_p^3}{6} = \epsilon_s \rho_p \quad (\text{A.2})$$

$$\rho_g = \frac{m_g}{V} = \rho \epsilon_g \quad (\text{A.3})$$

$$\epsilon_s + \epsilon_g = \frac{\rho_s}{\rho_p} + \frac{\rho_g}{\rho} = 1 \quad (\text{A.4})$$

$$\frac{1}{\rho_p} + \frac{\rho_g}{\rho_s \rho} = \frac{1}{\rho_s} \quad (\text{A.5})$$

Taking the ratio of gas to solids such that it is stoichiometric

$$\gamma_{st} = \frac{\rho_g}{\rho_s} \quad (\text{A.6})$$

and using [Eqs. \(A.2\)](#) and [\(A.5\)](#) becomes

$$\frac{1}{\rho_p} + \frac{\gamma_{st}}{\rho} = \frac{6}{n_{p,st} \rho_p \pi d_p^3} \quad (\text{A.7})$$

$$n_{p,st} = \frac{6}{\rho_p \pi d_p^3} \frac{\rho \rho_p}{\gamma_{st} \rho_p + \rho} = \frac{6}{\pi d_p^3} \frac{1}{\gamma_{st} \frac{\rho_p}{\rho} + 1} \quad (\text{A.8})$$

which for $\frac{\rho_p}{\rho} \gg 1$ becomes

$$n_{p,st} \approx \frac{6}{\pi d_p^3} \frac{\rho}{\gamma_{st} \rho_p} \quad (\text{A.9})$$

For a given γ_{st} , $n_{p,st}$ is the stoichiometric particle number density, for which $\tilde{\alpha}$ can be determined. The relation between the particle number density n_p and solids volume fraction ϵ_s is

$$n_p = \frac{6}{\pi d_p^3} \epsilon_s. \quad (\text{A.10})$$

Thus, for a given particle number density, the maximum diameter the particle can have without exceeding the packing limit can be computed from

$$d_{p,max} = \left(\frac{6\epsilon_{s,max}}{\pi n_p} \right)^{1/3}. \quad (\text{A.11})$$

The relation between the density ratio γ_{st} and solids volume fraction ϵ_s is

$$\epsilon_s = \frac{1}{\gamma_{st} \frac{\rho_p}{\rho} + 1} \quad (\text{A.12})$$

From the above the solids volume fraction at stoichiometric conditions can be determined, i.e. for γ_{st} from [Table 1](#).

Supplementary material

Supplementary material associated with this article can be found, in the online version, at doi:[10.1016/j.combustflame.2020.12.040](https://doi.org/10.1016/j.combustflame.2020.12.040).

References

- [1] H. Thunman, K. Davidsson, B. Leckner, Separation of drying and devolatilization during conversion of solid fuels, *Combust. Flame* 137 (1) (2004) 242–250, doi:[10.1016/j.combustflame.2004.02.008](https://doi.org/10.1016/j.combustflame.2004.02.008).
- [2] S. Saxena, Devolatilization and combustion characteristics of coal particles, *Prog. Energy Combust. Sci.* 16 (1) (1990) 55–94, doi:[10.1016/0360-1285\(90\)90025-X](https://doi.org/10.1016/0360-1285(90)90025-X).
- [3] R.C. Borah, P. Ghosh, P.G. Rao, A review on devolatilization of coal in fluidized bed, *Int. J. Energy Res.* 35 (11) (2011) 929–963, doi:[10.1002/er.1833](https://doi.org/10.1002/er.1833).
- [4] J. Yu, J.A. Lucas, T.F. Wall, Formation of the structure of chars during devolatilization of pulverized coal and its thermoproperties: a review, *Prog. Energy Combust. Sci.* 33 (2) (2007) 135–170, doi:[10.1016/j.pecs.2006.07.003](https://doi.org/10.1016/j.pecs.2006.07.003).
- [5] M. Vascellari, R. Arora, M. Pollack, C. Hasse, Simulation of entrained flow gasification with advanced coal conversion submodels. Part 1: pyrolysis, *Fuel* 113 (2013) 654–669, doi:[10.1016/j.fuel.2013.06.014](https://doi.org/10.1016/j.fuel.2013.06.014).
- [6] M. Vascellari, R. Arora, C. Hasse, Simulation of entrained flow gasification with advanced coal conversion submodels. Part 2: char conversion, *Fuel* 118 (2014) 369–384, doi:[10.1016/j.fuel.2013.11.004](https://doi.org/10.1016/j.fuel.2013.11.004).
- [7] M. Baum, P. Street, Predicting the combustion behaviour of coal particles, *Combust. Sci. Technol.* 3 (5) (1971) 231–243, doi:[10.1080/00102207108952290](https://doi.org/10.1080/00102207108952290).
- [8] M.A. Field, Rate of combustion of size-graded fractions of char from a low-rank coal between 1 200°K and 2 000°K, *Combust. Flame* 13 (3) (1969) 237–252, doi:[10.1016/0010-2180\(69\)90002-9](https://doi.org/10.1016/0010-2180(69)90002-9).
- [9] R.H. Hurt, M.M. Lunden, E.G. Brehob, D.J. Maloney, Statistical kinetics for pulverized coal combustion, *Symp. (Int.) Combust.* 26 (2) (1996) 3169–3177, doi:[10.1016/S0082-0784\(96\)80162-7](https://doi.org/10.1016/S0082-0784(96)80162-7).
- [10] R. Hurt, J.-K. Sun, M. Lunden, A kinetic model of carbon burnout in pulverized coal combustion, *Combust. Flame* 113 (1) (1998) 181–197, doi:[10.1016/S0010-2180\(97\)00240-X](https://doi.org/10.1016/S0010-2180(97)00240-X).
- [11] S. Niksa, G.S. Liu, R.H. Hurt, Coal conversion submodels for design applications at elevated pressures. Part I. Devolatilization and char oxidation 29 (5) (2003) 425–477, doi:[10.1016/S0360-1285\(03\)00033-9](https://doi.org/10.1016/S0360-1285(03)00033-9).
- [12] G.S. Liu, S. Niksa, Coal conversion submodels for design applications at elevated pressures. Part II. Char gasification 30 (6) (2004) 679–717, doi:[10.1016/j.pecs.2004.08.001](https://doi.org/10.1016/j.pecs.2004.08.001).
- [13] N.E.L. Haugen, M.B. Tilghman, R.E. Mitchell, The conversion mode of a porous carbon particle during oxidation and gasification, *Combust. Flame* 161 (2014) 612–619, doi:[10.1016/j.combustflame.2013.09.012](https://doi.org/10.1016/j.combustflame.2013.09.012).
- [14] N.E.L. Haugen, R.E. Mitchell, M.B. Tilghman, A comprehensive model for char particle conversion in environments containing O₂ and CO₂, *Combust. Flame* 162 (2015) 1455–1463, doi:[10.1016/j.combustflame.2014.11.015](https://doi.org/10.1016/j.combustflame.2014.11.015).
- [15] M.B. Tilghman, N.E.L. Haugen, R.E. Mitchell, A comprehensive char-particle gasification model adequate for entrained-flow and fluidized-bed gasifiers, *Energy Fuels* 31 (2015) 2164–2174, doi:[10.1021/acs.energyfuels.6b02148](https://doi.org/10.1021/acs.energyfuels.6b02148).
- [16] J. Krüger, N. Haugen, T. Løvås, D. Mitra, The effect of turbulence on the reaction rate of particles with heterogeneous surface reactions, *Proc. Combust. Inst.* 36 (2017) 2333–3240, doi:[10.1016/j.proci.2016.06.187](https://doi.org/10.1016/j.proci.2016.06.187).
- [17] N. Haugen, J. Krüger, D. Mitra, T. Løvås, The effect of turbulence on mass transfer rates of small inertial particles with surface reactions, *J. Fluid Mech.* 836 (2018) 932–951, doi:[10.1017/jfm.2017.820](https://doi.org/10.1017/jfm.2017.820).
- [18] J. Krüger, N.E.L. Haugen, T. Løvås, Correlation effects between turbulence and the conversion rate of pulverized char particles, *Combust. Flame* 185 (2017) 160–172, doi:[10.1016/j.combustflame.2017.07.008](https://doi.org/10.1016/j.combustflame.2017.07.008).
- [19] E. Karchniwy, A. Klimanek, N. Haugen, The effect of turbulence on mass transfer rates between inertial polydisperse particles and fluid, *J. Fluid Mech.* 874 (2019) 1147–1168, doi:[10.1017/jfm.2019.493](https://doi.org/10.1017/jfm.2019.493).
- [20] I. Smith, The combustion rates of coal chars: a review, *Symp. (Int.) Combust.* 19 (1) (1982) 1045–1065, doi:[10.1016/S0082-0784\(82\)80281-6](https://doi.org/10.1016/S0082-0784(82)80281-6).
- [21] D.D. Toporov, Combustion of Pulverized Coal in a Mixture of Oxygen and Recycled Flue Gas, Elsevier Insights, Elsevier, 2015, doi:[10.1016/C2013-0-19301-4](https://doi.org/10.1016/C2013-0-19301-4).
- [22] A. Hayhurst, The mass transfer coefficient for oxygen reacting with a carbon particle in a fluidized or packed bed, *Combust. Flame* 121 (2000) 679–688, doi:[10.1017/jfm.2017.820](https://doi.org/10.1017/jfm.2017.820).
- [23] L. Chen, S.Z. Yong, A.F. Ghoniem, Oxy-fuel combustion of pulverized coal: characterization, fundamentals, stabilization and CFD modeling, *Prog. Energy Combust. Sci.* 38 (2) (2012) 156–214, doi:[10.1016/j.pecs.2011.09.003](https://doi.org/10.1016/j.pecs.2011.09.003).
- [24] W. Ranz, W. Marshall, Evaporation from drops, part I, *Chem. Eng. Prog.* 48 (3) (1952) 141–146.
- [25] S. Kriebitzsch, A. Richter, LES simulation of char particle gasification at Reynolds numbers up to 1000, *Combust. Flame* 211 (2020) 185–194, doi:[10.1016/j.combustflame.2019.08.028](https://doi.org/10.1016/j.combustflame.2019.08.028).
- [26] W. Rodi, *Turbulence Models and Their Application in Hydraulics – a State of the Art Review*, NASA STI/Recon Technical Report A, 1980.
- [27] B.E. Launder, D.B. Spalding, The numerical computation of turbulent flows, *Comput. Methods Appl. Mech. Eng.* (3) (1974) 269–289.
- [28] W.P. Adamczyk, B. Isaac, J. Parra-Alvarez, S.T. Smith, D. Harris, J.N. Thornock, M. Zhou, P.J. Smith, R. Żmuda, Application of LES-CFD for predicting pulverized-coal working conditions after installation of NO_x control system, *Energy* 160 (2) (2018) 693–709, doi:[10.1016/j.energy.2018.07.031](https://doi.org/10.1016/j.energy.2018.07.031).

5.3 Paper III

A numerical study on the combustion of a resolved carbon particle

Ewa Karchniwy, Nils Erland L. Haugen, Adam Klimanek

Submitted for consideration to Combustion and Flame

A numerical study on the combustion of a resolved carbon particle

Ewa Karchniwy^{a,b,*}, Nils Erland L. Haugen^c, Adam Klimanek^a

^a*Department of Thermal Technology, Silesian University of Technology,
Konarskiego 22, 44-100 Gliwice, Poland*

^b*Department of Energy and Process Engineering, Norwegian University of Science and
Technology, Kolbjørn Hejes vei 1B, NO-7491 Trondheim, Norway*

^c*SINTEF Energi A.S., Sem Saelands vei 11, 7034 Trondheim, Norway*

Abstract

Combustion of a single, resolved carbon particle is studied using a novel numerical approach that makes use of an overset grid. The model is implemented into the framework of a compressible Direct Numerical Simulation (DNS) code. A method to artificially reduce the speed of sound is presented. For Mach numbers lower than ~ 0.1 this method may dramatically improve numerical efficiency without affecting any physical aspects except for the acoustics. The ability of the model to simulate solid fuel combustion is demonstrated and all parts of the model are validated against experimental and numerical data. A sensitivity of the carbon conversion rate to selected parameters (diffusion coefficients and homogeneous and heterogeneous kinetics) is investigated. A strong dependence on the oxygen diffusivity is observed and explained.

Keywords: resolved particle, char conversion, overset grid, multiphase reactive flows, solid fuel combustion

1. Introduction

Solid fuels are among the most important energy sources worldwide. On one hand, some countries, like e.g. China, India or Poland, are still vastly

*Corresponding author. Tel.: +48322372810

Email address: ewa.karchniwy@gmail.com (Ewa Karchniwy)

dependent on coal [1]. On the other hand, the contribution to the energy production from solid fuels in the form of biomass and refuse-derived fuel is increasing every year [2]. Due to its strong effect on global warming, emission of carbon dioxide from solid fuels conversion is a serious environmental problem. This, in connection with the global increase in energy demand [3], necessitates development of low-emission and efficient solid fuel-based technologies. Such technologies cannot be designed without a thorough knowledge about fuel properties and understanding of the underlying fuel conversion phenomena. This understanding is currently provided by experiments and by numerical simulations. Experimental investigation of solid fuels combustion is difficult because of complex physical and chemical processes occurring at different scales. As a consequence, information provided by experiments may not be complete. A deeper insight can be gained through detailed numerical simulations, in which all flow scales are resolved on a numerical grid. It should be stressed, however, that both research methods are complementary and equally important.

In Direct Numerical Simulation (DNS) studies on solid fuels conversion in turbulent systems, particles are commonly represented as point sources. This approach has previously been employed to study different aspects of pulverized coal combustion, for example in jet flames [4, 5, 6] and mixing layers [7, 8, 9]. The approximation of point particles is applicable only to very small particles, i.e. to particles with diameters smaller than Kolmogorov length scales of turbulence [10]. Also, in such simulations, interactions between the fluid and particles must be modeled using closure expressions. These expressions can be supplied by simulations in which the particle surface and its boundary layer are resolved on the numerical mesh. Even though such resolved simulations are typically limited to one or a few particles, this approach has a great potential to provide an understanding of the solid fuel conversion and gas-particle interactions at a very fundamental level. The resolved particle approach has recently been employed in several numerical investigations of coal or carbon conversion. Devolatilization and ignition stages of the resolved pulverized coal particle were considered by Vascellari et al. [11], whose studies were extended by Tufano et al. [12] to account for different atmospheres and a more accurate description of the volatile yield and composition. The same research group further broadened the focus of their studies on resolved coal particles by considering particle arrays [13], higher particle Reynolds numbers and effects of turbulence [14]. A number of publications neglect the devolatilization and investigate resolved char par-

particle combustion and gasification in steady state. For example, Kestel et al. [15] studied the impact of steam content and Reynolds number on the char oxidation in air, while the effects of the ambient gas temperature, gas velocity and oxygen mass fractions in O_2/CO_2 atmosphere were considered by Richter et al. [16]. A similar analysis was also performed by Safronov et al. [17] who indicated differences in combustion behavior between micro- and millimeter-sized particles. The conversion of a collection of resolved carbon particles was also investigated in a similar way by Schulze et al. [18]. Furthermore, the steady state approach was employed in a few studies [19, 20, 21] that attempted to resolve porous particle and understand intrinsic reactivity. It was shown that both porosity and pore structure can affect char conversion.

As demonstrated by the above-mentioned examples, a great deal of understanding can be reached with the steady state assumption. However, all transient phenomena and processes (ignition, volatiles burnout, progress of char conversion, combustion in non-laminar flow) require unsteady approach. The first transient simulations of resolved particle combustion in a non-quiescent (two-dimensional) flow were performed by Lee et al. [22] using the spectral element method. Recently, Farazi et al. [23] used an unsteady approach and a detailed chemical mechanism, and investigated char particle combustion in air and oxy-fuel atmospheres. The combustion characteristics in these two atmospheres were explored, as well as interactions between kinetics and mass transfer. This work was further extended to particle arrays by Sayadi et al. [24]. Another study on the resolved particle conversion in which the governing equations were solved in their unsteady form was done by Luo et al. [6]. In their work, an immersed boundary method and a simple semi-global mechanism were utilized. Finally, Tufano et al. [25] performed the most complete study up to date, in which all stages of the coal particle conversion are considered, i.e. heating, drying, ignition, volatiles combustion and char particle conversion. Moreover, in addition to detailed chemistry, their numerical model accounts for complex features of particle interior, such as time evolution of porosity and tortuosity. Most recently, Nguyen et al. [26] performed unsteady particle-resolved simulations to investigate the evolution of char particle morphology. Based on their results, improved expressions for the mode of burning and the Random Pore Model were proposed.

In the existing literature on resolved particle conversion, very different levels of numerical model complexity are presented. The current trend seems to be towards more and more detailed models and models that are able to capture transient effects. However, high accuracy is achieved at the expense

of efficiency. The objective of this work is to propose a novel numerical approach for resolved char particle combustion modeling. Contrary to the present trend in the literature, we aim for the model to be as simple and efficient as possible, while still preserving high accuracy and being able to predict unsteady phenomena. This is accomplished by using structured, overset grids and by introducing carefully verified assumptions and simplifications.

2. Governing equations and numerical methods

An open-source, compressible solver called the Pencil Code [27] is used to perform the simulations presented in this work. The Pencil Code uses a 6th order finite difference scheme and a 3rd order Runge-Kutta scheme for spatial and temporal discretization, respectively. One of the main features of the numerical approach employed in this study is the overset grid. The particle is surrounded by a cylindrical body-fitted grid (later also referred to as 'ogrid'), which spans the space between $r = r_p$ to $r = 3r_p = r_{ogrid}$, where r is a radial coordinate and r_p is the particle radius. The rest of the computational domain is resolved on the Cartesian grid. Such an approach allows one to use very high resolution close to the particle, which is necessary to resolve its boundary layer and the surrounding flame. Further away from the particle, the grid is much coarser, making the computational effort relatively low. The solution is interpolated between the ogrid and the Cartesian grid using a 4th order, explicit Lagrangian interpolation method, which has been shown to be an optimal choice in connection with a 6th order finite difference scheme [28, 29]. In order to avoid spurious oscillations, Padé filtering [30, 31] is applied on the cylindrical grid to density, temperature and velocity fields. The details about the implementation of the overset grid and performance of this method can be found in [32] and [33].

2.1. Fluid equations

The continuity and momentum equations are solved in their non-conservative, compressible form:

$$\frac{\partial \rho}{\partial t} + \nabla \cdot (\rho \mathbf{u}) = 0, \quad (1)$$

$$\rho \frac{\partial \mathbf{u}}{\partial t} + \rho \mathbf{u} \cdot \nabla \mathbf{u} = -\nabla p + \nabla \cdot \underline{\underline{\boldsymbol{\tau}}} + \mathbf{f}, \quad (2)$$

where ρ and p are the density and pressure, respectively, and the bold symbols represent the velocity (\mathbf{u}) and volumetric force (\mathbf{f}) vectors. The stress tensor, $\underline{\boldsymbol{\tau}}$, is given by

$$\underline{\boldsymbol{\tau}} = \mu(\nabla\mathbf{u} + (\nabla\mathbf{u})^T) - \frac{2}{3}\mu(\nabla \cdot \mathbf{u})\underline{\mathbf{I}}, \quad (3)$$

where μ stands for the dynamic viscosity and $\underline{\mathbf{I}}$ is the identity matrix. The mass fraction of chemical species k , given by Y_k , obeys the following transport equation

$$\rho \frac{\partial Y_k}{\partial t} + \rho \mathbf{u} \cdot \nabla Y_k = -\nabla \cdot \mathbf{J}_k + \dot{\omega}_k, \quad (4)$$

in which the diffusive flux, \mathbf{J}_k , is simplified by using the assumption of Fickian diffusion, such that

$$\mathbf{J}_k = -\rho D_k \nabla Y_k, \quad (5)$$

where D_k is the diffusion coefficient of species k and $\dot{\omega}_k$ represents the gas phase reaction rate of the same species.

By neglecting viscous heating, the energy equation is expressed in terms of temperature as [34]

$$\rho \frac{\partial T}{\partial t} + \rho \mathbf{u} \cdot \nabla T = \sum_k (\dot{\omega}_k - \nabla \cdot \mathbf{J}_k) \left(\frac{TR}{c_v M_k} - \frac{h_k}{c_v} \right) - \frac{\rho TR}{c_v M} \nabla \cdot \mathbf{u} - \frac{\nabla \cdot \mathbf{q}}{c_v}, \quad (6)$$

where T represents the temperature, c_v is the heat capacity at constant volume, R is the universal gas constant and M is the molar mass for the mixture, $1/M = \sum_k Y_k/M_k$. The heat flux, \mathbf{q} , is computed as

$$\mathbf{q} = \sum_k h_k \mathbf{J}_k - \lambda \nabla T, \quad (7)$$

where λ represents thermal conductivity and $h_k = \Delta h_{s,k} + h_{f,k}^0$ is the absolute enthalpy of species k , which is the sum of its sensible enthalpy, $\Delta h_{s,k}$, and its heat of formation, $h_{f,k}^0$. Finally, to relate density with pressure, the ideal gas equation of state is used,

$$p = \frac{\rho RT}{M}. \quad (8)$$

reaction	B_i	E_i [kcal/mol]	r_i	source
R1	1.97×10^9 cm / s	47.3	$k_1[\text{O}_2]$	[36]
R2	1.29×10^7 cm / s	45.6	$k_2[\text{CO}_2]$	[36]
R3 (forward)	$3.98 \times 10^{14} \left(\frac{\text{cm}^3}{\text{mol}}\right)^{3/4}$ /s	40.7	$k_{3,f}[\text{CO}][\text{H}_2\text{O}]^{1/2}[\text{O}_2]^{1/4}$	[37]
R3 (reverse)	5×10^8 1/s	40.7	$k_{3,r}[\text{CO}_2]$	[37]

Table 1: Kinetic parameters. Here, $[a]$ denotes concentration of species a , k_i is given by Eq. (9) and r_i represents the rate-of-progress variable. Note that for surface reactions units of r_i are mol/cm²/s, while for gas phase reactions it is mol/cm³/s

2.2. Chemical mechanism and boundary conditions

A simplified chemical mechanism that consists of two surface reactions and one reversible gas phase reaction is employed:



The Arrhenius expression for reaction i reads

$$k_i = B_i \exp(-E_i/RT). \quad (9)$$

The empirical kinetic parameters: pre-exponential factor B_i , activation energy E_i and reaction orders are listed in Table 1. The reaction term for the gas phase reaction in Eq. (4) is computed as

$$\dot{\omega}_k = M_k \sum_{i=1}^{n_{r,gas}} (\nu''_{ki} - \nu'_{ki}) r_i, \quad (10)$$

where ν'_{ki} and ν''_{ki} are the stoichiometric coefficients of gas phase species k in reaction i on the reactant and product side, respectively, while $n_{r,gas}$ is the number of gas phase reactions, and r_i is the rate-of-progress variable (adopting terminology from Ch. 4 in [35]), as given in Table 1.

Since the particle interior is not included in the current framework, it is assumed that all contributions to the reaction rate due to internal reactions are accounted for through the apparent kinetic parameters, and that the temperature gradient inside the particle is small enough to be neglected. Also, the particle is assumed to be entirely made of carbon and the model

does not incorporate particle shrinkage during its conversion. In reality, the particle size and density are slowly changing as combustion progresses [38]. However, the typical time of our simulations is much shorter than the burnout time of the particle such that the reduction of the particle diameter can be considered negligible.

As stated above, the interior of the particle is not included in the computational mesh. The interaction between the solid and the surrounding gas is therefore incorporated through the particle boundary conditions. We will now continue by describing these boundary conditions. The species balance at the cylinder surface can be expressed as [6]:

$$\rho D_k \frac{\partial Y_k}{\partial r} + \dot{m}_c Y_k + \dot{m}_k = 0, \quad (11)$$

where

$$\dot{m}_k = M_k \sum_{i=1}^{n_{r,heter}} (\nu''_{ki} - \nu'_{ki}) r_i, \quad (12)$$

is the production rate of species k due to heterogeneous reactions, and $n_{r,heter}$ is the number of heterogeneous reactions. The char conversion rate is given by

$$\dot{m}_c = -M_C(2k_1[\text{O}_2] + k_2[\text{CO}_2]) = -(\dot{m}_{\text{O}_2} + \dot{m}_{\text{CO}_2} + \dot{m}_{\text{CO}}) = - \sum_{k=1}^{n_{s,gas}} \dot{m}_k, \quad (13)$$

where the final summation is over all gas-phase species. A detailed deduction of Eq. (11) can be found in [Appendix A](#). It should be noted that both \dot{m}_c and \dot{m}_k depend on the species concentration on the surface, which makes it necessary to solve Eq. (11) in an iterative manner. Another possibility is to use species production rates from the previous time step, this can however lead to numerical instabilities and non-physical results. Here, we employ a simple iterative algorithm to simultaneously find solutions for Y_{O_2} and Y_{CO_2} at the surface, while the remaining species are solved for directly.

Mass conservation at the particle surface requires that (see [Appendix A](#))

$$\sum_k (\rho Y_k \mathbf{u} + \mathbf{J}_k) \cdot \hat{\mathbf{r}} = \sum_k \dot{m}_k = -\dot{m}_c, \quad (14)$$

where $\hat{\mathbf{r}}$ is the vector normal to the particle surface. From the above equation, and since $\sum_k \mathbf{J}_k \cdot \hat{\mathbf{r}} = 0$, the boundary condition for velocity becomes:

$$u_r = -\dot{m}_c / \rho, \quad (15)$$

where u_r is the outward velocity in the radial direction, corresponding to the so called Stefan flow.

Dirichlet boundary condition is employed for the temperature. The intention behind the Dirichlet boundary condition for temperature is to validate the code against the experimental data of Makino et al. [39], where the temperature was maintained constant. The last variable that needs to be defined at the cylinder surface is density, which is solved for directly from the transport equation and does therefore not require any special treatment at the boundary.

2.3. Transport properties

In simulations of reacting flows, it is common practice to compute transport coefficients, such as μ_k , D_k and thermal diffusivity D_{th} , based on the kinetic theory of gases, as described e.g. in [34]. This approach, while accurate, significantly increases computational cost. This is especially the case for species diffusion coefficients for which binary diffusion coefficients need to be evaluated first. In order to maximize computational efficiency, a simplified approach is employed in this work. At the same time, care is taken not to compromise the accuracy of the results.

The kinetic viscosity is related to temperature through Sutherland's law

$$\nu = \frac{C_1 T^{3/2}}{\rho(T + C_2)} \quad (16)$$

with constants $C_1 = 1.52 \cdot 10^{-6}$ kg/m/s/K^{1/2} and $C_2 = 110$ K. The above expression is fully applicable to single-component gases. However, if a mixture is dominated by components with similar properties (as is the case here), Eq. (16) is reduced to a decent approximation. Furthermore, constants C_1 and C_2 were selected such that for a wide range of temperatures and compositions the kinetic viscosity resulting from Eq. (16) is in a good agreement with the kinetic viscosity determined using the multi-component approach (i.e. based on kinetic theory). In Fig. 1, these two methods are compared for a typical composition encountered in the current work. For other compositions that are likely to occur, a deviation from the kinetic theory remains below 7% for the temperature range presented in Fig. 1.

The main assumption allowing us to compute the remaining transport coefficients is that the transport coefficients are proportional to each other, i.e.

$$\nu = \text{Pr} D_{th} = \text{Pr} \text{Le}_k D_k, \quad (17)$$

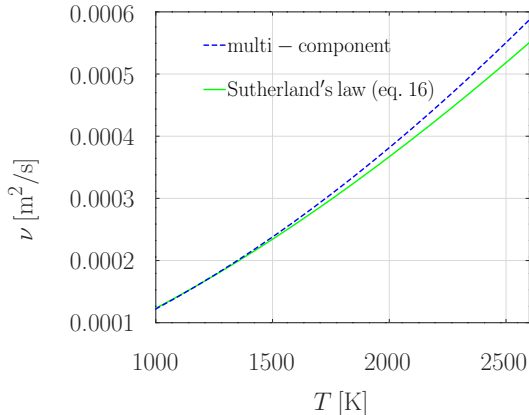


Figure 1: Kinetic viscosity as obtained using Sutherland’s law (Eq. (16)) and multi-component approach for the mixture consisting of $Y_{N_2} = 0.7292$, $Y_{O_2} = 0.05$, $Y_{H_2O} = 0.0008$, $Y_{CO} = 0.02$ and $Y_{CO_2} = 0.2$

with the constants of proportionality being the Prandtl (Pr) and Lewis (Le_k) numbers. Such an assumption of constant Prandtl and/or Lewis numbers has successfully been applied in recent studies on resolved particle devolatilization and combustion [12, 23]. Typically, $Pr = 0.7$ and $Le_k = 1$ for all species are assumed. This was shown to have a negligible impact on the devolatilization stage when compared with the complex multi-component approach [12]. However, in some conditions, the combustion rate might be affected by diffusion coefficients, as will be demonstrated in the next section. Therefore, a more careful approach is employed, as described below.

The heat capacity at constant pressure is given by

$$c_p = \sum_k Y_k c_{p,k} = \frac{R}{M} \sum_k Y_k \sum_{i=1}^5 a_i T^{i-1}, \quad (18)$$

where the polynomial coefficients a_i are taken from [40] and are listed in table 2 for the relevant temperature range. The heat capacity at constant volume is related to the heat capacity at constant pressure through the gas constant, such that

$$c_p - c_v = R/M. \quad (19)$$

species	CO	CO ₂	H ₂ O	N ₂	O ₂
a_1	3.025	4.454	2.672	2.927	3.698
a_2	$1.443 \cdot 10^{-3}$	$3.140 \cdot 10^{-3}$	$3.056 \cdot 10^{-3}$	$1.488 \cdot 10^{-3}$	$6.135 \cdot 10^{-4}$
a_3	$-5.631 \cdot 10^{-7}$	$-1.278 \cdot 10^{-6}$	$-8.730 \cdot 10^{-7}$	$-5.685 \cdot 10^{-7}$	$-1.259 \cdot 10^{-7}$
a_4	$1.019 \cdot 10^{-10}$	$2.394 \cdot 10^{-10}$	$1.201 \cdot 10^{-10}$	$1.010 \cdot 10^{-10}$	$1.775 \cdot 10^{-11}$
a_5	$-6.911 \cdot 10^{-15}$	$-1.669 \cdot 10^{-14}$	$-6.392 \cdot 10^{-15}$	$-6.753 \cdot 10^{-15}$	$-1.136 \cdot 10^{-15}$

Table 2: Polynomial coefficients for heat capacity in the temperature range $1000\text{ K} < T < 5000\text{ K}$

Using the heat capacity given by Eq. (18) and the thermal diffusivity given by Eq. (17), the thermal conductivity, defined as

$$\lambda = c_p \rho D_{\text{th}}, \quad (20)$$

is shown in Fig. 2 as a function of temperature for the same mixture as used in Fig. 1. In Fig. 2, the thermal conductivity as obtained using the multi-component approach is also presented. The best agreement between these two functions for a wide range of mixtures is achieved by setting the Prandtl number equal to 0.9.

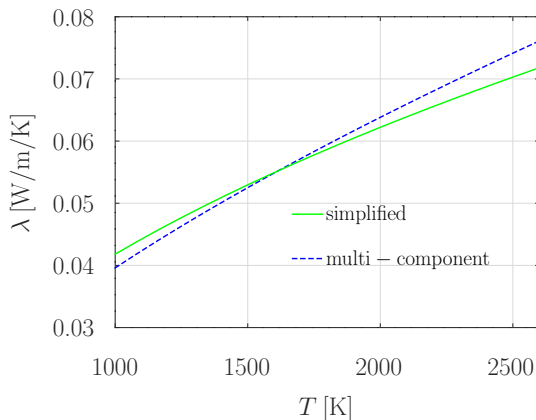


Figure 2: Thermal conductivity as obtained using Eq. (17) with $\text{Pr} = 0.9$ and multi-component approach for the mixture consisting of $Y_{\text{N}_2} = 0.7292$, $Y_{\text{O}_2} = 0.05$, $Y_{\text{H}_2\text{O}} = 0.0008$, $Y_{\text{CO}} = 0.02$ and $Y_{\text{CO}_2} = 0.2$

species	CO	CO ₂	H ₂ O	N ₂	O ₂
Le_k	0.78	1.01	0.58	0.7	0.78

Table 3: Selected Lewis numbers

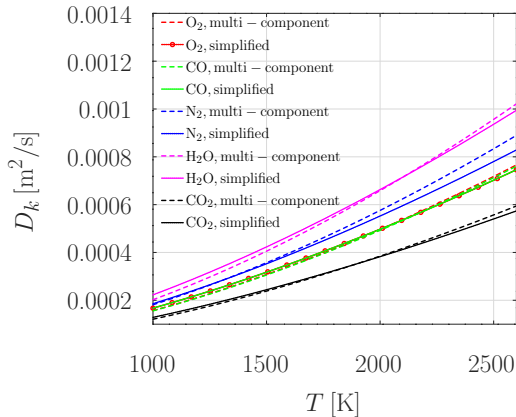


Figure 3: Diffusion coefficients as obtained using Eq. (17) (referred to as 'simplified') and multi-component approach for the mixture consisting of $Y_{N_2} = 0.7292$, $Y_{O_2} = 0.05$, $Y_{H_2O} = 0.0008$, $Y_{CO} = 0.02$ and $Y_{CO_2} = 0.2$

For each species, Le_k is chosen such that the resulting diffusion coefficient does not differ by more than around 10% from the diffusion coefficient computed based on the multi-component diffusion approach. This was verified for the full range of compositions and temperatures that are likely to appear in the cases we examine. Fig. 3 presents a comparison between the diffusion coefficients as a function of temperature as computed from Eq. (17) and as obtained using the multi-component diffusion. The magnitudes of the Lewis numbers leading to these results are listed in Table 3. A good agreement between the two approaches is achieved for all transport coefficients (ν , λ and D_k), which justifies the use of the simplified approach for the transport coefficients.

2.4. Speed of sound reduction

Numerical stability of the simulations requires several conditions to be fulfilled. First of all, a requirement due to convection, often called the CFL

condition limits the maximum time step to:

$$\Delta t \leq \frac{C\Delta x}{\max(c_s + u)}, \quad (21)$$

where C is a constant that depends on a numerical scheme (typically $C \approx 1$) and

$$c_s = \sqrt{\gamma RT/M} \quad (22)$$

is the speed of sound and $\gamma = c_p/c_v$. For reacting flows, the length of the time step and the grid spacing is most often limited by chemical scales. However, it turns out that in the case of flows that are both reacting and compressible, the resolution requirement due to the ratio between viscosity and the speed of sound might be more restrictive. For the particular numerical approach employed in the Pencil Code, it has been shown [41] that the grid spacing is constrained by

$$\Delta x < \frac{\beta\nu}{c_s}, \quad (23)$$

where $\beta \sim 50$. It follows from Eq. (23) that larger grid spacing, and hence less mesh points, may be used if the speed of sound is reduced. A good rule of thumb is that, as long as we are not interested in thermo-acoustics, the results are independent of the Mach number, $\text{Ma} = u/c_s$, for all Mach numbers below 0.1. In our case, the Mach number is typically of the order of 10^{-3} . The speed of sound can therefore be reduced by up to two orders of magnitude while still maintaining Mach-independent results. Since the time step is often limited by the CFL condition, which is typically the case for lower temperatures, a reduction of the speed of sound would also allow us to use larger time steps.

In the previous paragraph we showed that a reduction in the speed of sound could be very beneficial for the CPU consumption of our simulations, and that the effect such a reduction has on the results should be negligible if the Mach number is kept below a certain value. The question now is how the speed of sound can be changed without affecting any other aspect of the results. This is done by dividing the gas constant by a factor α^2 , such that

$$R \rightarrow R/\alpha^2, \quad (24)$$

which implies that (22)

$$c_s \rightarrow c_s/\alpha. \quad (25)$$

The gas constant is changed consistently for all equations, with the exception of Eq. (9) in which the original magnitude of R must be used in order for the reaction rate not to be affected. It should be noted that the reduction of R means that c_p , c_v and λ are also reduced by the same factor of α^2 , as can be seen from Eqs (19) - (20). However, this has no effect on the energy equation as all these reductions cancel out in every term of Eq. (6). The only term that is affected is the pressure gradient term in the momentum equation, since $\nabla p \sim c_s^2$, which is as intended.

We will now validate the assumption that a reduction in the speed of sound does not affect the main results, except for the acoustic waves, as long as the Mach number is below 0.1. This is done by simulating reacting flows of a one-dimensional carbon monoxide flame with three different values of c_s . In the base case, the speed of sound was kept unchanged, which resulted in $\text{Ma} \approx 0.001$, in the other cases the speed of sound was reduced by factors of 10 and 50, which led to $\text{Ma} \approx 0.01$ and $\text{Ma} \approx 0.05$, respectively. The initial conditions for these cases are given in Table 4, while the one-step mechanism given in section 2.2 governs the flame.

	reactant side	product side
Y_{O_2}	0.165	0.0
Y_{CO}	0.29	0.0
Y_{CO_2}	0.0	0.455
$Y_{\text{H}_2\text{O}}$	0.0008	0.0008
Y_{N_2}	0.544	0.544
$T[\text{K}]$	298	2000

Table 4: Initial conditions for 1D carbon monoxide flame

The resulting temperature and species mass fraction profiles at steady state are presented in Fig. 4, from which it can be seen that the results are not affected by the speed of sound reduction. Furthermore, for all three cases, the same flame speed, $S_L = 14$ cm/s, is obtained. Having verified that the speed of sound can be reduced without affecting the results, this tactic is employed for all cases discussed in the next section, which resulted in a major reduction of CPU power consumption, in particular for those cases where the time-step was not limited by chemical reactions.

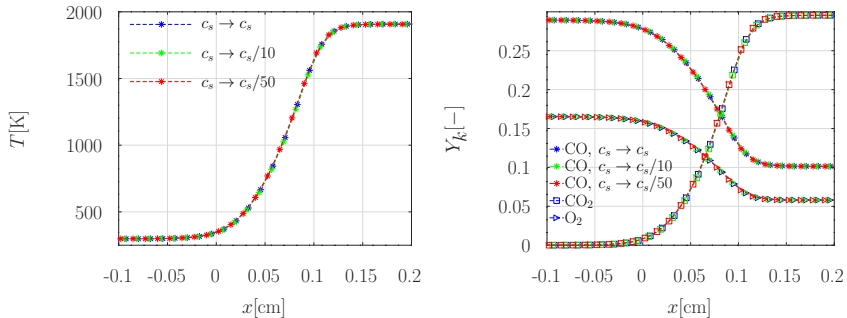


Figure 4: Comparison of temperature and species profiles across the flame obtained before and after the speed of sound reduction

2.5. Numerical set-up

The set-up for all simulated cases correspond to the experimental set-up of Makino et al. [39] and can be summarized as follows. A cylindrical particle of 5mm in diameter is placed in the middle of a 10cm \times 8cm computational domain. The fluid, which has a composition that is typical for air ($Y_{N_2} = 0.77$, $Y_{O_2} = 0.23$, $Y_{H_2O} = 0.0008$) enters the domain through one side with a velocity of 1 m/s in the y -direction. Periodic boundary conditions are specified in the two cross-flow directions. Initially, the temperature inside the domain is everywhere equal to 1280 K. The initial species distribution on the ogrid is such that the oxygen mass fraction decreases exponentially from $Y_{O_2} = 0.23$ at $r = r_{ogrid}$ to $Y_{O_2} = 0$ at the particle surface ($r = r_p$), while carbon dioxide is introduced in place of oxygen, *i.e.* $Y_{CO_2}(r) = Y_{O_2}(r_{ogrid}) - Y_{O_2}(r)$. The initial composition on the Cartesian grid is the same as the composition at the inlet. Such initial conditions do not reflect the experimental set-up and were selected purely to improve stability of simulations during the initial stage.

For most cases, a grid resolution of 720 \times 896 ($x \times y$ directions) grid points on the Cartesian grid and 208 \times 432 ($r \times \theta$ directions) on the ogrid was sufficient to accurately resolve all flow features. It should be noted that the ogrid is stretched in a non-linear manner in the radial direction. For the resolution given above this resulted in $\Delta r_{min} = 8.3 \cdot 10^{-4}$ cm at the particle surface and $\Delta r_{max} = 6.8 \cdot 10^{-3}$ cm at the outer edge of the cylindrical grid. A schematic representation of the numerical grid together with initial condition is presented in figure 5. If the particle temperature is relatively low

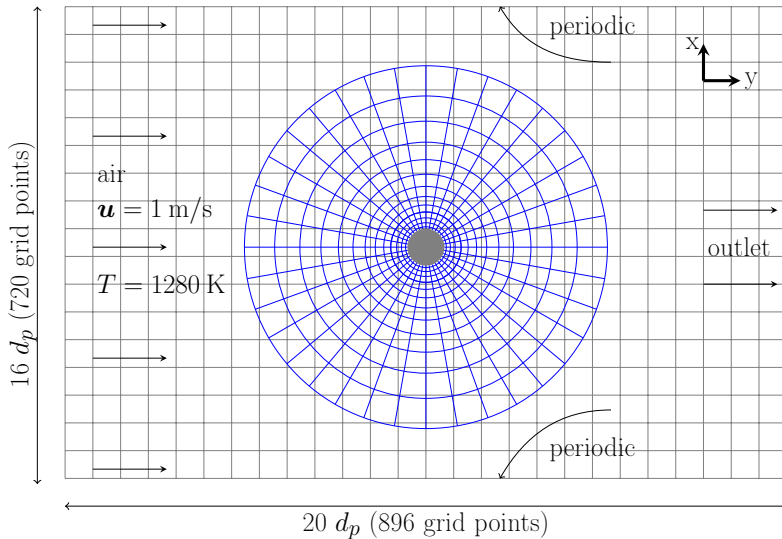


Figure 5: Schematic representation of the analyzed case (not drawn to scale)

($T_p \lesssim 1800$ K) the maximum time-step is limited to $\sim 10^{-7}$ s by convection, while for higher particle temperatures the time-step needs to be reduced to $\sim 10^{-8}$ s due to the shorter chemical timescales.

3. Results and discussion

3.1. Implementation of chemistry module - validation

Various aspects of the Pencil Code have been validated and tested a number of times and the results have been published in a large number of papers available in the open literature. See [27] for an overview of some relevant papers. In this work, we have, however, implemented several new methods and approximations to speed up the calculations, such as: simplified calculation of transport data, simplified global reaction mechanisms, heterogeneous reactions at the particle surface with the overset grid method, and variable speed of sound. In order to validate the current numerical model beyond the more specific validations presented in the previous section, the experimental set-up of Makino et al. [39] is reproduced numerically. In the experiment of Makino et al., combustion of a graphite rod was studied at different surface

temperatures, for different air velocities and temperatures. An important feature of the experiment is that the heat loss from the graphite surface due to radiation is balanced by electrical heating, such that a constant particle surface temperature is maintained at all times. As a result, a quasi-steady state is achieved for a relatively large fraction of the particle conversion time. In the current work, the case characterized by an air temperature of 1280 K and a velocity of 102.5 cm/s is analyzed for a range of particle surface temperatures. This particular selection of experimental conditions was motivated by the fact that the same case was studied numerically by Luo et al. [6], who demonstrated that a good agreement with the experimental results can be obtained using the chemical mechanism given by reactions (R1)-(R3). Despite the fact that Luo et al. also used the Pencil Code, there are two main differences between their approach and the approach used in the current work: 1) Luo et al. used kinetic theory to compute transport coefficients, and 2) their particle was resolved on a Cartesian grid using immersed boundary conditions for the particle surface.

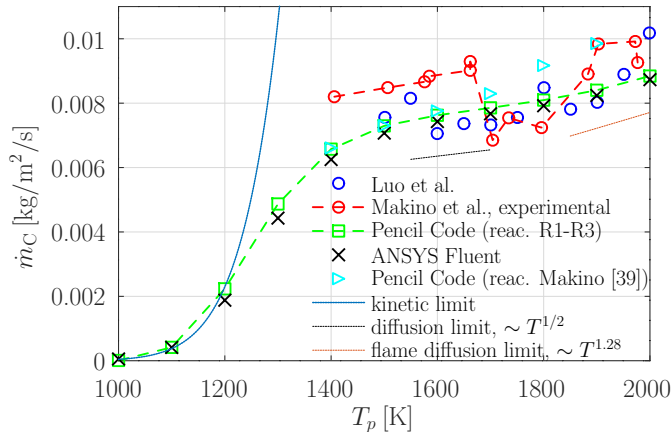


Figure 6: Comparison of carbon conversion rates as a function of particle surface temperature. The results for Luo et al. [6] are reproduced from their Fig. 8.

Fig. 6 presents the carbon conversion rate obtained with the current numerical approach (green squares) in addition to what was found experimentally by Makino et al. [39] (red circles) and numerically by Luo et al. [6]

(blue circles). In fact, what is shown is the conversion rate in the forward stagnation point. Additionally, kinetic (solid blue line) and diffusion (dotted black line) limits for oxidation are also included in figure 6. The first limit corresponds to the case of infinitely fast diffusion ($Y_{O_2, surface} = Y_{O_2, \infty}$), while the latter to the reaction rate being controlled by diffusion ($\sim T^{1/2}$). It can be seen that up to $T_p = 1200$ K, the carbon conversion rate is governed by kinetics, while around $T_p = 1600$ K the slope corresponding to the diffusion limit is achieved. There is one more limiting slope included in Fig. 6, which is called 'flame diffusion' limit. This limit arises due to the fact that at around $T_p = 1700$ K the flame begins to detach from the particle surface. The reason for this detachment is the large CO production at the surface and its subsequent transport by means of the Stefan flow and diffusion. The result is that most of the O_2 is consumed in the gas phase at the position of the flame that is formed away from the surface. As a consequence, mostly CO_2 can diffuse to the surface and the carbon conversion is due to the Boudouard reaction (R2). From the perspective of the oxidation reaction, the oxygen diffuses now towards the flame surface, not the particle surface. This effective surface grows proportionally to T^g , where the exponent g can be found by a fitting procedure. This was done in Fig. 7, from which it can be seen that the 'effective radius' scales as $T^{0.78}$. Here, the effective radius was computed as the average radial distance from the particle center to the flame, where it was assumed that the flame location corresponds to the grid point in which the gas phase reaction rate is the highest. The carbon conversion rate in the diffusion limit is proportional to the product of the mass transfer coefficient (k_i) and the effective surface:

$$\dot{m}_c \sim d_{p,eff}^2 k_i, \quad (26)$$

where $d_{p,eff}$ is the effective diameter of the flame surface. Since the mass transfer coefficient scales as $k_i \sim D_i/d_{p,eff}$ and $D_i \sim T^{1/2}$ (see Eqs. (16) and (17)), the conversion rate dependence on temperature becomes:

$$\dot{m}_c \sim d_{p,eff}^2 k_i \sim d_{p,eff} D_i \sim T^{1/2} T^{0.78} = T^{1.28}. \quad (27)$$

This is the flame diffusion limit seen in Fig. 6, which is reached for the highest of the studied particle surface temperatures.

Compared to the experimental results, slightly too low conversion is obtained for most temperatures. On the other hand, very similar magnitudes of conversion rates were obtained by Luo et al. [6], which indicates that the

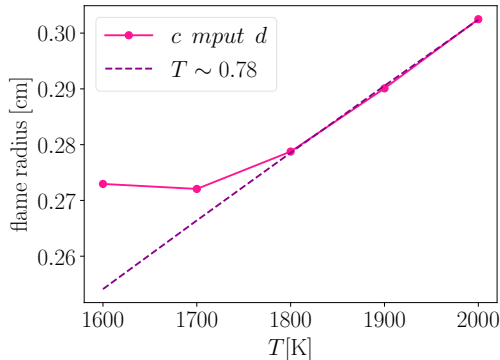


Figure 7: Effective flame radius in a function of temperature

difference is most probably caused by the reaction kinetics. It is in fact common that there is no agreement on the reaction kinetics and quite often a number of mechanisms are suggested, resulting in different reaction rates. The influence of heterogeneous kinetics has already been investigated by Nikrityuk et al. [42], who revealed that a factor of 2-3 difference in the carbon consumption rate can be expected between different sets of kinetic parameters that are found in the literature. A set of kinetic parameters for surface reactions was also proposed by Makino et al. [39] based on their experimental results and the conversion rates resulting from these parameters are presented in Fig. 6 (cyan triangles). It can be seen that this yielded a significantly higher carbon conversion rate at high surface temperatures, but did not lead to noticeable difference for $T_p \leq 1600$ K. This could be expected as the gasification reaction is much faster in Makino’s mechanism, while there is only a tiny difference in the oxidation rates when compared with the mechanism given in Table 1.

Another experimental feature that is not captured properly with the current approach is a sudden decrease of the conversion rate for surface temperatures around 1700–1800 K. This decrease is also present in the results shown in Fig. 6 in Luo et al. [6] (although the results in their Fig. 6 and Fig. 8 seem to be inconsistent regarding this feature). The main difference between their and the present numerical approach is how the transport coefficients are computed. In that respect, our approach is much simpler and, potentially, less accurate. Therefore, a further validation is essential. Such

a validation was performed using the ANSYS Fluent software, in which the same cases were reproduced and the resulting carbon conversion rates are shown as black x-signs in Fig. 6. The Fluent simulations were performed with the diffusion coefficients calculated from kinetic theory, as was also done by Luo et al. [6]. In addition, incompressible and steady state flow was assumed. Both assumptions are valid since the Mach number is low and the change in particle radius is very slow. As can be seen in Fig. 6, almost the same conversion rates were obtained using the complex formulation for the transport coefficients in ANSYS Fluent as for the simplified formulation used in the Pencil Code. In particular, the conversion rates in both cases are monotonically increasing functions, i.e. no reduction of the conversion rate was observed around $T_p = 1700\text{--}1800$ K. This verifies that the simplified approach for the transport is not responsible for this qualitative discrepancy between the experimental results and our numerical results, and allows us to gain confidence in the predictions of our approach.

It still remains to be understood why conversion rate obtained with the Pencil Code (and ANSYS Fluent) does not follow the experimental trend when it comes to the dip in carbon conversion rate around $T_p = 1700$ K. There exist several physical explanations of this trend in the literature, e.g.: it is attributed to the change of the effective reaction zone thickness [43], it is linked with the change of molecular structure of graphite [44, 45], it is caused by thermal rearrangement of surface-covering sites, from highly reactive at low temperatures to less reactive at higher temperatures [46, 47]. Makino et al. [39] argue that the presence of the dip stems from the fact that the dominant surface reaction shifts from oxidation to gasification around $T_p = 1700$ K. The reason for this shift is that at low temperatures the oxygen is used to oxidize the carbon directly at the surface, while at high temperatures the oxygen is used to oxidize CO in a CO-flame surrounding the particle, while the carbon conversion proceeds through gasification of CO₂ that diffuse to the surface from the CO flame. This change in the dominant mechanism for CO production at the surface is correctly predicted by the Pencil Code, as can be seen in Fig. 8. However, the shift is gradual and does not result in the non-monotonicity of $\dot{m}_C(T_p)$ as suggested by Makino et al. [39]. Another plausible explanation for the dip in \dot{m}_c is that since the shape of the conversion function depends on the gas phase kinetics, as shown in [48], the kinetic parameters we use might not yield the right behavior. While all the above explanations are probable, it is also possible that the results are affected by the measurement method. In the experiment, the surface temperature of the rod

was measured using two-color pyrometer [49]. These measurements are used to control the internal heating that is required to maintain a constant temperature of the graphite rod. This method is indirect, it might therefore be difficult to precisely measure the surface temperature without the results being affected by the surrounding flame. At relatively low surface temperatures, the flame remains attached to the surface, so the difference between the flame and the surface temperature is small. However, at temperatures at which the drop in the conversion rate is observed, the flame starts detaching from the rod surface. As such, the flame temperature might be significantly higher, giving a false impression of higher surface temperature. Since the experiment attempts to maintain a constant surface temperature, it is likely that the rod was cooled to lower temperature than intended, which resulted in a sudden decrease of the conversion rate. These are, however, only conjectures, and the reason for the qualitative inconsistency between the experiment and our results might be a combination of several of the above-mentioned factors.

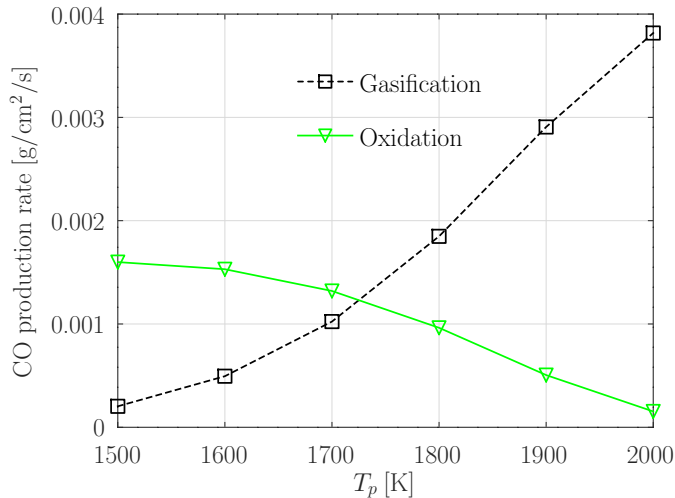


Figure 8: Contributions to CO production from gasification and oxidation

3.2. Sensitivity analysis

In order to better understand which parameters that control the carbon conversion rate, we have done a series of parameter studies. The first study

investigates the effect of species diffusivity. In this respect we varied the diffusivities of O_2 , CO_2 and CO from half of their original value up to twice the original value, and investigated how this influenced the solid (carbon) conversion rate. For this investigation, we concentrate on the situation where the particle temperature is 1700 K.

From the upper panel of figure 9 we see that the solid conversion rate has a strong dependence on diffusivity of O_2 . This is expected since higher diffusivity of O_2 will yield a higher transport rate of O_2 to the solid, which will then be able to convert (oxidize) more solid. From the lower panel of figure 9 we see that increasing the oxygen diffusivity results in an increase of both the oxidation and gasification rates of the solid. At first glance, it may look surprising that even the gasification rate increases with increased O_2 diffusivity, but the reason is simply that at the surface temperature of 1700 K that we focus on here, we experience a higher surface-fraction of CO_2 , resulting from oxidation of CO very close to the surface.

Let us now move on to the effect of CO diffusivity. We see from the upper panel of figure 9 that the solid conversion rate is weakly increasing with increasing diffusivity of CO . This effect is, however, more complicated than that of O_2 diffusivity, as can be seen from the lower panel of figure 9, which shows that solid conversion due to oxidation increases with CO diffusivity, while the opposite is true for gasification. To elucidate this behaviour in figure 10, we show CO_2 and O_2 concentrations along the y-axis in front of the solid. The dashed vertical line in the figure corresponds to the solid surface. From the left panel we see that lower CO diffusivity yields higher concentration of CO_2 at the surface, which explains why the gasification rate decreases with increasing CO diffusivity. The reason for the increased CO_2 concentration at the surface is that a lower CO diffusivity moves the flame closer to the surface. Since the CO_2 concentration is highest close to where it is produced, which is in the CO flame, this means that the concentration of CO_2 at the surface is also higher. Studying the gradients of O_2 very close to the surface (right panel) we see that the case with higher CO diffusivity has a steeper gradient of O_2 very close to the surface. For a given O_2 diffusivity, a steeper O_2 gradient results in more transport of O_2 to the surface, and, hence, more solid oxidation.

Finally, when increasing the diffusivity of CO_2 , we see from figure 9 that the solid conversion rate is actually reduced. This is despite the fact that the solid oxidation rate is independent of the diffusivity of CO_2 (see the lower panel of figure 9). The question is therefore why the solid gasification rate is

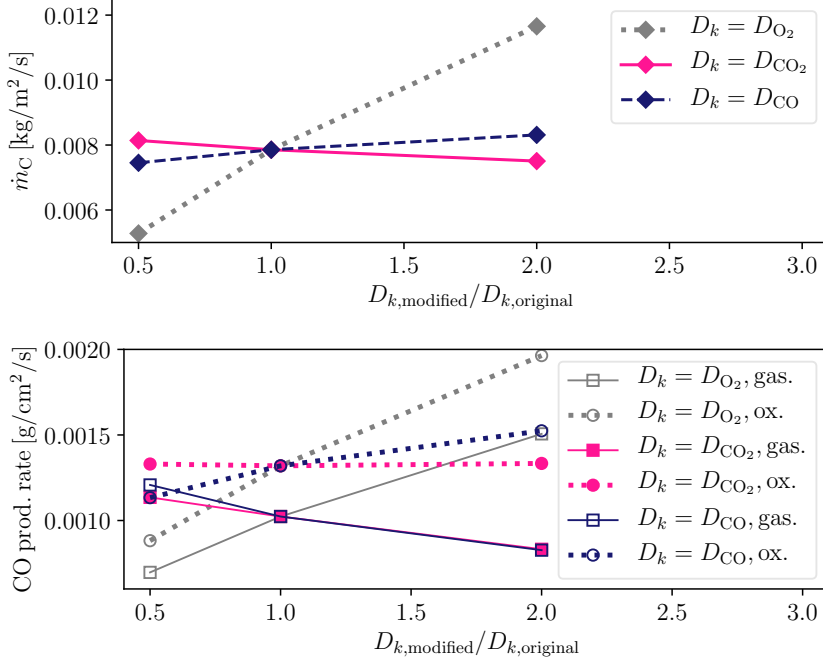


Figure 9: Upper: conversion rates for different diffusion coefficients, lower: contributions from gasification/oxidation to the CO production rate, $T_p = 1700$ K

reduced when the CO_2 diffusivity is increased. The answer to that question is that for the current case, which has a solid temperature of 1700 K, the CO_2 is always produced close to the solid surface due to the CO flame not being significantly lifted. Consequently, an increased CO_2 diffusivity will tend to transport CO_2 away from the surface, lowering the surface concentration, and, by that, reducing the gasification rate.

Another parameter that can influence the carbon conversion rate is chemical kinetics, both of surface and gas phase reactions. In the following we will proceed by studying the sensitivity of the carbon conversion rate to the chemical reactivity. The reactivity is varied by changing the pre-exponential factor. First, the surface reaction rate is varied. This is done separately for the oxidation (denoted by $R1$) and gasification (denoted by $R2$) reactions.

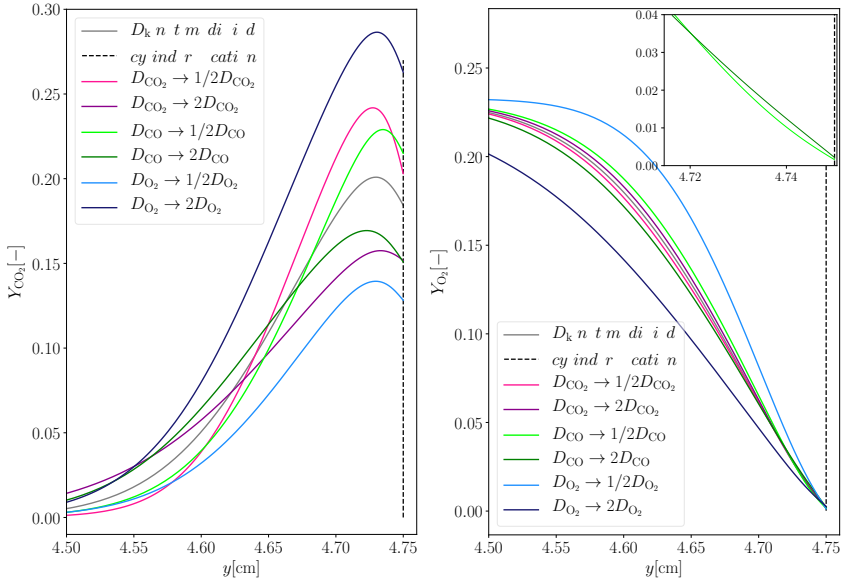


Figure 10: Oxygen and carbon dioxide mass fractions and temperature profiles in the particle stagnation region as obtained for different diffusion coefficients

The effect of this variation on the conversion rate can be seen in figure 11 for two different surface temperatures: 1200 and 1800 K.

For the higher temperature, the conversion rate is almost uninfluenced by changes in the oxidation rate, which is due to the fact that at such high temperatures the reaction is controlled almost purely by diffusion. This is confirmed in the lower panel of figure 11, which shows that the oxidation rate (R1) variations have no effect neither on the contribution from oxidation, nor on the contribution from gasification. At the same surface temperature, variations in the gasification rate (R2) have only a weak effect on the solid conversion rate. However, the reason for this is quite different, as in this case both contributions from gasification and oxidation are significantly affected, as can be observed in the lower panel of figure 11. These two contributions are affected in such a way that the increase in the carbon conversion rate due to the higher gasification rate is almost exactly balanced by the decrease in the solid conversion rate due to the faster oxidation.

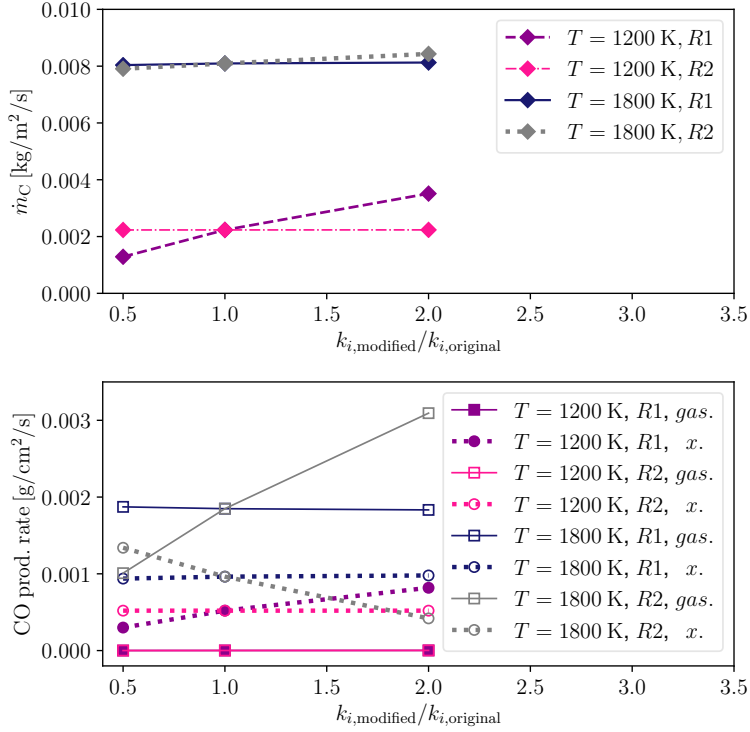


Figure 11: upper: conversion rates as obtained for modified surface reaction rates, lower: contributions from gasification/oxidation to the CO production rate. *R1* and *R2* denote oxidation and gasification, respectively, and indicate which reaction has been modified, while *ox.* and *gas.* denote contribution from oxidation and gasification to the CO production rate.

For $T_p = 1200 \text{ K}$, the carbon conversion rate is directly proportional to the change of the oxidation rate (*R1*), but does not depend on the gasification rate (*R2*). This is expected since at this temperature the surface reaction rates are controlled by kinetics, but the contribution to the solid conversion rate from gasification is around two orders of magnitude smaller than the contribution from oxidation.

The effect of the gas phase kinetics is shown in figure 12, from which

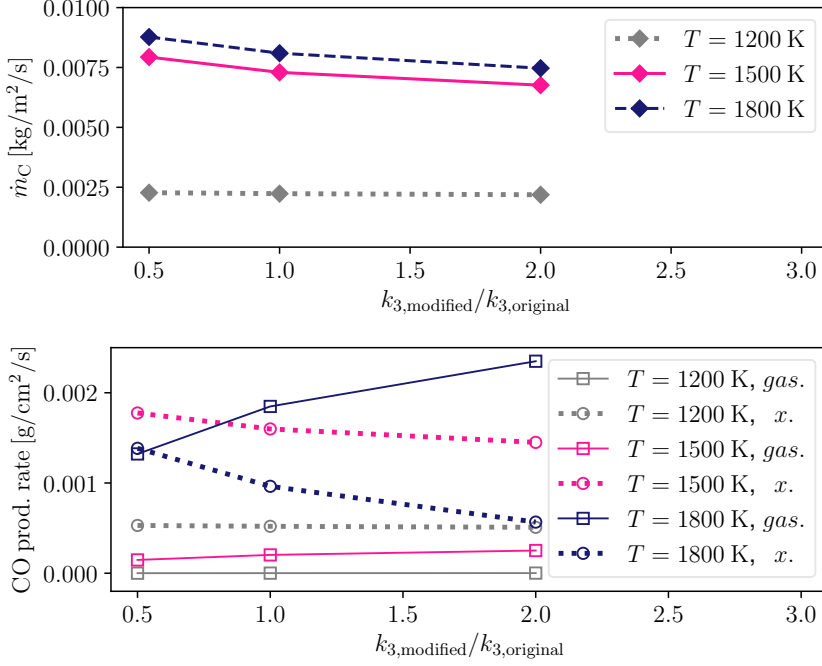


Figure 12: upper: conversion rates as obtained for modified homogeneous reaction rate, lower: contributions from gasification/oxidation to the CO production rate

it is clear that the solid conversion rate is not sensitive to the gas phase reaction rate variations, as long as the surface reactions are controlled by kinetics, i.e. for $T_p = 1200\text{ K}$. At higher particle surface temperatures, the solid conversion becomes faster upon decreasing the gas phase reaction rate. This is consistent with theoretical predictions of Libby and Blake [50] and Makino [51] who showed that the solid conversion rate is highest in the limit of the gas phase reaction rate approaching zero (so called 'frozen mode'), and lowest in the limit of very fast homogeneous reaction rate. This tendency can be linked to the fact that the higher the gas phase reaction rate, the more oxygen is consumed inside the CO-flame before reaching the particle surface, thus, the contribution to the combustion rate from oxidation decreases (see the lower panel of figure 12). Furthermore, the flame characteristics are also

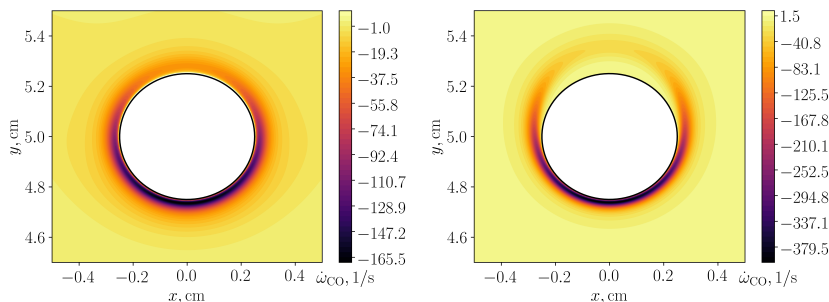


Figure 13: CO flame contours, $T_p = 1800$ K, left: $k_{3,f} \rightarrow 0.5k_{3,f}$, right: $k_{3,f} \rightarrow 2k_{3,f}$

directly linked to the gas phase reaction rate. In particular, when the rate is increased, the flame becomes thinner and can detach from the particle surface or shift further from the surface if it was already detached. This situation can be observed in figure 13, which presents contours of the CO flame for the cases in which the pre-exponential factor of the homogeneous reaction rate was halved and doubled relative to what it was originally. A consequence of the flame moving away from the solid surface is that the gradient of oxygen between the flame and the surface becomes less steep, leading to a slower diffusion of O_2 towards the particle. This can be observed for $T_p = 1800$ K in figure 14, which shows oxygen profiles along the centerline behind the particle. For $T_p = 1500$ K, the flame is much closer to the solid surface, thus the oxygen profiles further away are almost parallel to each other, and the contribution to the combustion rate from oxidation is affected to a smaller extent, as seen in the lower panel of figure 12. The situation is opposite for carbon dioxide, as higher rate of homogeneous reaction means more CO_2 that is produced inside the flame and faster diffusion of this species to the surface. It is also interesting to notice in the right panel of figure 14 that for $T_p = 1500$ K the concentration of CO_2 at the solid surface is almost the same as the concentration inside the flame, which indicates that the gasification rate is still controlled by kinetics. Therefore, the increase of the contribution from gasification is simply caused by the higher mass fraction of CO_2 at the surface, not by the diffusion rate as was the case for $T_p = 1800$ K.

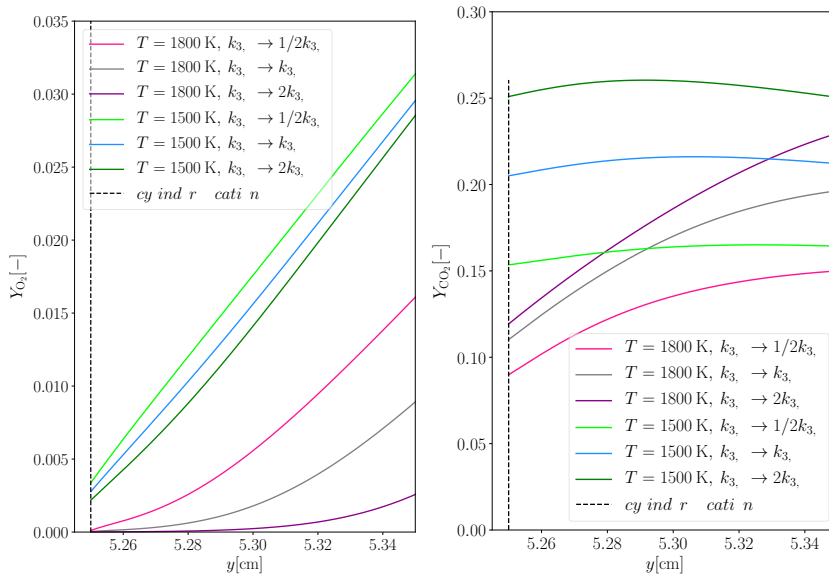


Figure 14: Oxygen and carbon dioxide mass fraction profiles along the centerline behind the particle as obtained for different gas phase reaction rates

4. Conclusions

The goal of this work was twofold, first to formulate an efficient approach to model resolved solid particle combustion, then to understand the relevant physics and sensitivity. For this purpose, a model within the framework of the Pencil Code was developed and validated against experimental and numerical data. Our model is not as advanced as some approaches proposed in the literature, but it has a great potential to capture the transient nature of char conversion upon further development. Although within this study the laminar flow over a single particle was analyzed, the model can also be employed in turbulent flow situations. In order to achieve high efficiency, an overset grid was used, which allowed us to reduce the computational expense without compromising the accuracy. Other features of the numerical approach that have been proposed for the sake of efficiency are the speed of sound reduction and fitting of the transport coefficients (kinetic viscosity, thermal conductivity and species diffusion coefficients). It was demonstrated

that the above mentioned actions did not lead to relevant changes in the results for the range of considered conditions. On the other hand, the results are in general dependent on the chemical mechanism and care must be taken to use a mechanism that represents well the examined situation.

A sensitivity analysis was performed that showed that the solid conversion rate can be affected by different parameters (diffusion coefficients, surface kinetics and gas phase kinetics). Which of these parameters is the most important, depends on whether the conversion is controlled by the reaction kinetics or the reactant diffusion. For most of the studied particle surface temperatures, the conversion was found to be controlled by the oxygen diffusion to the particle (around $1400 < T_p < 1800$ K) and to the effective flame ($T_p > 1800$ K) surfaces. Even though in diffusion-controlled conditions the overall solid conversion rate is only weakly dependent on kinetics, the contributions from gasification and oxidation reactions, as well as the flame structure, might be substantially affected.

It is remarkable that the combustion behavior of the solid particle can be explored in such a detailed manner by employing a very simple chemical mechanism. However, a complex mechanism is needed for a more thorough analysis. At the current stage of development, the model presented in this study was validated against quasi-steady experimental results. In order to explore transient phenomena in further studies, it would be necessary to account for the heat transfer at the particle surface, in particular radiation between the particle and the surrounding gas, and for temperature gradients inside the particle. Finally, the reason for the conversion rate to drop around $T_p = 1700$ K could be explored by including models that account for changes in the molecular structure of the solid.

Appendix A. Derivation of boundary conditions for species

Species transport equation,

$$\frac{\partial(\rho Y_k)}{\partial t} + \nabla \cdot (\rho \mathbf{u} Y_k + \mathbf{J}_k) = \dot{\omega}_k, \quad (\text{A.1})$$

can be expressed in integral form as

$$\int_V \frac{\partial(\rho Y_k)}{\partial t} dV + \int_V \nabla \cdot (\rho \mathbf{u} Y_k + \mathbf{J}_k) dV = \int_V \dot{\omega}_k dV. \quad (\text{A.2})$$

Using the divergence theorem, Eq. (A.2) becomes

$$\int_V \frac{\partial(\rho Y_k)}{\partial t} dV + \int_S (\rho \mathbf{u} Y_k + \mathbf{J}_k) \cdot \hat{\mathbf{n}} dA = \int_V \dot{\omega}_k dV, \quad (\text{A.3})$$

where $\hat{\mathbf{n}}$ is a unit vector normal to the surface. At the particle surface all volumetric integrals tend to 0 and a source term due to the surface reactions (\dot{m}_k) appears in the place of the volumetric reaction term ($\dot{\omega}_k$). Also, since the particle is assumed to be perfectly cylindrical $\hat{\mathbf{n}} = \hat{\mathbf{r}}$, where $\hat{\mathbf{r}}$ is a unit normal vector in the radial direction. After taking all of the above into account, Eq. (A.3) becomes

$$\int_S (\rho \mathbf{u} Y_k + \mathbf{J}_k) \cdot \hat{\mathbf{r}} dA = \int_S \dot{m}_k dA. \quad (\text{A.4})$$

Using the fact that for an arbitrary surface

$$\int_S b dA = \int_S c dA \Leftrightarrow b = c, \quad (\text{A.5})$$

Eq. (A.4) can be written in a differential form

$$(\rho \mathbf{u} Y_k + \mathbf{J}_k) \cdot \hat{\mathbf{r}} = \dot{m}_k. \quad (\text{A.6})$$

Summing over all gas phase species one obtains

$$\sum_k (\rho \mathbf{u} Y_k + \mathbf{J}_k) \cdot \hat{\mathbf{r}} = \rho u_r = \sum_k \dot{m}_k = -\dot{m}_C \quad (\text{A.7})$$

where it has been used that $\sum_k \mathbf{J}_k \cdot \hat{\mathbf{r}} = 0$. Here, \dot{m}_C is a carbon consumption rate and u_r is the outward velocity of the species mixture in the radial direction. One can now substitute

$$\mathbf{J}_k = -\rho D_k \nabla Y_k, \quad (\text{A.8})$$

$$\mathbf{u} \cdot \hat{\mathbf{r}} = u_r = -\dot{m}_C / \rho \quad (\text{A.9})$$

and

$$\nabla Y_k \cdot \hat{\mathbf{r}} = \frac{\partial Y_k}{\partial r} \quad (\text{A.10})$$

into Eq. (A.6) to arrive at the final form of boundary conditions for species mass fractions at the particle surface,

$$\dot{m}_k + \dot{m}_C Y_k + \rho D_k \frac{\partial Y_k}{\partial r} = 0. \quad (\text{A.11})$$

Acknowledgments

This study has been supported by the statutory research fund of the Silesian University of Technology, Faculty of Energy and Environmental Engineering, Department of Thermal Engineering, Gliwice, Poland. The research leading to these results has also received funding from the research projects: 'CHEERS', financed by the European Union's Horizon 2020 research and innovation program (grant agreement No. 764697).

References

- [1] [Coal 2018](#), Tech. rep., International Energy Agency, Paris (2020).
URL www.iea.org/reports/coal-2020
- [2] [Renewables 2020](#), Tech. rep., International Energy Agency, Paris (2020).
URL <https://www.iea.org/reports/renewables-2020>
- [3] [World energy outlook 2020](#), Tech. rep., International Energy Agency, Paris (2020).
URL <https://www.iea.org/reports/world-energy-outlook-2020>
- [4] T. Hara, M. Muto, T. Kitano, R. Kurose, S. Komori, Direct numerical simulation of a pulverized coal jet flame employing a global volatile matter reaction scheme based on detailed reaction mechanism, *Combustion and Flame* 162 (12) (2015) 4391–4407. doi:10.1016/J.COMBUSTFLAME.2015.07.027.
- [5] K. Luo, Y. Bai, T. Jin, K. Qiu, J. Fan, Direct Numerical Simulation Study on the Stabilization Mechanism of a Turbulent Lifted Pulverized Coal Jet Flame in a Heated Coflow, *Energy Fuels* 31 (8) (2017) 8742–8757. doi:10.1021/acs.energyfuels.7b01342.
- [6] K. Luo, C. Mao, J. Fan, Z. Zhuang, N. Haugen, Fully resolved simulations of single char particle combustion using a ghost-cell immersed boundary method, *AIChE Journal* 64 (7) (2018) 2851–2863. doi:10.1002/aic.16136.
- [7] M. Muto, K. Yuasa, R. Kurose, Numerical simulation of ignition in pulverized coal combustion with detailed chemical reaction mechanism, *Fuel* 190 (2017) 136–144. doi:10.1016/j.fuel.2016.11.029.

- [8] M. Rieth, A. Kempf, A. Kronenburg, O. Stein, Carrier-phase DNS of pulverized coal particle ignition and volatile burning in a turbulent mixing layer, *Fuel* 212 (2018) 364–374. doi:10.1016/J.FUEL.2017.09.096.
- [9] X. Wen, A. Shamooni, O. T. Stein, L. Cai, A. Kronenburg, H. Pitsch, A. M. Kempf, C. Hasse, Detailed analysis of early-stage NO_x formation in turbulent pulverized coal combustion with fuel-bound nitrogen, in: *Proceedings of the Combustion Institute*, Vol. 38, Elsevier, 2021, pp. 4111–4119. doi:10.1016/j.proci.2020.06.317.
- [10] J. G. M. Kuerten, Point-Particle DNS and LES of Particle-Laden Turbulent flow - a state-of-the-art review, *Flow, Turbulence and Combustion* 97 (3) (2016) 689–713. doi:10.1007/s10494-016-9765-y.
- [11] M. Vascellari, H. Xu, C. Hasse, Flamelet modeling of coal particle ignition, *Proceedings of the Combustion Institute* 34 (2) (2013) 2445–2452. doi:10.1016/j.proci.2012.06.152.
- [12] G. L. Tufano, O. T. Stein, A. Kronenburg, A. Frassoldati, T. Faravelli, L. Deng, A. M. Kempf, M. Vascellari, C. Hasse, Resolved flow simulation of pulverized coal particle devolatilization and ignition in air- and O₂/CO₂-atmospheres, *Fuel* 186 (2016) 285–292. doi:10.1016/j.fuel.2016.08.073.
- [13] G. L. Tufano, O. T. Stein, B. Wang, A. Kronenburg, M. Rieth, A. M. Kempf, Coal particle volatile combustion and flame interaction. Part I: Characterization of transient and group effects, *Fuel* 229 (2018) 262–269. doi:10.1016/j.fuel.2018.02.105.
- [14] G. L. Tufano, O. T. Stein, B. Wang, A. Kronenburg, M. Rieth, A. M. Kempf, Coal particle volatile combustion and flame interaction. Part II: Effects of particle Reynolds number and turbulence, *Fuel* 234 (2018) 723–731. doi:10.1016/j.fuel.2018.07.054.
- [15] M. Kestel, P. Nikrityuk, O. Hennig, C. Hasse, Numerical study of the partial oxidation of a coal particle in steam and dry air atmospheres, in: *IMA Journal of Applied Mathematics (Institute of Mathematics and Its Applications)*, Vol. 77, Oxford University Press, 2012, pp. 32–46. doi:10.1093/imamat/hxr071.

- [16] A. Richter, P. A. Nikrityuk, M. Kestel, Numerical Investigation of a Chemically Reacting Carbon Particle Moving in a Hot O₂/CO₂ Atmosphere, *Industrial Engineering Chemistry Research* 52 (16) (2013) 5815–5824. doi:10.1021/ie302770j.
- [17] D. Safronov, M. Kestel, P. Nikrityuk, B. Meyer, Particle resolved simulations of carbon oxidation in a laminar flow, *Canadian Journal of Chemical Engineering* 92 (10) (2014) 1669–1686. doi:10.1002/cjce.22017.
- [18] S. Schulze, P. Nikrityuk, F. Compant, A. Richter, B. Meyer, Particle-resolved numerical study of char conversion processes in packed beds, *Fuel* 207 (2017) 655–662. doi:10.1016/j.fuel.2017.05.071.
- [19] Z. Xue, Q. Guo, Y. Gong, J. Xu, G. Yu, Numerical study of a reacting single coal char particle with different pore structures moving in a hot O₂/CO₂ atmosphere, *Fuel* 206 (2017) 381–389. doi:10.1016/j.fuel.2017.06.035.
- [20] Z. Xue, Y. Gong, Q. Guo, Y. Wang, G. Yu, Conversion characteristics of a single coal char particle with high porosity moving in a hot O₂/CO₂ atmosphere, *Fuel* 256 (2019) 115967. doi:10.1016/j.fuel.2019.115967.
- [21] A. Richter, M. Kestel, P. A. Nikrityuk, Pore-Resolved Simulation of Char Particle Combustion/Gasification, *Gasification Processes: Modeling and Simulation* 9783527335503 (2014) 243–270. doi:10.1002/9783527673186.CH9.
- [22] J. Lee, A. Tomboulides, S. Orszag, R. Yetter, F. Dryer, A transient two-dimensional chemically reactive flow model: Fuel particle combustion in a nonquiescent environment, *Symposium (International) on Combustion* 26 (2) (1996) 3059–3065. doi:10.1016/S0082-0784(96)80149-4.
- [23] S. Farazi, M. Sadr, S. Kang, M. Schiemann, N. Vorobiev, V. Scherer, H. Pitsch, Resolved simulations of single char particle combustion in a laminar flow field, *Fuel* 201 (2017) 15–28. doi:10.1016/j.fuel.2016.11.011.
- [24] T. Sayadi, S. Farazi, S. Kang, H. Pitsch, Transient multiple particle simulations of char particle combustion, *Fuel* 199 (2017) 289–298. doi:10.1016/j.fuel.2017.02.096.

- [25] G. L. Tufano, O. T. Stein, A. Kronenburg, G. Gentile, A. Stagni, A. Frassoldati, T. Faravelli, A. M. Kempf, M. Vascellari, C. Hasse, Fully-resolved simulations of coal particle combustion using a detailed multi-step approach for heterogeneous kinetics, *Fuel* 240 (2019) 75–83. doi:10.1016/j.fuel.2018.11.139.
- [26] C. B. Nguyen, J. Scherer, M. Hartwich, A. Richter, The morphology evolution of char particles during conversion processes, *Combustion and Flame* 226 (2021) 117–128. doi:10.1016/j.combustflame.2020.11.038.
- [27] A. Brandenburg, A. Johansen, P. A. Bourdin, W. Dobler, W. Lyra, M. Rheinhardt, S. Bingert, N. E. L. Haugen, A. Mee, F. Gent, N. Babkovskaia, C.-C. Yang, T. Heinemann, B. Dintrans, D. Mitra, S. Candelaresi, J. rn Warnecke, P. J. Käpylä, A. Schreiber, P. Chatterjee, M. J. Käpylä, X.-Y. Li, J. K. ger, J. rgen R. Aarnes, G. R. Sarson, J. S. Oishi, J. Schober, R. Plasson, C. Sandin, E. Karchniwy, L. F. S. Rodrigues, A. Hubbard, G. Guerrero, A. Snodin, I. R. Losada, J. Pekkilä, C. Qian, The pencil code, a modular mpi code for partial differential equations and particles: multipurpose and multiuser-maintained, *Journal of Open Source Software* 6 (58) (2021) 2807. doi:10.21105/joss.02807.
- [28] S. E. Sherer, J. N. Scott, High-order compact finite-difference methods on general overset grids, *Journal of Computational Physics* 210 (2) (2005) 459–496. doi:10.1016/j.jcp.2005.04.017.
- [29] J. Chicheportiche, X. Gloerfelt, Study of interpolation methods for high-accuracy computations on overlapping grids, *Computers and Fluids* 68 (2012) 112–133. doi:10.1016/j.compfluid.2012.07.019.
- [30] M. R. Visbal, D. V. Gaitonde, High-order-accurate methods for complex unsteady subsonic flows, *AIAA journal* 37 (10) (1999) 1231–1239. doi:10.2514/2.591.
- [31] M. R. Visbal, D. V. Gaitonde, On the use of higher-order finite-difference schemes on curvilinear and deforming meshes, *Journal of Computational Physics* 181 (1) (2002) 155–185. doi:10.1006/jcph.2002.7117.

- [32] J. R. Aarnes, N. E. L. Haugen, H. I. Andersson, High-order overset grid method for detecting particle impaction on a cylinder in a cross flow, *International Journal of Computational Fluid Dynamics* 33 (1-2) (2019) 43–58. doi:[10.1080/10618562.2019.1593385](https://doi.org/10.1080/10618562.2019.1593385).
- [33] J. R. Aarnes, T. Jin, C. Mao, N. E. L. Haugen, K. Luo, H. I. Andersson, Treatment of solid objects in the Pencil Code using an immersed boundary method and overset grids, *Geophysical & Astrophysical Fluid Dynamics* 114 (1-2) (2020) 35–57. doi:[10.1080/03091929.2018.1492720](https://doi.org/10.1080/03091929.2018.1492720).
- [34] N. Babkovskaia, N. E. Haugen, A. Brandenburg, A high-order public domain code for direct numerical simulations of turbulent combustion, *Journal of Computational Physics* 230 (1) (2011) 1–12. arXiv:[1005.5301](https://arxiv.org/abs/1005.5301), doi:[10.1016/j.jcp.2010.08.028](https://doi.org/10.1016/j.jcp.2010.08.028).
- [35] S. R. Turns, *An introduction to combustion: Concepts and Applications*. Second edition., McGraw hills international editions, 2000.
- [36] L. Zhang, K. Liu, C. You, Fictitious domain method for fully resolved reacting gas-solid flow simulation, *Journal of Computational Physics* 299 (2015) 215–228. doi:<https://doi.org/10.1016/j.jcp.2015.07.010>.
- [37] F. L. Dryer, C. K. Westbrook, Simplified Reaction Mechanisms for the Oxidation of Hydrocarbon Fuels in Flames, *Combustion Science and Technology* 27 (1-2) (1981) 31–43. doi:[10.1080/00102208108946970](https://doi.org/10.1080/00102208108946970).
- [38] N. E. L. Haugen, R. E. Mitchell, M. B. Tilghman, A comprehensive model for char particle conversion in environments containing O₂ and CO₂, *Combustion & Flame* 162 (2015) 1455–1463. doi:[10.1016/j.combustflame.2014.11.015](https://doi.org/10.1016/j.combustflame.2014.11.015).
- [39] A. Makino, T. Namikiri, K. Kimura, Combustion rates of graphite rods in the forward stagnation field with high-temperature airflow, *Combustion and Flame* 132 (4) (2003) 743–753. doi:[10.1016/S0010-2180\(02\)00537-0](https://doi.org/10.1016/S0010-2180(02)00537-0).
- [40] S. Gordon, B. McBride, *Computer program for calculation of complex chemical equilibrium compositions*, no. 1311, NASA Reference Publication, 1971.

- [41] A. Brandenburg, Computational aspects of astrophysical MHD and turbulence, in: *Advances in Nonlinear Dynamos*, CRC Press, 2003, pp. 269–344. doi:[10.1201/9780203493137-9](https://doi.org/10.1201/9780203493137-9).
- [42] P. A. Nikrityuk, M. Gräbner, M. Kestel, B. Meyer, Numerical study of the influence of heterogeneous kinetics on the carbon consumption by oxidation of a single coal particle, *Fuel* 114 (2013) 88–98. doi:[10.1016/j.fuel.2012.10.037](https://doi.org/10.1016/j.fuel.2012.10.037).
- [43] R. T. Yang, M. Steinberg, A Diffusion Cell Method for Studying Heterogeneous Kinetics in the Chemical Reaction/Diffusion Controlled Region. Kinetics of $C + CO_2 \rightarrow 2CO$ at 1200-1600 °C, *Industrial and Engineering Chemistry Fundamentals* 16 (2) (1977) 235–242. doi:[10.1021/i160062a011](https://doi.org/10.1021/i160062a011).
- [44] D. E. Rosner, H. D. Allendor, Comparative studies of the attack of pyrolytic and isotropic graphite by atomic and molecular oxygen at high temperatures, *AIAA Journal* 6 (4) (1968) 650–654. doi:[10.2514/3.4558](https://doi.org/10.2514/3.4558).
- [45] D. E. Rosner, High-Temperature Gas-Solid Reactions, *Annual Review of Materials Science* 2 (1) (1972) 573–606. doi:[10.1146/annurev.ms.02.080172.003041](https://doi.org/10.1146/annurev.ms.02.080172.003041).
- [46] J. Nagle, R. F. Strickland-Constable, Oxidation of carbon between 1000-2000 °C, in: *Proceedings of the Fifth Conference on Carbon*, Pergamon, 1962, pp. 154–164. doi:<https://doi.org/10.1016/B978-0-08-009707-7.50026-1>.
- [47] J. R. Walls, R. F. Strickland-Constable, Oxidation of carbon between 1000-2400 °C, *Carbon* 1 (3) (1964) 333–338. doi:[10.1016/0008-6223\(64\)90288-x](https://doi.org/10.1016/0008-6223(64)90288-x).
- [48] A. Makino, N. Araki, Y. Mihara, Combustion of artificial graphite in stagnation flow: Estimation of global kinetic parameters from experimental results, *Combustion and Flame* 96 (3) (1994) 261–274. doi:[10.1016/0010-2180\(94\)90013-2](https://doi.org/10.1016/0010-2180(94)90013-2).
- [49] A. Makino, T. Namikiri, N. Araki, Combustion rate of graphite in a high stagnation flowfield and its expression as a function of the transfer num-

ber, in: Symposium (International) on Combustion, Vol. 27, Elsevier, 1998, pp. 2949–2956. [doi:10.1016/S0082-0784\(98\)80154-9](https://doi.org/10.1016/S0082-0784(98)80154-9).

- [50] P. A. Libby, T. R. Blake, Theoretical study of burning carbon particles, *Combustion and Flame* 36 (C) (1979) 139–169. [doi:10.1016/0010-2180\(79\)90056-7](https://doi.org/10.1016/0010-2180(79)90056-7).
- [51] A. Makino, An approximate explicit expression for the combustion rate of a small carbon particle, *Combustion and Flame* 90 (2) (1992) 143–154. [doi:10.1016/0010-2180\(92\)90116-7](https://doi.org/10.1016/0010-2180(92)90116-7).

